A Continuum Model for Slip-Twinning Interactions in Magnesium and Magnesium Alloys

Thesis by

Yingrui Chang

In Partial Fulfillment of the Requirements

for the Degree of

Doctor of Philosophy

California Institute of Technology

Pasadena, California

2016

(Defended January 15, 2016)

All models are wrong, but some are useful.

George E. P. Box

Acknowledgments

This research was sponsored by the Army Research Laboratory and was accomplished under Cooperative Agreement Number W911NF-12-2-0022. The views and conclusions contained in this document are those of the authors and should not be interpreted as representing the official policies, either expressed or implied, of the Army Research Laboratory or the U.S. Government. The U.S. Government is authorized to reproduce and distribute reprints for Government purposes notwithstanding any copyright notation herein.

Firstly, I want to express my sincere appreciation to the people who have been supporting me and collaborating with me to make this research work possible. Most importantly, I want to thank my Ph.D. advisor, Professor Dennis Kochmann, for his supervision and support over the last five years. Working with him has been a wonderful and rewarding experience. His creative ideas and coutinuous encouragement have always been a source of motivation for me to pursue the challenging problems and to do the best in my research. In addition, Professor Kochmann has been a wonderful teacher and mentor not only in class but in almost every aspect of life and will always be a model for me to learn from.

I would like to give my special thanks to Professor Kaushik Bhattacharya for his effort co-leading the MEDE metal research and all the encouragement and support he has given me. The Friday-MEDE meetings were always influential and I have learned a lot from my interaction with him.

I am very grateful to have Professor Michael Ortiz serve on my thesis committee and I appreciate all the valuable advice they gave for my research. In addition, Professor Ortiz is a great teacher for introducing all the advanced subjects in solid mechanics. Particularly, the subject of continuum mechanics and the associated computational techniques I learned from him are the basis for this research work and I also appreciate his generosity for sharing his computational framework "Eureka"

with me in my first few years of study. I want to thank our ARL collaborator Dr. Jeff Lloyd for flying to Caltech to serve as my committee member and for the data he provided for simulating the response of Mg polycrystals, which has been extremely helpful. I have always enjoyed the discussions with him on the modeling of Mg. I would like to thank Professor José Andrade for serving on my thesis committee and for the advice he gave during my defense to improve this work.

Besides my committee members, I want to express my deep gratitude to our Caltech/JHU/ARL collaborators in the MEDE project for their generosity in sharing their data and valuable research advice. In particular, I appreciate the data from Kolsky bar experiments provided by Professor K.T. Ramesh of JHU and his students, Neha Dixit and Kavan Hazeli, which helped to validate our simulations. I also want to thank Professor Ravichandran and Dr. Owen Kingstedt for their data of the thermal effects in Mg polycrystals. In addition, I am thankful for collaborations with Mauricio Ponga and all his valuable advice during my career search. At last, I want to thank our ARL collaborators Dr. Rich Becker and Dr. John Clayton for their advice on the research work.

It has been a wonderful experience to be part of the Kochmann Research Group. I want to thank my collegues for all the help they provided. In particular, Charles Wojnar has always been a good friend and wonderful officemate. I appreciate his help on correcting all the typos and English phrases over the years and I wish him great success in his future career. I am very lucky to have Jeff Amelang as my officemate and his help addressing all my programming questions and the difficult bugs I came across. I deeply appreciate his effort on developing the finite element framework, which is essential for all the simulation results shown in this thesis. In addition, I want to thank Alex Zelhofer and Ishan Tembhekar for devoting their time to maintain the code and all the new features they have added. I wish to express my appreciation to everyone else in the group: Vidyasagar, Neel Nadkarni, Greg Phlipot, Wei Lin Tan, and Michael Frazier.

I want to thank all my friends for their help at Caltech, especially those from the Caltech Chinese community, who have made my life outside of research more colorful. I enjoyed all the road trips and hikes with them.

At last, I want to express my deep appreciation to my parents for their unconditional support over the years. They have sacrificed so much of their life to support me in my pursuit of higher education. I am always proud to have them as my family.

Abstract

Due to their high specific strength and low density, magnesium and magnesium-based alloys have gained great technological importance in recent years. However, their underlying hexagonal crystal structure furnishes Mg and its alloys with a complex mechanical behavior because of their comparably smaller number of energetically favorable slip systems. Besides the commonly studied slip mechanism, another way to accomplish general deformation is through the additional mechanism of deformation-induced twinning. The main aim of this thesis research is to develop an efficient continuum model to understand and ultimately predict the material response resulting from the interaction between these two mechanisms.

The constitutive model we present is based on variational constitutive updates of plastic slips and twin volume fractions and accounts for the related lattice reorientation mechanisms. The model is applied to single- and polycrystalline pure magnesium. We outline the finite-deformation plasticity model combining basal, pyramidal, and prismatic dislocation activity as well as a convexification-based approach for deformation twinning. A comparison with experimental data from single-crystal tension-compression experiments validates the model and serves for parameter identification. The extension to polycrystals via both Taylor-type modeling and finite element simulations shows a characteristic stress-strain response that agrees well with experimental observations for polycrystalline magnesium. The presented continuum model does not aim to represent the full details of individual twin-dislocation interactions, yet it is sufficiently efficient to allow for finite element simulations while qualitatively capturing the underlying microstructural deformation mechanisms.

Contents

List of Figures

List of Tables

Published Content

Some parts of **Chapter 3, 4, 5 and 6** of this thesis were previously published in the International Journal of Plasticity (Chang and Kochmann, 2015). All other work is original to this thesis.

Chapter 1

Introduction

1.1 Magnesium and hexagonal close packed (hcp) materials

Magnesium and magnesium-based alloys have gained great technological importance due to their excellent strength-to-weight ratios, making them ideal candidates e.g., for the transportation industry or for defense applications. However, its hexagonal crystal structure furnishes Mg and its alloys with a non-trivial mechanical performance which involves a substantial tension-compression asymmetry (Avedesian et al., 1999; Ball and Prangnell, 1994; Kurukuri et al., 2014; Lou et al., 2007) and a comparably low ductility at low holonomous temperature (Hauser et al., 1956; Tegart, 1964), as well as a pronounced deformation anisotropy, see e.g., the recent studies by Agnew and Duygulu (2005), Lou et al. (2007), and Stanford et al. (2011). In Figure 1.1, we show an experimental observation from Foley et al. (2011) to illustrate the anisotropic response of Mg. In this study, textured Mg polycrystals (taken from cold-rolling and ECAE processes) are loaded in different directions and the corresponding stress-strain curves are recorded. From this figure, we observe:

- the material shows different ultimate stresses in each case, e.g., loading under 37° from the longitudinal direction (LD) of the ECAE sample results in the highest ultimate stress (about 400MPa) and in contrast, loading in the transverse direction (TD) of rolled sample shows the lowest stress;

- the stress-strain shapes differ, which indicates different deformation mechanisms occur in each case: loading in the TD and FD shows a two-stage S-shaped response which results from twinning-dominated deformation followed by a reorientation of the slip systems while other

curves show a typical slip hardening behavior.

- ductility varies with different loading directions, i.e., deformation dominated by twinning (FD and TD) tends to have a more extended plastic range than slip dominated deformation, and loading in the FD seems to have higher ultimate stress and ductility at the same time.

Therefore, the successful implementation of Mg-based materials in everyday applications essentially hinges upon suitable models to accurately describe, thoroughly understand, and reliably predict the complex material response over wide ranges of loading and environmental conditions.

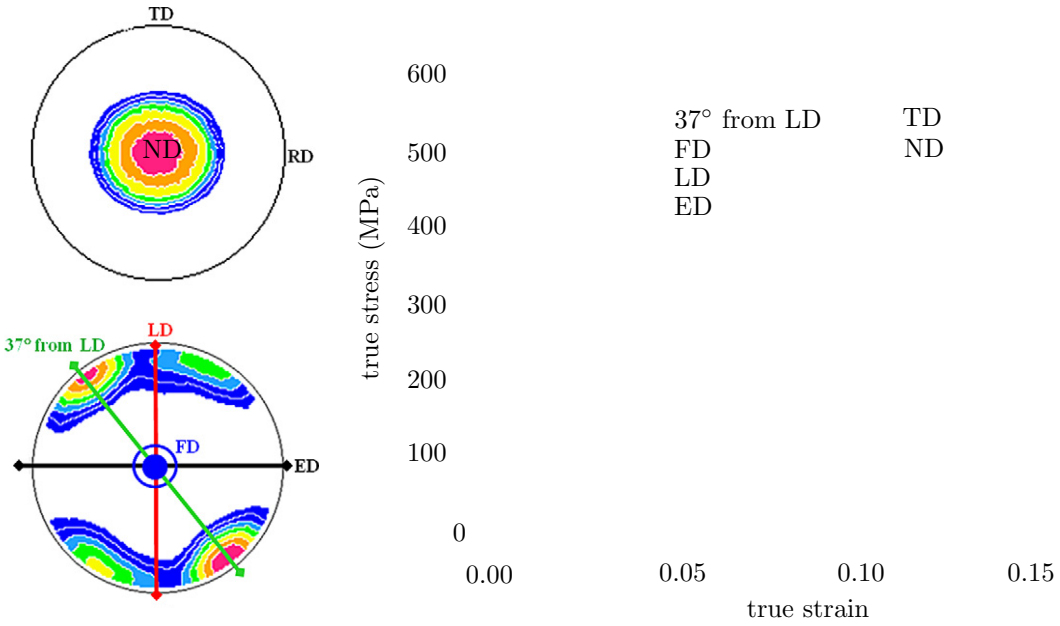

Figure 1.1: Experimental results of Mg polycrystals from Foley et al. (2011) show highly anisotropic stress-strain response when loading in different directions. Left figure shows the (0001)-pole figures of an AZ31 polycrystal after cold-rolling process (top) and ECAE process (bottom). The right figure shows the stress-strain response when the samples are loaded in different directions.

The origin of the complex mechanical response lies in the hcp crystallography of Mg with a specific lattice aspect ratio of $c/a = 1.624$ (Christian and Mahajan, 1995). While the crystal structure offers several slip systems that operate in the basal plane, it severely restricts out-of-plane dislocation activity due to the relatively high critical resolved shear stresses of all non-basal systems, see e.g., Staroselsky and Anand (2003). Instead, if the sample is deformed parallel to the c-axis, stress relaxation can be accommodated by deformation twinning which, by itself, is

fairly well understood and leads to a reorientation of the crystal lattice by rotations or reflections about characteristic twin systems (Christian and Mahajan, 1995). In Figure 1.2 and Table 1.1, we summarize the commonly observed slip/twin systems and the corresponding critical twinning shear strain in Mg. Since the pyramidal $\langle c + a \rangle$ system is generally considered to be harder to activate at room temperature, the number of slip systems is not sufficient for general homogeneous deformation, e.g., deformations along the c-axis. Thus, an additional mechanism such as twinning must occur to accommodate general deformations. The coexistence of slip and twinning in Mg leads to a complex deformation behavior with rich microstructural phenomena that are responsible for the macroscopic response, cf. Hauser et al. (1956), Reed-Hill and Robertson (1958), Roberts and Partridge (1966), Wonsiewicz and Backofen (1967) and Ando and Tonda (2000). The exact deformation modes are still subject to controversial discussions which have raised a number of open questions, see e.g., Lilleodden (2010) for a more recent discussion.

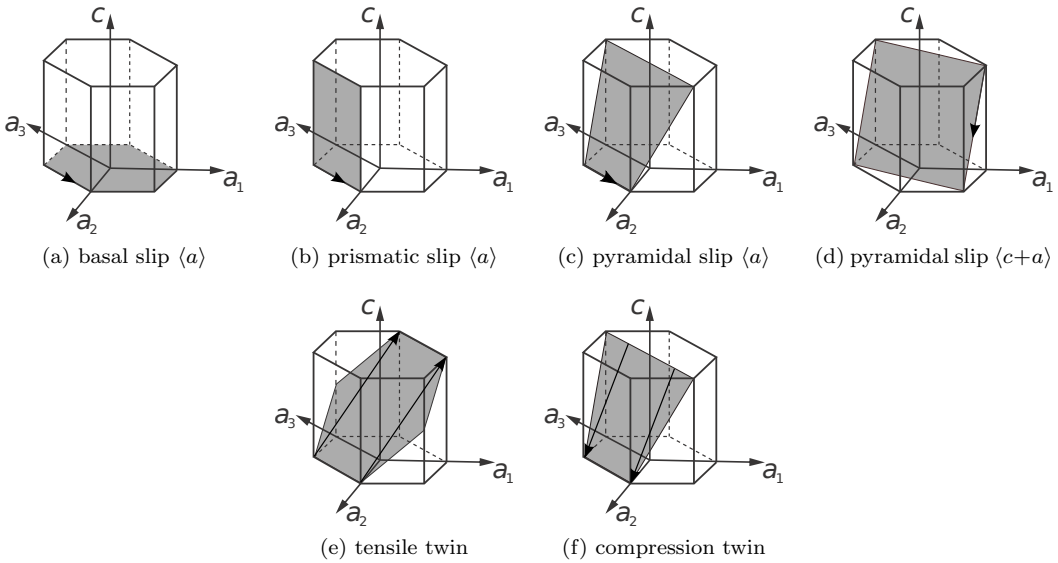

(a) basal slip $\langle a \rangle$ (b) prismatic slip $\langle a \rangle$ (c) pyramidal slip $\langle a \rangle$ (d) pyramidal slip $\langle c+a \rangle$

(e) tensile twin (f) compression twin

Figure 1.2: Schematic view of the primary slip and twin systems observed in Mg.

1.2 Continuum modeling of Mg and Mg alloys

A variety of models operating on different length scales have been proposed to bridge the gap between macroscopic observations and microstructural mechanisms in Mg, from the atomistic level

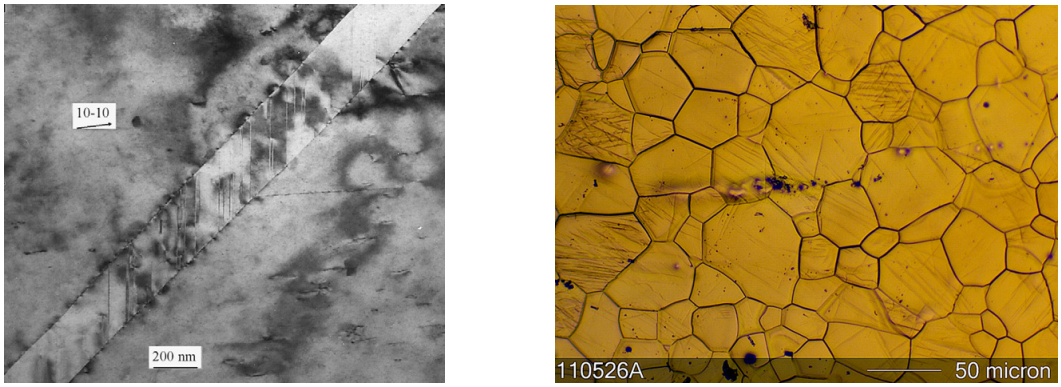

Figure 1.3: Experimental evidence of slip and twinning in Mg. Left: TEM observation of slip and twin (Hazell et al., 2012); right: micrograph of twinning in grains of shocked F-grade Mg alloy (Guillemer et al., 2011).

all the way up to continuum-mechanics descriptions. Here, we limit our scope to the latter and aim at incorporating as much lower-scale information about specific slip and twinning modes as necessary (but not more) to accurately and efficiently describe the effective response of single- and polycrystalline Mg. One natural way to incorporate twinning into the crystal plasticity model is through the phase field approach (Clayton and Knap, 2011a,b). In this approach, twinning is explicitly expressed by an order parameter η which accepts a value between 0 and 1 indicating whether the material is in the parent or twinned orientations, respectively. In combination with gradient plasticity models, see e.g., Fleck and Hutchinson (1997), Kochmann and Le (2008, 2009b) and Hurtado and Ortiz (2012), we can capture detailed microstructural characteristics such as twin interface evolution and grain boundary dislocation pile-up. To elaborate on this theory, let us consider a small strain problem. Suppose the material exhibits n active slip systems denoted by pairs $(\boldsymbol{s}_\alpha, \boldsymbol{m}_\alpha)$ representing the slip directions and slip plane normals, respectively. The plastic

type	slip/twin plane	slip/twinning direction	number of systems	γ_{tw}
basal slip:	$\{0001\}$	$\langle 11\bar{2}0\rangle$	3	-
prismatic slip:	$\{1\bar{1}00\}$	$\langle 11\bar{2}0\rangle$	3	-
pyramidal slip $\langle a\rangle$:	$\{1\bar{1}01\}$	$\langle 11\bar{2}0\rangle$	6	-
pyramidal slip $\langle c+a\rangle$:	$\{11\bar{2}2\}$	$\langle \bar{1}\bar{1}23\rangle$	6	-
tensile twin:	$\{10\bar{1}2\}$	$\langle \bar{1}011\rangle$	6	0.129
compression twin (rare):	$\{10\bar{1}1\}$	$\langle \bar{1}012\rangle$	6	1.066

Table 1.1: Properties of the various slip and twin systems found in Mg and included in the model.

distortion produced by slip is the sum from all systems,

$$\boldsymbol{\beta} = \sum_{\alpha=1}^{n} \gamma_\alpha \boldsymbol{s}_\alpha \otimes \boldsymbol{m}_\alpha, \tag{1.1}$$

where $\boldsymbol{\gamma} = [\gamma_1, ..., \gamma_n]$ are the slips on each system. Consequently, the slip contributions to the plastic strain are the symmetric part of the plastic distortion,

$$\boldsymbol{\varepsilon}_\mathrm{p} = \frac{1}{2}(\boldsymbol{\beta} + \boldsymbol{\beta}^\mathrm{T}). \tag{1.2}$$

In addition to slip, the material also presents a twin system $(\boldsymbol{a}, \boldsymbol{n})$: the twinning shear direction and the twinning plane normal. Thus, we can write out the plastic strain due to twinning,

$$\boldsymbol{\varepsilon}_\mathrm{tw} = \varphi(\eta)\gamma_\mathrm{tw}\,\mathrm{sym}(\boldsymbol{a} \otimes \boldsymbol{n}), \tag{1.3}$$

where γ_tw is the critical twinning shear strain, determined from the underlying lattice structure, and $\varphi(\eta)$ is an interpolation function used to interpolate the order parameter to the strain field, satisfying the conditions $\varphi(0) = 0$ and $\varphi(1) = 1$. A specific choice of φ can be found in Clayton and Knap (2011a).

Following the above notations, the material is characterized by the Helmholtz free energy density,

$$W(\nabla \boldsymbol{u}, \boldsymbol{\gamma}, \eta) = W_\mathrm{el}(\boldsymbol{\varepsilon}_\mathrm{e}, \eta) + W_\mathrm{p}(\boldsymbol{\gamma}) + W_\rho(\nabla\boldsymbol{\gamma}) + W_\mathrm{tw}(\eta) + W_\mathrm{inter}(\nabla\eta). \tag{1.4}$$

In this formula, W_el is the elastic energy depending on the elastic infinitesimal strain tensor $\boldsymbol{\varepsilon}_\mathrm{e} = \boldsymbol{\varepsilon} - \boldsymbol{\varepsilon}_\mathrm{p} - \boldsymbol{\varepsilon}_\mathrm{tw}$, where $\boldsymbol{\varepsilon} = \frac{1}{2}(\nabla\boldsymbol{u} + \nabla\boldsymbol{u}^\mathrm{T})$ is the total infinitesimal strain tensor, calculated through the displacement field $\boldsymbol{u}$. $W_\mathrm{p}(\boldsymbol{\gamma})$ and $W_\rho(\nabla\boldsymbol{\gamma})$ are the energies stored in the slip systems, where W_p is used to capture the slip hardening behavior and W_ρ is the so-called dislocation network energy characterizing the interactions between dislocations and/or dislocation self-energies. W_ρ depends on a scalar dislocation density,

$$\rho = \sum_{\alpha=1}^{n} \rho_\alpha, \qquad \rho_\alpha = \frac{1}{b}|\boldsymbol{s}_\alpha \cdot \nabla\gamma_\alpha|, \tag{1.5}$$

where b is the magnitude of the Burger's vector. The scalar dislocation density is obtained through Nye's dislocation density tensor $\boldsymbol{\alpha} = \operatorname{curl}\boldsymbol{\beta}$ (Nye, 1953). A detailed derivation can be found in Berdichevsky (2006). Various forms of W_ρ have been proposed to capture different aspects of dislocation structures. For a brief selection, see the line tension model (linear) by Ortiz and Repetto (1999), the quadratic energy density proposed by Gurtin and Anand (2007), or the logarithmic energy for capturing dislocation saturation behavior (Berdichevsky, 2006).

Similarly, twinning is described via the twinning energy $W_{\text{tw}}(\eta)$ and interface energy $W_{\text{inter}}(\nabla\eta)$. W_{tw} is usually assumed as a nonconvex double-well potential with minimum residing at 0 and 1, since the material is assumed to not store energy in the pure parent or twinned orientations. The interface energy depends on the gradient of the order parameter, preventing the material forming fine twins. One particular choice of twinning and interface energy is from Cahn and Hilliard (1958),

$$W_{\text{tw}}(\eta) = A\eta^2(1-\eta)^2, \qquad W_{\text{inter}} = \boldsymbol{\kappa} : (\nabla\eta \otimes \nabla\eta), \tag{1.6}$$

where A is a material constant, and $\boldsymbol{\kappa}$ is a second-order tensor characterizing the interface energy (and oftentimes assumed isotropic). Following an energy minimization approach, the solution for the displacements, slip field $\boldsymbol{\gamma}$, and order parameter η are the minimizers of the free energy over all feasible solutions for given boundary conditions.

Figure 1.4 through Figure 1.6 show results from the application of the above combination of gradient plasticity theory and phase field model. In Figure 1.4, a pillar having only a single slip system was compressed and the resulting slip and dislocation density are plotted. In this simulation, the dislocation network energy is chosen from the line tension model (Ortiz and Repetto, 1999), increasing linearly with respect to the scalar dislocation density. The penalty from the dislocation network energy aims to reduce the slip gradient, and because of the zero slip boundary conditions imposed here, a sharp slip gradient appears near the grain boundary, which serves as a barrier preventing dislocations from penetrating. Therefore, dislocations pile up near the boundary, leaving the center of the sample almost dislocation-free. When plotting the stress-strain curves for different pillar sizes, we observe strong size effects, i.e., the stress required to achieve the same deformation is higher with smaller samples, which is known as grain boundary strengthening (Hall, 1951; Petch, 1953). In Figure 1.5, a square sample with a single twin system was deformed under simple shear and the order parameter field is plotted to identify the twinned and untwinned regions for different

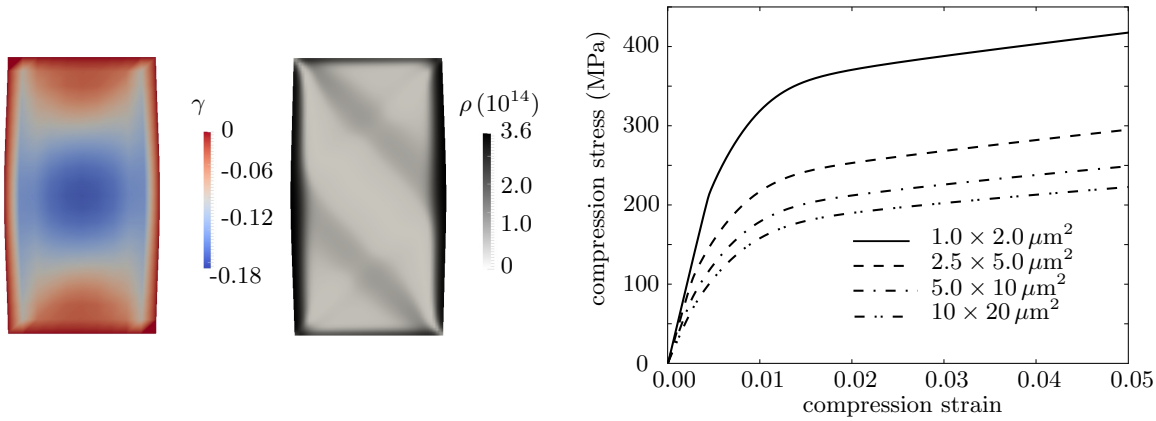

Figure 1.4: Pillar compression simulation using the gradient plasticity theory shows dislocation pileups at the grain boundary and size effects. The right figure includes results for four different pillar sizes of rectangular shape in two dimensions.

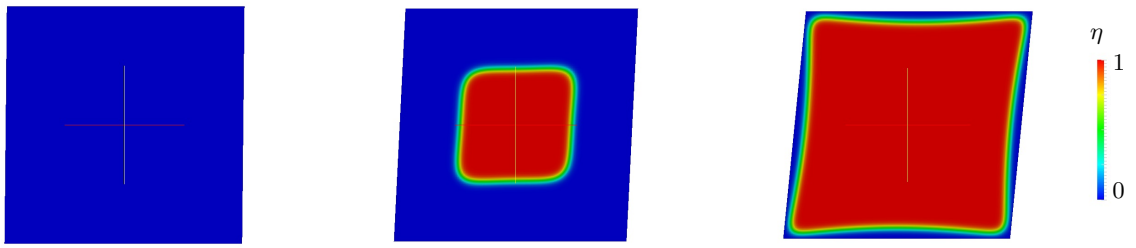

Figure 1.5: Simple shear simulation of one twin system using the phase field model shows twin nucleation and evolution.

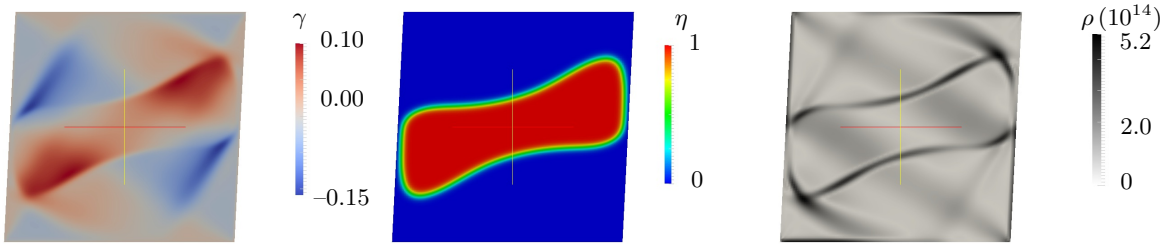

Figure 1.6: The combined simulation (using gradient plasticity plus twinning phase field) predicts dislocation pile-up at the twinning interface.

applied shear strains. From this result, we observe that the twin nucleates and evolves as we deform the sample, and ultimately reaches the boundary where we deliberately set the order parameter to 0. Finally, we put the two theories together to study the interactions between slip and twinning. A simple shear test was performed on a single slip/twin material and the relevant slip/twin fields at 5% strain are shown in Figure 1.6. In this plot, we see strong interactions between slip and twinning: the shape of the twinned region is influenced by the presence of slip. Furthermore, in addition to the grain boundaries, which attract dislocations as shown in Figure 1.4, the twin interface serves as an additional source for dislocations to accumulate, which agrees with simulation results by Kondo et al. (2014).

Although the combination of gradient plasticity and phase field theory provides us with an effective way to understand detailed interactions between slip and twinning, the practical application of this theory presents us with certain difficulties. Besides the scale separation problem with slip and twinning, discussed in Section 1.3, the different modeling principles of these two mechanisms create additional complexities when we include too many slip/twin systems. In addition, the choice of the nonconvex energy in (1.6) creates additional numerical challenges for solving a nonconvex optimization problem. Thus, we need to develop an efficient model that can both capture the interaction between slip and twinning and at the same time be numerically advantageous.

Since dislocation glide is one of the primary inelastic mechanisms, many models have borrowed concepts from conventional crystal plasticity (Asaro, 1983; Asaro and Rice, 1977; Hill, 1966; Rice, 1971; Simo, 1988a,b). Deformation twinning was included by introducing each twin system as an additional slip system (often referred to as *pseudo slip systems*) (Agnew et al., 2001; Graff et al., 2007; Van Houtte, 1978). Experiments on single- and polycrystalline Mg (Kelley and Hosford, 1968a,b) have confirmed the importance of the lattice reorientation due to twinning, which was not accounted for in those early models. In addition, the coexistence of untwinned and twinned domains and simultaneous activity of dislocations in both orientations can significantly affect the stress-strain response. Recently, several approaches have been reported that aim to overcome these deficiencies by including more microstructural details, see e.g., Staroselsky and Anand (2003), Zhang and Joshi (2012) and Wang et al. (2010), by employing a flow rule presented by Kalidindi (2001) to capture the effects of lattice reorientation. Among those, closest to our model presented here are those of Homayonifar and Mosler (2011, 2012) and Zhang and Joshi (2012).

Homayonifar and Mosler (2011, 2012) presented variational models whose crystal plasticity

basis is enriched by energy relaxation schemes to describe the effects of deformation twinning, cf. James (1981), Ball and James (1987) and Kochmann and Hackl (2011). In this approach, the non-(quasi)convex energy landscape is replaced by either a rank-one-convex envelope (which is realized by sequential lamination to identify energy-minimizing fine-scale laminate patterns) (Ortiz and Repetto, 1999) or by full convexification (in which case lamellar patterns are free of the constraint of mechanical compatibility), see also Glüge et al. (2010). While these approaches have a solid mathematical foundation and offer beneficial extensions and numerical advantages owing to the variational structure, they are also numerically costly and simulation examples have been limited to material point calculations due to the computational complexity. On the other hand, Zhang and Joshi (2012) introduced a crystal plasticity-based formulation with pseudo-slip systems to accommodate twinning, enriched by a lattice reorientation procedure to account for slip in both parent and twinned orientations. Their model accounts for many details of the slip-twinning interactions, yet it uses a conventional crystal plasticity formulation based on direct updates of the inelastic variables and therefore without a variational structure. In this thesis, we combine both concepts into an efficient variational model for Mg accounting for slip-twinning interactions without the necessity of energy relaxation algorithms by using variational constitutive updates (Comi et al., 1991, 1992; Ortiz and Stainier, 1999).

Variational models offer various advantages from both a numerical-mathematical and a physical viewpoint. By using variational constitutive updates, the internal state variables and the deformation mapping follow from minimization of the same potential, which circumvents the complexity of having to solve for both types of variables simultaneously. In addition, the implicit update of the internal variables in the variational approach improves the efficiency by allowing for considerably larger time steps compared to explicit schemes, which in turn enables the simulation of significantly more complex physical scenarios. Owing to their underlying minimum energy principle, variational models also offer a convenient foundation for error estimation and mesh adaptation, see e.g., Radovitzky and Ortiz (1999), Thoutireddy and Ortiz (2004) and Mosler and Ortiz (2006). The existence of solutions and the formation of fine-scale microstructure can be analyzed by well-established techniques, see e.g., Ball and James (1987), Ortiz and Repetto (1999) and Carstensen et al. (2002). Variational constitutive updates have been applied to a wide range of material models, including viscoelasticity and viscoplasticity (Ortiz and Stainier, 1999), crystal plasticity (Carstensen et al., 2002; Ortiz and Repetto, 1999; Ortiz et al., 2000), and strain gradient plasticity (Qiao, 2009);

they also admit a variational, thermodynamically-consistent extension to thermo-mechanical coupling, see e.g., Yang et al. (2006).

Our approach is similar in spirit and is based on variational constitutive updates to describe the slip-twinning interactions in Mg and Mg alloys (although we focus on pure Mg here, the presented framework can easily be extended to other hcp metals). Our model uses a finite-strain crystal plasticity formulation which accounts for the lattice reorientation due to twinning on the flow rule level similarly to Zhang and Joshi (2012). All prevailing slip and twin systems and interactions between them are accounted for by appropriate hardening energies and dissipation potentials.

1.3 Motivation of twin volume fractions from energy relaxation theory

As discussed in the previous sections, slip and twinning both contribute to the deformation of Mg and other hcp materials for crystallographical reasons. In Figure 1.7, we show two experimental evidences. Shown on the left is a pillar compression example from Aitken et al. (2015), where the Mg sample is undergoing significant basal slip-dominated deformation. In this experiment, the length scales of the pillars are between 300nm to 5000nm. However, on the twinning side, previous researchers, e.g., Yu et al. (2012), found that in most cases the typical twin spacing can be on the order of several layers of atoms, forming nano-twins, as shown in Figure 1.7. This scale discrepancy between slip and twinning imposes modeling difficulties: since twinning occurs at the nanoscale, typically several layers of atoms, conventional models based on the continuum assumption become questionable. Furthermore, the phase field model as discussed in Section 1.2 is capable of capturing detailed twin nucleation and evolution. However, in order to study both slip and twinning in the same computational model, we need fine mesh resolutions down to the lower nanoscale to model twin interfaces while dislocation and grain boundaries reside on the scale of hundreds of nanometers to microns. This results in extremely high computational costs. In either case, direct modeling of slip and twinning in the same continuum model is neither plausible nor realistic. We need to come up with a technique that can capture the scale separation between slip and twinning but at the same time is computationally efficient.

The key concept of our approach is modeling the evolution of twin volume fraction, which are related to the energy relaxation approach (Homayonifar and Mosler, 2011, 2012; Ortiz and Repetto,

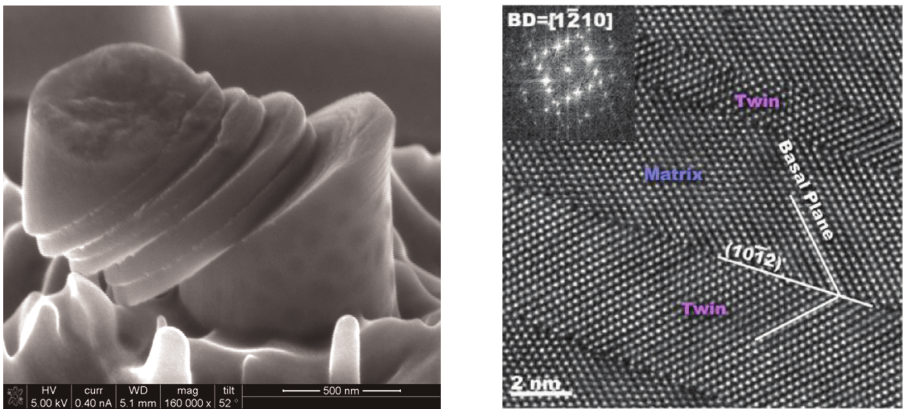

Figure 1.7: Experimental evidence of deformation mechanisms and the scale separation observed in Mg. Left: dislocation activity happens at a larger scale, typically hundreds of nanometers to several micrometers (Aitken et al., 2015); right: twin spacings usually occupy several layers of atoms (Yu et al., 2012), and are on the order of several nanometers.

1999). To motivate this concept, we start with a simple example. Suppose we have material exhibiting a single twin system, separating the parent and twinned orientations. The system is defined by the twinning habit plane normal $\boldsymbol{n}$, twinning shear direction $\boldsymbol{a}$ and the critical shear strain γ^{tw}, all of which are material parameters determined from the underlying crystal structure. Following Ortiz and Repetto (1999), we assume the material forms infinitely fine twins so that we can introduce the twinning ratio of this system, denoted by λ, to describe the volume fractions of materials that are in the twinned orientation.

We consider a small-strain experiment with an imposed global strain denoted by $\boldsymbol{\varepsilon}$. In order to determine the material response, all we need to know are the effective twinning ratio and the corresponding strains in the parent and twinned orientations, $\boldsymbol{\varepsilon}_1$ and $\boldsymbol{\varepsilon}_2$, respectively. By strain compatibility, we have

$$(1-\lambda)\boldsymbol{\varepsilon}_1 + \lambda\boldsymbol{\varepsilon}_2 = \boldsymbol{\varepsilon}, \tag{1.7}$$

meaning that the average strain from the two orientations should equal the total strain. In addition, Hadamard compatibility (rank-one-compatibility) requires

$$\boldsymbol{\varepsilon}_1 - \boldsymbol{\varepsilon}_2 = \text{sym}(\boldsymbol{a}' \otimes \boldsymbol{n}), \tag{1.8}$$

for some vector $\boldsymbol{a}'$. Furthermore, in the twinned region, the material has already gone through

plastic deformation, and thus the elastic strain in the twinned orientation is $\boldsymbol{\varepsilon}_2 - \boldsymbol{\varepsilon}_{\mathrm{tw}}$, where the plastic strain equals the twinning strain defined by $\boldsymbol{\varepsilon}_{\mathrm{tw}} = \gamma_{\mathrm{tw}}\,\mathrm{sym}(\boldsymbol{a} \otimes \boldsymbol{n})$. Following an energy minimization approach, we seek minimizers $(\lambda, \boldsymbol{\varepsilon}_1, \boldsymbol{\varepsilon}_2, \boldsymbol{a}')$ of the total strain energy density,

$$(\lambda, \boldsymbol{\varepsilon}_1, \boldsymbol{\varepsilon}_2, \boldsymbol{a}') = \arg\min\,(1-\lambda)W(\boldsymbol{\varepsilon}_1) + \lambda W(\boldsymbol{\varepsilon}_2 - \boldsymbol{\varepsilon}_{\mathrm{tw}}) \tag{1.9}$$

with constraints (1.7), (1.8), and $0 \leq \lambda \leq 1$.

Let us consider a plane-strain problem, i.e.,

$$\boldsymbol{\varepsilon} = \begin{bmatrix} \varepsilon_{11} & \varepsilon_{12} \\ \varepsilon_{12} & \varepsilon_{22} \end{bmatrix}, \tag{1.10}$$

and the twinning system lies in the deformed plane, i.e., in the x-y-plane, with twinning normal direction $\boldsymbol{n} = [-\sin\phi, \cos\phi]^{\mathrm{T}}$, and shear direction $\boldsymbol{a} = [\cos\phi, \sin\phi]^{\mathrm{T}}$. To solve the energy minimization problem (1.9), we make the following ansatz to automatically satisfy constraints (1.7) and (1.8):

$$\boldsymbol{\varepsilon}_1 = \boldsymbol{\varepsilon} - \lambda\,\mathrm{sym}(\boldsymbol{a}' \otimes \boldsymbol{n}), \tag{1.11a}$$

$$\boldsymbol{\varepsilon}_2 = \boldsymbol{\varepsilon} + (1-\lambda)\,\mathrm{sym}(\boldsymbol{a}' \otimes \boldsymbol{n}). \tag{1.11b}$$

For simplicity, we consider an isotropic linear elastic material with elastic energy

$$W(\boldsymbol{\varepsilon}) = \frac{\lambda}{2}\,\mathrm{tr}^2(\boldsymbol{\varepsilon}) + \mu\,\boldsymbol{\varepsilon} \cdot \boldsymbol{\varepsilon}, \tag{1.12}$$

where λ and μ are the Lamé constants. Substituting (1.11) into (1.9) and solving at a stationary point, we can find an analytical solution for this problem,

$$\lambda = \frac{2\varepsilon_{12}\cos 2\phi + (\varepsilon_{22} - \varepsilon_{11})\sin 2\phi}{\gamma^{\mathrm{tw}}}, \tag{1.13a}$$

$$\boldsymbol{a}' = \gamma^{\mathrm{tw}}[\cos\phi, \sin\phi]^{\mathrm{T}}. \tag{1.13b}$$

Note that this solution only applies if $\lambda \in [0; 1]$. Otherwise, the material is either untwinned ($\lambda = 0$) or fully twinned ($\lambda = 1$). We need to mention that although the unknown vector $\boldsymbol{a}'$ turns out to

point in the same direction as the twinning shear, we cannot assume this property in the first place in (1.8), where only the rank-one jump condition is used.

We illustrate the material behavior of this model system using simple shear tests ($\varepsilon_{12} = \frac{1}{2}\gamma$, $\varepsilon_{11} = \varepsilon_{22} = 0$) with different twin systems ($\phi = 0°$ and $15°$). In Figure 1.8, we plot the resulting average stored energy (W_{relaxed}) calculated through (1.9) versus the average shear deformation γ. For comparison, we also plot the unrelaxed energy curves W_{parent} and W_{twin}, where all the material is either assumed solely in the parent or twinned orientations, respectively, and mixing is not allowed. From both results in Figure 1.8, we see that the energy minimization approach identifies the optimal twinning ratio that rank-one-convexifies the energy envelopes: if the deformation is in an appropriate range so that the resulting twinning ratio in (1.13a) is between 0 and 1, the material's energy density is relaxed by the existence of twinning. Otherwise, the energy follows the unrelaxed energy curves either of the untwinned or the twinned orientation. In principle, this approach can be used to study second-or higher-order laminates to study slip and twinning interactions in hcp metals involving multiple deformation systems, see e.g., Homayonifar and Mosler (2011, 2012). However, this often requires complex optimization over a nonconvex energy profile, which is numerically expensive and intractable when dealing with finite deformation. In the following chapters, we will present our alternative approach that treats twinning as additional slip systems by using the twinning ratios as internal variables. Building on the conventional crystal plasticity models, we will study slip and twinning in Mg and Mg alloys in a more efficient way.

Lastly, we need to mention that by using the concept of twin volume fractions, the twinning interface energy is not included in the model. The underlying energy minimization principle only determines the energy-minimizing volume fractions and not their exact laminate spacings; thus the minimizing sequence may lead to infinitely-fine laminate microstructures between the parent and twinned orientations, see Bhattacharya (1998) for detailed review. In reality, this would not happen because the twinning interface energy grows rapidly when many twins are present in the material. However, by defining an effective twinning ratio at each material point and not worrying about the associated length scales of the individual twin laminate, we capture the twinning behavior at the lower scales.

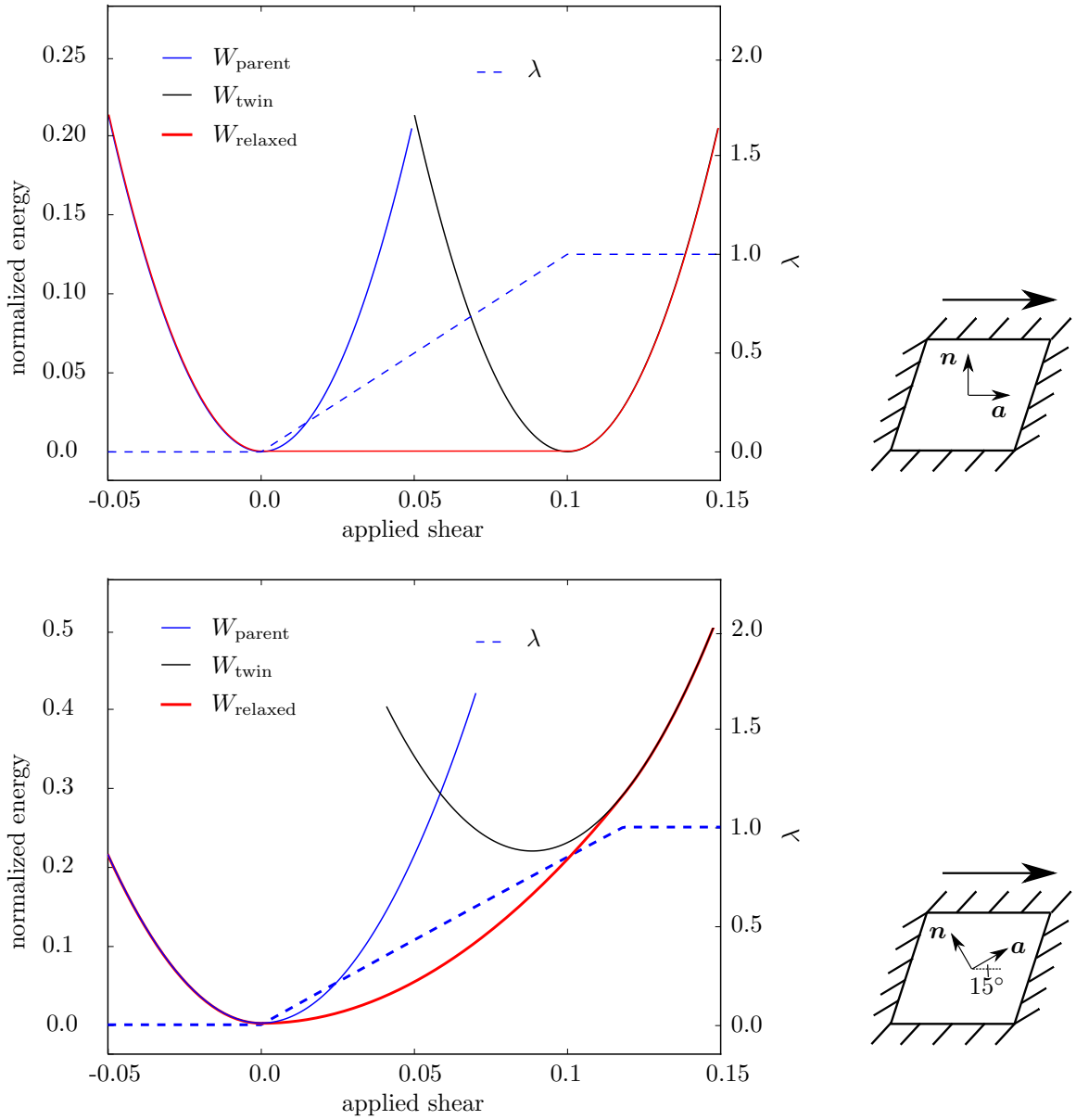

Figure 1.8: Relaxation of the total energy density from a simple shear test due to twinning with different twin system orientations.

1.4 Outline of this thesis

In the following chapters, we begin our discussion with a brief review of continuum mechanics and crystal plasticity theories in Chapter 2, based on which we develop the magnesium model. In Chapter 3, we introduce the model based on the continuum variational approach, where slip and twinning ratios are treated as the primary internal variables. The interactions between slip and twinning are modeled by a modified flow rule to explicitly accounts for the reorientation of the crystal lattice due to the presence of twinning. In Chapter 4, we describe the numerical implementation details of the model via both variational updates and the conventional explicit approach. In Chapter 5 and 6, we go through a set of examples to understand the material behavior using our model. First, we compare with the phase field approach and obtain the model parameters by fitting into experimental data from Kelley and Hosford (1968a,b). Then we apply our model to predict the texture evolution of Mg polycrystals during the cold rolling process. In Chapter 7, we present results from simulations with large numbers of grains to study the material response of textured Mg polycrystals using a Taylor model and finite element simulations for comparison with experimental observations. We conclude with a summary of the main result of this thesis research and possible future directions in Chapter 8.

Chapter 2

Theoretical Background

For completeness, in this chapter, we give a brief review of the fundamentals of the constitutive relations and the internal variable approach within classical continuum mechanics, which are used to develop the crystal plasticity theory. The usage of additional internal variables to describe the thermodynamic state of solid materials with general heat conduction and viscosity was first derived by Coleman and Noll (1963), and later extended by Hill (1966), Rice (1971), and Asaro and Rice (1977) to study solids with crystalline structures. A variationally-consistent reformulation of the theory was established by Ortiz and Repetto (1999) and Ortiz and Stainier (1999), where the conventional constitutive relations were recovered by computing updates of the internal variables via minimization of a newly-introduced rate functional, which showed numerical and mathematical advantages over previous methods.

The rest of the chapter is arranged as follows: we start with a brief summary of the basic kinematics in continuum mechanics and plasticity in Section 2.1. In Section 2.2, we follow the discussions from Ortiz and Stainier (1999) and Homayonifar and Mosler (2011) to derive the thermodynamic equilibrium relations that govern the internal states of crystalline solids, in which plasticity results from dislocation motion on the slip planes. In Section 2.3, the variational framework from Ortiz and Stainier (1999) is applied to crystal plasticity, and suitable potentials are derived to construct the rate functional, the minimization of which recovers the constitutive relations introduced. For completeness, we give a brief review of the thermo-mechanical coupling in the crystal plasticity model and derive the governing law for heat production and temperature evolution in Section 2.4. The discussion follows the variational approach of Yang et al. (2006).

2.1 Kinematics of plastic deformation

We begin our discussion by reviewing the kinematics of plasticity theory in a finite deformation setting. Suppose a body occupies a certain domain Ω in the reference configuration and we label each of the material points by its position $\boldsymbol{X}$. We adopt a Lagrangian description of motion and define a deformation mapping $\boldsymbol{\varphi}(\boldsymbol{X}) : \Omega \to \mathbb{R}^3$ that maps the body from the reference configuration to the current configuration. To eliminate the effects of rigid body translation, we define the deformation gradient,

$$\boldsymbol{F}(\boldsymbol{X}) = \frac{\partial \boldsymbol{\varphi}(\boldsymbol{X})}{\partial \boldsymbol{X}}, \qquad \boldsymbol{X} \in \Omega, \tag{2.1}$$

which contains all the information related to the local metrics change of the body.

Plastic or viscoplastic solids are characterised by a permanent or plastic deformation, measured by plastic deformation gradient $\boldsymbol{F}_{\mathrm{p}}$, which does not recover upon unloading and leaves the crystal lattice undistorted or unrotated. In incompressible plasticity, there is no volume change associated with plastic deformation, i.e., the plastic deformation satisfies the condition

$$\det(\boldsymbol{F}_{\mathrm{p}}) = 1. \tag{2.2}$$

In addition to plastic deformation, the rotation and distortion of the lattice are described by the elastic deformation gradient $\boldsymbol{F}_{\mathrm{e}}$. Following Lee (1969), the total deformation gradient (2.1) follows a multiplicative decomposition,

$$\boldsymbol{F} = \boldsymbol{F}_{\mathrm{e}}\boldsymbol{F}_{\mathrm{p}}. \tag{2.3}$$

In this decomposition, the plastic deformation maps the reference configuration to some intermediate configuration and the superimposed elastic deformation further maps the body from intermediate configuration to the current configuration. Following this decomposition, the velocity gradient is decomposed additively,

$$\boldsymbol{l} = \dot{\boldsymbol{F}}\boldsymbol{F}^{-1} = \boldsymbol{l}_{\mathrm{e}} + \boldsymbol{l}_{\mathrm{p}} = \boldsymbol{l}_{\mathrm{e}} + \boldsymbol{F}_{\mathrm{e}}\,\tilde{\boldsymbol{l}}_{\mathrm{p}}\,\boldsymbol{F}_{\mathrm{e}}^{-1} \qquad \text{with} \qquad \boldsymbol{l}_{\mathrm{e}} = \dot{\boldsymbol{F}}_{\mathrm{e}}\boldsymbol{F}_{\mathrm{e}}^{-1}, \quad \tilde{\boldsymbol{l}}_{\mathrm{p}} = \dot{\boldsymbol{F}}_{\mathrm{p}}\boldsymbol{F}_{\mathrm{p}}^{-1}, \tag{2.4}$$

where the dot denotes the material derivative with respect to time.

2.2 Constitutive relations of crystal plasticity

Based on the kinematics we have discussed, in this section we adopt the internal variable formalism (Lubliner, 1972, 1973), which extends the discussion of Coleman and Noll (1963), to derive the constitutive laws that govern the material behavior of crystalline solids. In conventional crystal plasticity, the plastic deformation results from dislocation motion. Suppose the crystal structure processes n slip systems and we consider a set of internal variables $\boldsymbol{\epsilon} \in \mathbb{R}^n$, which are interpreted as the accumulated slips caused by dislocation motion on each system denoted by the pairs of Burger's vector directions and slip plane normals, $(\boldsymbol{s}_\alpha, \boldsymbol{m}_\alpha)$, defined in the intermediate configuration, with $\alpha = 1, ..., n$. The accumulated slips $\boldsymbol{\epsilon}$ are related to the actual slip $\boldsymbol{\gamma}$ by the relation

$$\dot{\epsilon}_\alpha = |\dot{\gamma}_\alpha| \quad \text{for } \alpha = 1, \dots, n, \tag{2.5}$$

in a component-wise manner. To describe the thermodynamic state of the material, we postulate a Helmholtz free energy density

$$W(\boldsymbol{F}, \boldsymbol{F}_\mathrm{p}, \boldsymbol{\epsilon}) = W_\mathrm{e}(\boldsymbol{F}_\mathrm{e}) + W_\mathrm{p}(\boldsymbol{\epsilon}) = W_\mathrm{e}(\boldsymbol{F}\boldsymbol{F}_\mathrm{p}^{-1}) + W_\mathrm{p}(\boldsymbol{\epsilon}), \tag{2.6}$$

where we adopt the decomposition introduced in (2.3). In this formulation, the total energy density is decomposed into an elastic part W_e, depending only on the elastic distortion $\boldsymbol{F}_\mathrm{e}$, and plastic stored energy W_p, representing the hardening response due to slip. The plastic stored energy is further decomposed into a self-hardening energy $W_\mathrm{p,self}$ and the associated latent hardening $W_\mathrm{p,lat}$

$$W_\mathrm{p}(\boldsymbol{\epsilon}) = W_\mathrm{p,self}(\boldsymbol{\epsilon}) + W_\mathrm{p,lat}(\boldsymbol{\epsilon}). \tag{2.7}$$

The specific choice of $W_\mathrm{p,self}(\boldsymbol{\epsilon})$ and $W_\mathrm{p,lat}(\boldsymbol{\epsilon})$ related to Mg will be discussed in Section 3.3.

In this energy representation, we choose the accumulated slips $\boldsymbol{\epsilon}$ over the actual slip $\boldsymbol{\gamma}$ as the start of our discussion because of the history-dependent hardening response, which implies W_p should be a direct function of $\boldsymbol{\epsilon}$ rather than the actual slip. Thus the state of the material is described by the variables $\{\boldsymbol{F}, \boldsymbol{F}_\mathrm{p}, \boldsymbol{\epsilon}\}$. At this point, we account for the plastic deformation, $\boldsymbol{F}_\mathrm{p}$, as one of the internal variables since it enters into the free energy explicitly for computing the elastic deformation. However, as we will see later, the structure of $\boldsymbol{F}_\mathrm{p}$ is generally considered to be related

to $\boldsymbol{\epsilon}$ by employing a flow rule, which leaves $\boldsymbol{\epsilon}$ as the only independent internal variables.

We denote the first Piola-Kirchhoff stress tensor by $\boldsymbol{P}$. If the material does not possess viscosity, $\boldsymbol{P}$ equals the equilibrium part of the stress, i.e.,

$$\boldsymbol{P} = \frac{\partial W}{\partial \boldsymbol{F}}(\boldsymbol{F}, \boldsymbol{F}_{\mathrm{p}}, \boldsymbol{\epsilon}) = \frac{\partial W_{\mathrm{e}}}{\partial \boldsymbol{F}}(\boldsymbol{F}\boldsymbol{F}_{\mathrm{p}}^{-1}). \tag{2.8}$$

Stress equilibrium requires that $\boldsymbol{P}$ satisfies the balance law,

$$\mathrm{Div}\, \boldsymbol{P} = \boldsymbol{0} \qquad \forall\, \boldsymbol{X} \in \Omega, \tag{2.9}$$

in the absence of body forces and inertial effects.

A flow rule is used to characterize the relation between the evolution of plastic deformation $\boldsymbol{F}_{\mathrm{p}}$ and the slip rate. The most general form of the flow rule is, see Ortiz and Stainier (1999),

$$\boldsymbol{l}_{\mathrm{p}} = \dot{\boldsymbol{F}}_{\mathrm{p}}\boldsymbol{F}_{\mathrm{p}}^{-1} = \dot{\boldsymbol{\epsilon}}\boldsymbol{M} = \sum_{\alpha=1}^{n} \dot{\epsilon}_{\alpha}\boldsymbol{M}_{\alpha}, \tag{2.10}$$

where $\boldsymbol{M} = \{\boldsymbol{M}_1, ..., \boldsymbol{M}_n\}$ is a collection of second-order tensors. A variation can be expressed as,

$$\mathrm{d}\boldsymbol{F}_{\mathrm{p}} = \sum_{\alpha=1}^{n} \mathrm{d}\epsilon_{\alpha}\,(\boldsymbol{M}_{\alpha}\boldsymbol{F}_{\mathrm{p}}) = \mathrm{d}\boldsymbol{\epsilon}(\boldsymbol{M}\boldsymbol{F}_{\mathrm{p}}). \tag{2.11}$$

We define the driving force $\boldsymbol{Y}$ acting on the internal varialbles $\boldsymbol{\epsilon}$ by,

$$\boldsymbol{Y} = -\frac{\partial W_{\mathrm{e}}}{\partial \boldsymbol{F}_{\mathrm{p}}} : \frac{\partial \boldsymbol{F}_{\mathrm{p}}}{\partial \boldsymbol{\epsilon}} - \frac{\partial W_{\mathrm{p}}}{\partial \boldsymbol{\epsilon}} = \boldsymbol{T} : (\boldsymbol{M}\boldsymbol{F}_{\mathrm{p}}) - \boldsymbol{\tau}_{\mathrm{p}}^{\mathrm{cr}}, \tag{2.12}$$

with $\boldsymbol{T}$ being the back stress, defined by

$$\boldsymbol{T} = -\frac{\partial W}{\partial \boldsymbol{F}_{\mathrm{p}}} = \boldsymbol{F}_{\mathrm{e}}^{\mathrm{T}}\boldsymbol{P}, \tag{2.13}$$

and $\boldsymbol{\tau}_{\mathrm{p}}^{\mathrm{cr}}$ being the current critical yield stress due to slip hardening,

$$\boldsymbol{\tau}_{\mathrm{p}}^{\mathrm{cr}} = \frac{\partial W_{\mathrm{p}}}{\partial \boldsymbol{\epsilon}}. \tag{2.14}$$

Here, we view $\boldsymbol{F}_\mathrm{p}$ as a function dependent on $\boldsymbol{\epsilon}$ via the flow rule (2.11). Further simplification gives

$$\boldsymbol{Y} = (\boldsymbol{F}_\mathrm{e}^\mathrm{T}\boldsymbol{P}\boldsymbol{F}_\mathrm{p}^\mathrm{T}) : \boldsymbol{M} - \boldsymbol{\tau}_\mathrm{p}^\mathrm{cr}. \tag{2.15}$$

Using index notation, the previous expression is

$$Y_\alpha = \boldsymbol{\sigma}_\mathrm{M} : \boldsymbol{M}_\alpha - \tau_{\mathrm{p},\alpha}^\mathrm{cr}, \qquad \alpha = 1, ..., n, \tag{2.16}$$

with Mandel stress tensor $\boldsymbol{\sigma}_\mathrm{M}$ defined by

$$\boldsymbol{\sigma}_\mathrm{M} = \boldsymbol{F}_\mathrm{e}^\mathrm{T}\boldsymbol{P}\boldsymbol{F}_\mathrm{p}^\mathrm{T}. \tag{2.17}$$

To derive the relations between the previously defined quantities that fulfill the second law of thermodynamics, following previous summary by Homayonifar and Mosler (2011), we consider the Clausius-Duhem dissipation inequality,

$$\mathcal{D} = \boldsymbol{P} : \dot{\boldsymbol{F}} - \dot{W} \geq 0, \tag{2.18}$$

where $\dot{W}$ is evaluated to

$$\dot{W} = \frac{\partial W_\mathrm{e}}{\partial \boldsymbol{F}} : \dot{\boldsymbol{F}} + \frac{\partial W_\mathrm{e}}{\partial \boldsymbol{F}_\mathrm{p}} : \dot{\boldsymbol{F}}_\mathrm{p} + \frac{\partial W_\mathrm{p}}{\partial \boldsymbol{\epsilon}} \cdot \dot{\boldsymbol{\epsilon}}. \tag{2.19}$$

In this equation, $\frac{\partial W_\mathrm{e}}{\partial \boldsymbol{F}_\mathrm{p}}$ is related to the back stress defined in (2.13). Inserting (2.13) into (2.19), the dissipation is reduced to

$$\mathcal{D} = \boldsymbol{\sigma}_\mathrm{M} : \boldsymbol{l}_\mathrm{p} - \boldsymbol{\tau}_\mathrm{p}^\mathrm{cr} \cdot \dot{\boldsymbol{\epsilon}}. \tag{2.20}$$

In this equation, $\boldsymbol{\sigma}_\mathrm{M}$ and $\boldsymbol{l}_\mathrm{p}$ are the previously defined Mandel stress and plastic velocity gradient in (2.17) and (2.4), respectively.

The set of admissible stress space is defined by an elastic domain,

$$\mathcal{S} = \{(\boldsymbol{\sigma}_\mathrm{M}, \boldsymbol{\tau}_\mathrm{p}^\mathrm{cr}) \in \mathbb{R}^{9+n} \ | \phi_\alpha(\boldsymbol{\sigma}_\mathrm{M}, \tau_{\mathrm{p},\alpha}^\mathrm{cr}) \leq 0, \alpha = 1, ..., n\}, \tag{2.21}$$

which is defined by n convex yield functions ϕ_α. Each of those is associated with a certain slip

system. For the choice of rate-independent plasticity, the yield function is

$$\phi_\alpha(\boldsymbol{\sigma}_\mathrm{M}, \tau^\mathrm{cr}_{\mathrm{p},\alpha}) = |\tau_\alpha| - \tau^\mathrm{cr}_{\mathrm{p},\alpha} - \tau^0_\alpha, \tag{2.22}$$

where τ_α is the so called resolved shear stress on slip system α, which is calculated by projecting the Mandel stress onto the slip plane by

$$\tau_\alpha = \boldsymbol{\sigma}_\mathrm{M} : (\boldsymbol{s}_\alpha \otimes \boldsymbol{m}_\alpha). \tag{2.23}$$

The yield criteria states that yielding occurs when the resolved shear stress on a particular system τ_α surpasses the hardening resistance $\tau_{\mathrm{p},\alpha}$ plus some initial yield stress τ^0_α. Thus additional shear must occur to make the stress state remain on the yield surface.

To apply the principle of maximum dissipation, we maximize the dissipation function (2.20) subject to the constraint (2.21). We define a set of Lagrange multipliers $\boldsymbol{\zeta} = [\zeta_1, ..., \zeta_n]$, each of which associates with one yield surface. Thus, we construct the Lagrangian of the system,

$$\mathcal{L}(\boldsymbol{\sigma}_\mathrm{M}, \boldsymbol{\tau}^\mathrm{cr}_\mathrm{p}, \boldsymbol{\zeta}) = \mathcal{D} - \sum_{\alpha=1}^{n} \zeta_\alpha \phi_\alpha. \tag{2.24}$$

Taking derivatives with respect to the stress-like variables $\boldsymbol{\sigma}_\mathrm{M}$ and $\boldsymbol{\tau}^\mathrm{cr}_\mathrm{p}$ yields

$$\boldsymbol{l}_\mathrm{p} = \sum_{\alpha=1}^{n} \zeta_\alpha \frac{\partial \phi_\alpha}{\partial \boldsymbol{\sigma}_\mathrm{M}} = \sum_{\alpha=1}^{n} \zeta_\alpha \,\mathrm{sgn}(\tau_\alpha) \boldsymbol{s}_\alpha \otimes \boldsymbol{m}_\alpha, \tag{2.25a}$$

$$\dot{\epsilon}_\alpha = \zeta_\alpha \frac{\partial \phi_\alpha}{\partial \tau^\mathrm{cr}_{\mathrm{p},\alpha}} = \zeta_\alpha, \tag{2.25b}$$

together with the Karush-Kuhn-Tucker (KKT) optimality conditions,

$$\zeta_\alpha \geq 0, \qquad \zeta_\alpha \phi_\alpha = 0, \tag{2.26}$$

where we deduce that the accumulated shear should be nondecreasing and that plasticity only evolves on the yield surface. From (2.5), the slip rates, $\dot{\boldsymbol{\gamma}}$, are related to $\dot{\boldsymbol{\epsilon}}$ via

$$\dot{\gamma}_\alpha = \dot{\epsilon}_\alpha \,\mathrm{sgn}(\tau_\alpha). \tag{2.27}$$

Thus we can simplify the optimality condition in (2.25a) to get the flow rule

$$\boldsymbol{l}_{\mathrm{p}} = \sum_{\alpha=1}^{N} \dot{\gamma}_\alpha \boldsymbol{s}_\alpha \otimes \boldsymbol{m}_\alpha, \tag{2.28}$$

which is a specific form of the general flow rule in (2.10) defining the relationship between slip $\boldsymbol{\gamma}$ and plastic strain $\boldsymbol{F}_{\mathrm{p}}$. Comparing with (2.10), we identify

$$\boldsymbol{M}_\alpha = \boldsymbol{s}_\alpha \otimes \boldsymbol{m}_\alpha \operatorname{sgn}(\tau_\alpha). \tag{2.29}$$

An application of the flow rule (2.28) yields the driving force $\boldsymbol{Y}$ on $\boldsymbol{\epsilon}$ via (2.15),

$$Y_\alpha = |\tau_\alpha| - \tau^{\mathrm{cr}}_{\mathrm{p},\alpha}. \tag{2.30}$$

By inserting (2.25) into the dissipation inequality (2.20), we arrive at the inequality,

$$\mathcal{D} = \sum_{\alpha=1}^{n} \dot{\epsilon}_\alpha \left(|\tau_\alpha| - \tau^{\mathrm{cr}}_{\mathrm{p},\alpha} \right) = \sum_{\alpha=1}^{n} \dot{\epsilon}_\alpha Y_\alpha \geq 0. \tag{2.31}$$

In addition, this inequality can also be expressed in terms of the actual slip field. Using the relation (2.27), we have

$$\mathcal{D} = \sum_{\alpha=1}^{n} \dot{\gamma}_\alpha \left[\tau_\alpha - \tau^{\mathrm{cr}}_{\mathrm{p},\alpha} \operatorname{sgn}(\tau_\alpha) \right] \geq 0. \tag{2.32}$$

2.3 A variational reformulation of crystal plasticity theory

In Section 2.2, the accumulated slips $\boldsymbol{\epsilon}$ are used as our primary internal variables because of the history-dependent material hardening response. However, as we have shown in the end of the last section, it might be more intuitive to use the actual slip $\boldsymbol{\gamma}$ to represent the internal process as it directly relates to the flow rule (2.28). In order to develop a more consistent and compatible argument with the rest of this thesis work, from now on we will switch to the slips $\boldsymbol{\gamma}$ as our primary internal variables. Similarly, the Helmholtz free energy is decomposed into

$$W = W_{\mathrm{e}}(\boldsymbol{F}_{\mathrm{e}}) + W_{\mathrm{p}}(\boldsymbol{\epsilon}(\boldsymbol{\gamma})) = W_{\mathrm{e}}(\boldsymbol{F}\boldsymbol{F}_{\mathrm{p}}^{-1}) + W_{\mathrm{p}}(\boldsymbol{\epsilon}(\boldsymbol{\gamma})). \tag{2.33}$$

Here we view the accumulated strain rate as a function dependent on slip via the relation $\dot{\epsilon} = |\dot{\boldsymbol{\gamma}}|$. We define the force vector $\boldsymbol{Y}$ as

$$Y_\alpha = \tau_\alpha - \tau^{\mathrm{cr}}_{\mathrm{p},\alpha} \operatorname{sgn}(\tau_\alpha). \tag{2.34}$$

By assuming the yielding function (2.22), the evolution of $\boldsymbol{\gamma}$ is determined by

- $\dot{\gamma}_\alpha = 0 \quad$ if $|Y_\alpha| < \tau^0_\alpha$,
- $\dot{\gamma}_\alpha \neq 0 \quad \Rightarrow |Y_\alpha| = \tau^0_\alpha$.

Thus $\boldsymbol{Y}$ indeed serves as the driving force for internal variables $\boldsymbol{\gamma}$. From (2.16), the driving force on system α is

$$Y_\alpha = \boldsymbol{\sigma}_{\mathrm{M}} : \boldsymbol{M}_\alpha - \frac{\partial W_{\mathrm{p}}}{\partial \epsilon_\alpha} \frac{\partial \epsilon_\alpha}{\partial \gamma_\alpha} = \boldsymbol{\sigma}_{\mathrm{M}} : \boldsymbol{M}_\alpha - \tau^{\mathrm{cr}}_{\mathrm{p},\alpha} \operatorname{sgn}(\tau_\alpha). \tag{2.35}$$

Comparing with (2.34) and using the definition of the resolved shear stress (2.23), we discover that

$$\boldsymbol{M}_\alpha = \boldsymbol{s}_\alpha \otimes \boldsymbol{m}_\alpha, \tag{2.36}$$

from which we recover the flow rule (2.28).

Following Ortiz and Stainier (1999), to determine the evolution of the internal variables, we assume that the rate of the local internal process described by $\dot{\boldsymbol{\gamma}}$ is determined solely by the current local thermodynamic state, which gives the general form of the kinetic equation,

$$\dot{\boldsymbol{\gamma}} = \boldsymbol{f}(\boldsymbol{F}, \boldsymbol{F}_{\mathrm{p}}, \boldsymbol{\gamma}). \tag{2.37}$$

The kinetic relation (2.37) and stress balance law (2.9) complete the set of equations to determine the thermodynamic state of the material.

The Onsager reciprocity relation (Onsager, 1931) states that the kinetic relation (2.37) can be derived from a dissipation potential $\Psi(\boldsymbol{Y})$ such that

$$\dot{\boldsymbol{\gamma}} = \frac{\partial \Psi}{\partial \boldsymbol{Y}}(\boldsymbol{Y}). \tag{2.38}$$

We postulate the dissipation potential corresponding to the yield function (2.21),

$$\Psi_\alpha(Y) = \begin{cases} 0 & \text{if} \quad |Y| \leq \tau_\alpha^0, \\ +\infty & \text{otherwise}, \end{cases} \tag{2.39}$$

meaning that the region outside the yield surface is not accessible. The total dissipation potential is the sum of all the individual potentials,

$$\Psi(\boldsymbol{Y}) = \sum_{\alpha=1}^{n} \Psi_\alpha(Y). \tag{2.40}$$

In addition, we introduce the dual kinetic potential $\Psi^*(\dot{\boldsymbol{\epsilon}})$ via Legendre transformation, i.e.,

$$\Psi^*(\dot{\boldsymbol{\gamma}}) = \sup_{\boldsymbol{Y}} \{\boldsymbol{Y} \cdot \dot{\boldsymbol{\gamma}} - \Psi(\boldsymbol{Y})\}, \tag{2.41}$$

where it follows that

$$\Psi^*(\dot{\boldsymbol{\gamma}}) = \sum_{\alpha=1}^{n} \Psi_\alpha^*(\dot{\gamma}) \quad \text{with} \quad \Psi_\alpha^*(\dot{\gamma}) = \tau_\alpha^0 |\dot{\gamma}|, \tag{2.42}$$

with the property that

$$\boldsymbol{Y} \in \frac{\partial \Psi^*}{\partial \dot{\boldsymbol{\gamma}}}(\dot{\boldsymbol{\gamma}}). \tag{2.43}$$

In this relation, the differential inclusion is used because the dissipation potential is a non-smooth function because it is derived for the case of rate-independent plasticity.

To develop a variational statement of the constitutive relations, we introduce the rate functional (Ortiz and Stainier, 1999),

$$\mathcal{E}(\dot{\boldsymbol{F}}, \dot{\boldsymbol{\gamma}}) = \dot{W}(\boldsymbol{F}, \boldsymbol{\gamma}) + \Psi^*(\dot{\boldsymbol{\gamma}}) = \frac{\partial W}{\partial \boldsymbol{F}} : \dot{\boldsymbol{F}} - \boldsymbol{Y} \cdot \dot{\boldsymbol{\gamma}} + \Psi^*(\dot{\boldsymbol{\gamma}}). \tag{2.44}$$

Optimizing (2.44) over the slip rate recovers the dual form of the kinetic relation (2.43), i.e.,

$$\boldsymbol{0} \in \frac{\partial \mathcal{E}}{\partial \dot{\boldsymbol{\gamma}}} = \frac{\partial \Psi^*}{\partial \dot{\boldsymbol{\gamma}}} - \boldsymbol{Y}, \tag{2.45}$$

which results in a condensed form,

$$\mathcal{E}_{\text{cond}} = \min_{\dot{\gamma}} \mathcal{E}(\dot{\boldsymbol{F}}, \dot{\gamma}). \tag{2.46}$$

And the first Piola-Kirchhoff stress tensor $\boldsymbol{P}$ can be calculated through

$$\boldsymbol{P} = \frac{\partial \mathcal{E}_{\text{cond}}}{\partial \dot{\boldsymbol{F}}} = \frac{\partial W}{\partial \boldsymbol{F}}. \tag{2.47}$$

In this formulation, by transforming the evolution law (2.38) into a dissipation potential, the rate of the total deformation $\dot{\boldsymbol{F}}$ and the evolution of slip field $\dot{\gamma}$ are both calculated through the minimization of the rate functional (2.44). The fully variational structure of this approach admits certain numerical advantages such as allowing larger time steps over the conventional explicit updates based on evolution equations as discussed in Section 1.2.

At last, we note that the yield function (2.22) and the dissipation potential we adopted in this chapter are for the choice of rate-independent plasticity, as we can see directly that the driving force in (2.34) is a constant function of slip rate. As we will see later in Section 3.3, for the modeling of general materials with rate-dependent behavior, a power law form of the dual dissipation potential in (3.35) is used and a rate dependency study of material behavior in terms of the stress-strain response will be shown in Chapter 7.

2.4 Extracting thermal effects from the variational formulation

During inelastic deformation, stored energy is released and dissipated; specifically, it is converted into heat as well as into plastic hardening energy stored in the material's microstructure. In Yang et al. (2006), a variational formulation of the thermo-mechanical coupling problem was proposed. Following the summary of Stainier and Ortiz (2010), the postulated free energy is dependent on the absolute temperature T in addition to the deformation gradient $\boldsymbol{F}$ and internal variables $\boldsymbol{\gamma}$, i.e.,

$$W = W(\boldsymbol{F}, \boldsymbol{\gamma}, T). \tag{2.48}$$

For metals, the free energy is usually assumed to be decomposed additively as

$$W = W_{\mathrm{e}}(\boldsymbol{F}_{\mathrm{e}}, T) + W_{\mathrm{p}}(\boldsymbol{\epsilon}(\boldsymbol{\gamma})) + W_H(T) = W_{\mathrm{e}}(\boldsymbol{F}\boldsymbol{F}_{\mathrm{p}}^{-1}, T) + W_{\mathrm{p}}(\boldsymbol{\epsilon}(\boldsymbol{\gamma})) + W_H(T), \tag{2.49}$$

where $W_H(T)$ is the heat storage capacity of the material.

Following Coleman and Noll (1963), the entropy density per unit undeformed volume is given by

$$\rho_0 \eta = -\frac{\partial W}{\partial T}(\boldsymbol{F}, \boldsymbol{\gamma}, T), \tag{2.50}$$

where η is the entropy per unit mass and ρ_0 is the mass density in the undeformed configuration, and the heat capacity follows as

$$\rho_0 C = -T\frac{\partial^2 W}{\partial T^2}(\boldsymbol{F}, \boldsymbol{\gamma}, T), \tag{2.51}$$

where C is the specific heat capacity. Finally, the law of energy conservation is expressed in the entropy form,

$$\rho_0 \dot{\eta} = \frac{1}{T}\left(\boldsymbol{Y} \cdot \dot{\boldsymbol{\gamma}} - \operatorname{Div} \boldsymbol{H} + \rho_0 Q\right), \tag{2.52}$$

where $\boldsymbol{H}$ is the heat flux and Q denotes an external heat source. We consider an adiabatic process, where the external heat source and the heat flux are neglected. Thus the conservation of energy is simplified to

$$\rho_0 \dot{\eta} = \frac{1}{T}\boldsymbol{Y} \cdot \dot{\boldsymbol{\gamma}}. \tag{2.53}$$

To derive the evolution law to describe the temperature evolution, we write out the time evolution of the entropy density in (2.50). Applying the chain rule, we have

$$\rho_0 \dot{\eta} = -\frac{\partial^2 W}{\partial T \partial \boldsymbol{F}} : \dot{\boldsymbol{F}} - \frac{\partial^2 W}{\partial T \partial \boldsymbol{\gamma}} \cdot \dot{\boldsymbol{\gamma}} - \frac{\partial^2 W}{\partial T^2}\dot{T} = -\frac{\partial \boldsymbol{P}}{\partial T} : \dot{\boldsymbol{F}} + \frac{\partial \boldsymbol{Y}}{\partial T} \cdot \dot{\boldsymbol{\gamma}} - \frac{\rho_0 C}{T}\dot{T}, \tag{2.54}$$

where the equation is simplified using (2.51), the first Piola-Kirchhoff stress tensor (2.8) and driving force $\boldsymbol{Y}$ associated to internal variable $\boldsymbol{\gamma}$, defined similarly as in (2.12). Inserting (2.54) into energy conservation law (2.53), we have,

$$\rho_0 C\dot{T} = T\frac{\partial \boldsymbol{P}}{\partial T} : \dot{\boldsymbol{F}} - T\frac{\partial \boldsymbol{Y}}{\partial T} \cdot \dot{\boldsymbol{\gamma}} + \boldsymbol{Y} \cdot \dot{\boldsymbol{\gamma}} \approx \boldsymbol{Y} \cdot \dot{\boldsymbol{\gamma}} = \mathcal{D}. \tag{2.55}$$

Here we neglect the contributions from the first two terms, which represent contributions from thermoelastic effects and intrinsic dissipation, since they are very small compared to the third term for metals undergoing large strain (Stainier and Ortiz, 2010). Applying (2.34) and (2.27), we arrive at the evolution law of temperature in crystals,

$$\rho_0 C\dot{T} = \sum_{\alpha=1}^{n} (\tau_\alpha \dot{\gamma}_\alpha - \tau_{\mathrm{p},\alpha}^{\mathrm{cr}} \dot{\epsilon}_\alpha) = \boldsymbol{\tau} \cdot \dot{\boldsymbol{\gamma}} - \boldsymbol{\tau}_{\mathrm{p}}^{\mathrm{cr}} \cdot \dot{\boldsymbol{\epsilon}}. \tag{2.56}$$

As a consequence of this variational approach, the Taylor-Quinney factor β (Taylor and Quinney, 1934), defined as the ratio of dissipated heat per plastic power, thus follows as

$$\beta = \frac{\boldsymbol{\tau} \cdot \dot{\boldsymbol{\gamma}} - \boldsymbol{\tau}_{\mathrm{p}}^{\mathrm{cr}} \cdot \dot{\boldsymbol{\epsilon}}}{\boldsymbol{\tau} \cdot \dot{\boldsymbol{\gamma}}}. \tag{2.57}$$

Unlike many other thermo-mechanical models, where the dissipated heat is calculated through a predefined Taylor-Quinney factor, in this variational formulation, the combination of free energy and dissipation potential is sufficient to determine every aspect of the material behavior and the dissipated heat follows directly from the conservation of energy, while the Taylor-Quinney factor is predicted as an a-posteriori value.

Chapter 3

Theoretical Framework for Slip-Twinning Interaction and Application to HCP Materials and Magnesium

In this chapter, we first outline the basic theory to describe the interactions of dislocation slip and twinning in general materials in which the two mechanisms are observed. Materials of this kind generally exhibit highly anisotropic behavior in the inelastic range and do not have enough slip systems to accommodate general deformations. Therefore, additional inelastic mechanisms such as twinning must occur. In the second part, this theory is applied to study magnesium by choosing appropriate energy functional representations and material parameters. The framework for this and the following chapters follows the discussion in our previously published paper (Chang and Kochmann, 2015).

The modeling approach is built upon the conventional crystal plasticity formulation for finite strains, cf. Rice (1971), Asaro and Rice (1977) and Asaro (1983), but incorporates the idea of twinning ratio (volume fraction) introduced in Section 1.3 to describe the microstructural evolution due to twinning at the lower scale. Thus, rather than resolving individual twins and dislocations, we resort to plastic slip and twinning ratios as the primary internal variables to describe the material's internal processes as done, for example, in Agnew et al. (2001), Staroselsky and Anand (2003), Graff et al. (2007), Zhang and Joshi (2012) and Homayonifar and Mosler (2011, 2012). The theoretical setup is based on an energetic approach, which can be cast into a variational formulation that

can be solved in a numerically efficient way. Let us first introduce the kinematic relations before presenting the variational approach based on concepts of Ortiz and Stainier (1999) and Ortiz et al. (2000).

3.1 Kinematic description of the slip–twinning competition

Suppose the material's crystallography exhibits n_s slip systems denoted by $(\boldsymbol{s}_\alpha, \boldsymbol{m}_\alpha)$, where $\boldsymbol{s}_\alpha$ and $\boldsymbol{m}_\alpha$ are unit vectors pointing into the direction of slip and being normal to the slip plane, respectively. Analogously, there exist n_t twin systems $(\boldsymbol{a}_\beta, \boldsymbol{n}_\beta)$ with twin plane normal $\boldsymbol{n}_\beta$ and twinning shear direction $\boldsymbol{a}_\beta$, see e.g., Christian and Mahajan (1995) for a review. Here and in the following, we use subscripts α and β to differentiate between slip and twin systems, respectively. As in conventional crystal plasticity models, dislocation activity is described by plastic slips $\boldsymbol{\gamma} = \{\gamma_1, \dots, \gamma_{n_s}\}$ acting across all n_s slip system. In addition, the effect of twinning is captured by the twinning ratios $\boldsymbol{\lambda} = \{\lambda_1, \dots, \lambda_{n_t}\}$ which describe the volume fractions of the twinned orientations. Obviously, the twin volume fractions are constrained by

$$0 \leq \lambda_\beta \leq 1 \quad \text{for} \quad \beta = 1, \dots, n_t, \qquad \text{and} \qquad 0 \leq \sum_{\beta=1}^{n_t} \lambda_\beta \leq 1. \tag{3.1}$$

Thus, the primary internal variables are the slip amounts $\boldsymbol{\gamma}$ and twinning ratios $\boldsymbol{\lambda}$. It is important to note that models based on this kinematic description do not qualify to describe the intricate details of individual twins that may arise on much smaller length scales than those of dislocations on the mesoscale of a polycrystal, cf. Yu et al. (2012). Unlike e.g., phase field models for deformation twinning (Clayton and Knap, 2011a, 2013) or explicit continuum models resolving individual twins (Kochmann and Le, 2009a), the introduction of twin volume fractions allows us to decouple the length scales and to model the effective material response on the mesoscopic level. We note that the description of the inelastic phenomena in terms of plastic slips and twin volume fractions is only one possible strategy to represent the microstructural configuration and thus to model plastic deformation; see e.g., the related approaches based on dislocation densities (Arsenlis and Parks, 2002; Bertin et al., 2013; Hansen et al., 2013; Lee et al., 2010; Ma and Roters, 2004).

In finite strains, we may assume a multiplicative decomposition of the deformation gradient tensor $\boldsymbol{F} = \operatorname{Grad} \boldsymbol{\varphi}$ (where $\boldsymbol{\varphi}(\boldsymbol{X})$ denotes the deformation mapping) into elastic and inelastic

parts, i.e.,

$$\boldsymbol{F} = \boldsymbol{F}_{\mathrm{e}}\,\boldsymbol{F}_{\mathrm{in}}, \tag{3.2}$$

where $\boldsymbol{F}_{\mathrm{e}}$ and $\boldsymbol{F}_{\mathrm{in}}$ denote the elastic and inelastic deformation gradients, respectively. Both slip and twinning contribute to the plastic deformation and the specific order of these two mechanisms is not obvious. Therefore, we adopt the approach of Kalidindi (2001) and work with a single inelastic deformation gradient $\boldsymbol{F}_{\mathrm{in}}$ to incorporate both relaxation schemes rather than further splitting $\boldsymbol{F}_{\mathrm{in}}$ multiplicatively into plastic slip and twinning components (Homayonifar and Mosler, 2011, 2012). This further implies that no kinematic interactions between slip an twinning are built into this decomposition but will be accounted for by the specific constitutive model presented below.

From (3.2) the velocity gradient tensor as well as its elastic and inelastic contributions follow as, respectively,

$$\boldsymbol{l} = \dot{\boldsymbol{F}}\boldsymbol{F}^{-1} = \boldsymbol{l}_{\mathrm{e}} + \boldsymbol{l}_{\mathrm{in}} = \boldsymbol{l}_{\mathrm{e}} + \boldsymbol{F}_{\mathrm{e}}\,\tilde{\boldsymbol{l}}_{\mathrm{in}}\,\boldsymbol{F}_{\mathrm{e}}^{-1} \qquad \text{with} \qquad \boldsymbol{l}_{\mathrm{e}} = \dot{\boldsymbol{F}}_{\mathrm{e}}\boldsymbol{F}_{\mathrm{e}}^{-1}, \quad \tilde{\boldsymbol{l}}_{\mathrm{in}} = \dot{\boldsymbol{F}}_{\mathrm{in}}\boldsymbol{F}_{\mathrm{in}}^{-1}. \tag{3.3}$$

Since at mesoscopic time scales slip and twinning are assumed to occur simultaneously, we further split the inelastic velocity gradient into its slip and twinning contributions according to

$$\tilde{\boldsymbol{l}}_{\mathrm{in}} = \tilde{\boldsymbol{l}}_{\mathrm{p}} + \tilde{\boldsymbol{l}}_{\mathrm{tw}}, \tag{3.4}$$

The kinematic interactions of slip and twinning are built into the flow rule as follows. Upon deformation twinning, all slip systems $(\boldsymbol{s}_\alpha, \boldsymbol{m}_\alpha)$ in the parent orientation are reflected across the twin interfaces onto the respective twin orientation. Hence, the re-oriented slip systems $(\boldsymbol{s}'_{\alpha\beta}, \boldsymbol{m}'_{\alpha\beta})$, i.e., the original slip system $(\boldsymbol{s}_\alpha, \boldsymbol{m}_\alpha)$ now re-oriented in twin orientation β, are given by

$$\boldsymbol{s}'_{\alpha\beta} = \boldsymbol{Q}_\beta \boldsymbol{s}_\alpha, \quad \boldsymbol{m}'_{\alpha\beta} = \boldsymbol{Q}_\beta \boldsymbol{m}_\alpha, \qquad \text{with} \quad \boldsymbol{Q}_\beta = \boldsymbol{I} - 2\,\boldsymbol{n}_\beta \otimes \boldsymbol{n}_\beta \tag{3.5}$$

(and no summation over repeated indices is implied here). Consequently, the flow rule for slip is modified from conventional crystal plasticity to account for dislocation activity on both the original slip systems and their twin-orientation counterparts. Extending concepts of Kalidindi

(2001) and Zhang and Joshi (2012), we thus use the following flow rules for slip and twinning:

$$\tilde{\boldsymbol{l}}_{\mathrm{p}} = \sum_{\alpha=1}^{n_s} \dot{\gamma}_\alpha \left[\phi \left(1 - \sum_{\beta=1}^{n_t} \lambda_\beta \right) \boldsymbol{s}_\alpha \otimes \boldsymbol{m}_\alpha + \sum_{\beta=1}^{n_t} \phi(\lambda_\beta)\, \boldsymbol{s}'_{\alpha\beta} \otimes \boldsymbol{m}'_{\alpha\beta} \right], \tag{3.6a}$$

$$\tilde{\boldsymbol{l}}_{\mathrm{tw}} = \sum_{\beta=1}^{n_t} \dot{\lambda}_\beta\, \gamma_\beta^{\mathrm{tw}}\, \boldsymbol{a}_\beta \otimes \boldsymbol{n}_\beta. \tag{3.6b}$$

Here, $\gamma_\beta^{\mathrm{tw}}$ is the maximum twinning shear strain associated with system β, which we assume to be constant and which is determined from the material's crystallography. $\phi(\lambda)$ is assumed to be a monotonically-increasing function that governs the switching between parent and twin orientations. For compatibility it must satisfy $\phi(0) = 0$ and $\phi(1) = 1$. Our numerical experiments have shown that the specific choice of $\phi(\lambda)$ has little impact on the microstructural evolution due to the specific mechanisms leading to slip and twinning. If a grain is oriented favorably for twinning, it will in most cases completely reorient from the untwinned into the twinned state before alternative relaxation mechanisms (usually basal plane slip systems) are activated. However, the specific choice of $\phi(\lambda)$ is only relevant as long as the twin volume fractions are evolving (in the purely untwinned or fully twinned states it is irrelevant). From our experience, there is no reason to define more complicated representations of $\phi(\lambda)$ than the simplest valid choice, which will be used in the following, viz. $\phi(\lambda) = \lambda$, and which reduces to the formulation of Zhang and Joshi (2012).

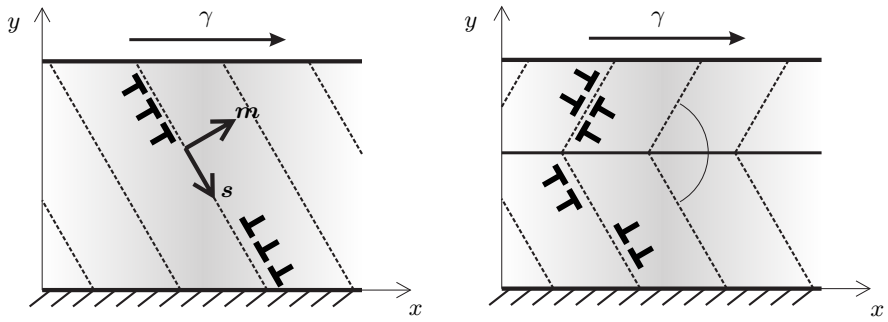

Figure 3.1: Schematic of one active slip system reorientation by the formatio of a twin.

In order to capture plastic hardening due to slip, we introduce the accumulated plastic strains $\boldsymbol{\epsilon} = (\epsilon_1, \ldots, \epsilon_{n_s})$, which are updated when slip occurs on any of the n_s slip systems (in parent and twin orientations) via

$$\dot{\epsilon}_\alpha = |\dot{\gamma}_\alpha| \quad \text{for } \alpha = 1, \ldots, n_s. \tag{3.7}$$

Altogether, these model assumptions imply that we account for slip in both untwinned and twinned orientations, and that dislocations are fully transferred between these two orientations. Also, both untwinned and twinned orientations contribute to plastic hardening. This is different than the recent model of Homayonifar and Mosler (2012), for example, who assumed all dislocations are consumed by the moving twinning front and no dislocations are transferred from the untwinned to the twinned orientation.

3.2 Constitutive relations and variational framework

Like in conventional crystal plasticity the Helmholtz free energy density is assumed to decompose additively as

$$\begin{aligned} W(\boldsymbol{F}, \boldsymbol{F}_{\text{in}}, \boldsymbol{\epsilon}, \boldsymbol{\lambda}) &= W_{\text{e}}(\boldsymbol{F}_{\text{e}}) + W_{\text{p}}(\boldsymbol{\epsilon}) + W_{\text{tw}}(\boldsymbol{\lambda}) \\ &= W_{\text{e}}(\boldsymbol{F}_{\text{e}}) + W_{\text{p,self}}(\boldsymbol{\epsilon}) + W_{\text{p,lat}}(\boldsymbol{\epsilon}) + W_{\text{tw,self}}(\boldsymbol{\lambda}) + W_{\text{tw,lat}}(\boldsymbol{\lambda}), \end{aligned} \tag{3.8}$$

where W_{e} is the elastic strain energy density depending on $\boldsymbol{F}_{\text{e}} = \boldsymbol{F}\boldsymbol{F}_{\text{in}}^{-1}$. W_{p} denotes the stored plastic energy density due to slip, which further decomposes into self-hardening and latent hardening contributions, $W_{\text{p,self}}$ and $W_{\text{p,lat}}$, respectively. Analogously, W_{tw} denotes the stored plastic energy density due to twinning, which contains self-hardening and latent hardening contributions, $W_{\text{tw,self}}$ and $W_{\text{tw,lat}}$, respectively. Specific choices of all energy densities for magnesium will be discussed in Section 3.3.

We cast the material model into a variational framework (Ortiz and Stainier, 1999), so that the evolution of the internal variables is governed by the principle of minimum dissipation potential, see e.g., Carstensen et al. (2002) and Conti and Ortiz (2008) for discussions and Hackl and Fischer (2008) for its relation to the principal of maximum dissipation. We introduce the dual (dissipation) potential $\Psi^*(\dot{\boldsymbol{\gamma}}, \dot{\boldsymbol{\lambda}})$ so that the internal variables follow from the principle of minimum dissipation potential (i.e., they minimize the total stress power):

$$0 \in \frac{\partial}{\partial \dot{\gamma}_\alpha}(\dot{W} + \Psi^*), \qquad 0 \in \frac{\partial}{\partial \dot{\lambda}_\beta}(\dot{W} + \Psi^*). \tag{3.9}$$

The differential inclusions are necessary when rate-independence is considered; in the case of rate-dependent evolution laws, the differential inclusions may be replaced by equalities, see e.g., Carstensen

et al. (2002) and Kochmann and Hackl (2011). The dual potential is assumed to have contributions from slip and twinning in an additive fashion, generally

$$\Psi^*_{\mathrm{p}}(\dot{\boldsymbol{\epsilon}}) = \sum_{\alpha=1}^{n_s} \Psi^*_{\mathrm{p},\alpha}(\dot{\epsilon}_\alpha), \qquad \Psi^*_{\mathrm{tw}}(\dot{\boldsymbol{\lambda}}) = \sum_{\beta=1}^{n_t} \Psi^*_{\mathrm{tw},\beta}(\dot{\lambda}_\beta). \tag{3.10}$$

To arrive at the resulting evolution laws, let us expand the stress power as

$$\dot{W} + \Psi^* = \frac{\partial W_{\mathrm{e}}}{\partial \boldsymbol{F}_{\mathrm{e}}} \cdot \dot{\boldsymbol{F}}_{\mathrm{e}} + \frac{\partial W_{\mathrm{p}}}{\partial \boldsymbol{\epsilon}} \cdot \dot{\boldsymbol{\epsilon}} + \frac{\partial W_{\mathrm{tw}}}{\partial \boldsymbol{\lambda}} \cdot \dot{\boldsymbol{\lambda}} + \Psi^*_{\mathrm{p}}(\dot{\boldsymbol{\epsilon}}) + \Psi^*_{\mathrm{tw}}(\dot{\boldsymbol{\lambda}}). \tag{3.11}$$

From (3.3) and (3.6) it follows that

$$\dot{\boldsymbol{F}}_{\mathrm{e}} = \dot{\boldsymbol{F}}\boldsymbol{F}_{\mathrm{in}}^{-1} - \boldsymbol{F}_{\mathrm{e}}\dot{\boldsymbol{F}}_{\mathrm{in}}\boldsymbol{F}_{\mathrm{in}}^{-1} = \dot{\boldsymbol{F}}\boldsymbol{F}_{\mathrm{in}}^{-1} - \boldsymbol{F}_{\mathrm{e}} \left(\sum_\alpha \dot{\gamma}_\alpha \boldsymbol{p}_\alpha + \sum_\beta \dot{\lambda}_\beta \, \gamma_\beta^{\mathrm{tw}} \, \boldsymbol{a}_\beta \otimes \boldsymbol{n}_\beta \right), \tag{3.12}$$

where $\boldsymbol{p}_\alpha$ is an abbreviation for the average slip direction tensor for each slip system over all twinned orientations:

$$\boldsymbol{p}_\alpha = \phi \left(1 - \sum_\beta \lambda_\beta \right) \boldsymbol{s}_\alpha \otimes \boldsymbol{m}_\alpha + \sum_\beta \phi(\lambda_\beta) \, \boldsymbol{s}'_{\alpha\beta} \otimes \boldsymbol{m}'_{\alpha\beta}. \tag{3.13}$$

Furthermore, note that

$$\frac{\partial W_{\mathrm{e}}}{\partial \boldsymbol{F}_{\mathrm{e}}} = \frac{\partial W_{\mathrm{e}}}{\partial \boldsymbol{F}} \cdot \frac{\partial \boldsymbol{F}}{\partial \boldsymbol{F}_{\mathrm{e}}} = \boldsymbol{P}\boldsymbol{F}_{\mathrm{in}}^{\mathrm{T}}, \qquad \text{where} \qquad \boldsymbol{P} = \frac{\partial W}{\partial \boldsymbol{F}} = \frac{\partial W_{\mathrm{e}}}{\partial \boldsymbol{F}} \tag{3.14}$$

denotes the first Piola-Kirchhoff stress tensor. Overall, this leads to

$$\dot{W} + \Psi^* = \boldsymbol{P} \cdot \dot{\boldsymbol{F}} - \sum_{\alpha=1}^{n_s} \dot{\gamma}_\alpha \tau_\alpha^{\mathrm{p}} - \sum_{\beta=1}^{n_t} \dot{\lambda}_\beta \tau_\beta^{\mathrm{tw}} + \frac{\partial W_{\mathrm{p}}}{\partial \boldsymbol{\epsilon}} \cdot \dot{\boldsymbol{\epsilon}} + \frac{\partial W_{\mathrm{tw}}}{\partial \boldsymbol{\lambda}} \cdot \dot{\boldsymbol{\lambda}} + \Psi^*_{\mathrm{p}}(\dot{\boldsymbol{\epsilon}}) + \Psi^*_{\mathrm{tw}}(\dot{\boldsymbol{\lambda}}), \tag{3.15}$$

with the resolved shear stresses on the slip and twin systems, respectively,

$$\tau_\alpha^{\mathrm{p}} = \boldsymbol{\sigma}_M \cdot \boldsymbol{p}_\alpha \qquad \text{and} \qquad \tau_\beta^{\mathrm{tw}} = \gamma_\beta^{\mathrm{tw}} \, \boldsymbol{\sigma}_M \cdot (\boldsymbol{a}_\beta \otimes \boldsymbol{n}_\beta) \tag{3.16}$$

and the Mandel stress tensor

$$\boldsymbol{\sigma}_{\mathrm{M}} = \boldsymbol{F}_{\mathrm{e}}^{\mathrm{T}} \boldsymbol{P} \boldsymbol{F}_{\mathrm{in}}^{\mathrm{T}}. \tag{3.17}$$

Finally, application of principle (3.9) yields the evolution laws for the internal variables:

$$0 \in -|\tau_\alpha^{\mathrm{p}}| + \frac{\partial W_{\mathrm{p}}}{\partial \epsilon_\alpha} + \frac{\partial \Psi^*_{\mathrm{p},\alpha}}{\partial \dot{\epsilon}_\alpha}, \tag{3.18a}$$

$$0 \in -\tau_\beta^{\mathrm{tw}} + \frac{\partial W_{\mathrm{tw}}}{\partial \lambda_\beta} + \frac{\partial \Psi^*_{\mathrm{tw},\beta}}{\partial \dot{\lambda}_\beta}. \tag{3.18b}$$

The missing norm in the evolution law for the twinning volume fractions is only valid as long as $\lambda_\beta = 0$, to implement the polarity of twinning. That is, in contrast to slip, which may occur in either positive or negative direction, twinning is restricted to occur in only one direction per twin system for crystallographic reasons, see e.g., Christian and Mahajan (1995). This, of course, changes as soon as $\lambda_\beta > 0$, so that a reversal of the loading can lead to detwinning (which implies $\dot{\lambda}_\beta < 0$), see e.g., Lou et al. (2007). Also, we have neglected the dependence of the average slip direction tensor $\boldsymbol{p}_\alpha$ on the rates of the twinning ratios $\dot{\lambda}_\beta$, which is a valid assumption when considering small incremental steps in our numerical setup.

Experiments have found evidence for higher-order twin patterns, i.e., the activity of a second twin system in already-twinned domains of the crystal, see e.g., Hong et al. (2010) and Kadiri et al. (2013). However, how such competing twin systems develop (e.g., in which order they are activated and whether or not they evolve simultaneously) is not entirely clear. Our model assumes that at a given instance of time only one twin system is evolving at any material point. This does not rule out that the crystal twins on one system and, as soon as the reorientation is complete, another twin system can be activated to result in the coexistence of multiple twin variants in the final deformed state.

To model twinning within an already twinned domain on a second system, we need to consider the reorientation of already twinned crystal by the newly-activated twin system. Since there is no limitation to the number of activatable twin systems, this could lead to a highly recursive mechanism, and the resulting cross-interactions between the twin and slip systems soon become numerically demanding, if not intractable, especially within an implicit, variational framework. Therefore, we neglect the possibility of multiple twin variants evolving at the same time at any given material point for the sake of a fully implicit, variational formulation that covers many other phenomena observed experimentally, as shown later. Of course, this is a simplification of physical reality. In Taylor-type polycrystal simulations, this implies that only one twin variant is evolving at a time within each grain. In contrast, for mesoscale finite-element simulations that resolve the

grain structure geometrically, the assumption demands that only one twin system is active at a time at each material point, thus allowing for (spatially-separated) multiple twin variants within a grain. While the restriction to only one active system is not a stringent necessity of the variational approach, it greatly reduces the model complexity, thus allowing for more efficient simulations. Many of the previously proposed models, see e.g., Homayonifar and Mosler (2011, 2012) and Zhang and Joshi (2012), use similar flow rules and reorientation schemes as presented here.

3.3 Specific choices of energetics and kinematics for pure magnesium

3.3.1 Elastic energy: polyconvex strain energy density

Here and in the following, we use conventional Miller indices to describe planes and orientations in the hexagonal lattice structure whose coordinate system is defined by the three basal unit vectors $\{\boldsymbol{a}_1, \boldsymbol{a}_2, \boldsymbol{a}_3\}$ with $\boldsymbol{a}_3 = -(\boldsymbol{a}_1 + \boldsymbol{a}_2)$ and the longitudinal axis with unit vector $\boldsymbol{c} = \{0, 0, 0, 1\}$. Due to its hcp crystallography, the elastic response of Mg exhibits transverse isotropy (with isotropy in the basal plane). Almost all previous models for Mg used isotropic strain energy densities to approximate the elastic response, a common albeit simplifying approximation, see e.g., the discussion in Clayton and Knap (2011a). Here, in addition to capturing the anisotropic elastic behavior of hcp metals, we aim to construct a polyconvex energy density for the following reasons. At finite strains, the loss of quasiconvexity of the free energy density can lead to the loss of stability of a homogeneous deformation gradient and to the formation of fine-scale microstructure (so-called minimizing sequences), see e.g., Ball (1976), Ball and James (1987), Ortiz and Repetto (1999), Mielke (2004) and Conti and Theil (2005). Quasiconvexity is hard to enforce owing to its non-local definition. A reasonable alternative is the use of polyconvex energy densities since polyconvexity (of a finite-valued, continuous function) implies quasiconvexity which, in turn, ensures rank-one convexity, thus avoiding instability due to loss of ellipticity under large deformation. Here, we adopt the polyconvex energy density proposed by Schröder et al. (2008) and adjust it to describe the transversely-isotropic response of magnesium.

We assume the additive decomposition of the strain energy density into isotropic and anisotropic

parts and we adopt the material frame-indifferent form

$$W_{\mathrm{e}}(\boldsymbol{F}) = W_{\mathrm{iso}}(I_1, I_2, I_3) + W_{\mathrm{aniso}}(J_4, J_5) \tag{3.19}$$

with invariants of the right Cauchy-Green tensor $\boldsymbol{C} = \boldsymbol{F}^{\mathrm{T}}\boldsymbol{F}$ defined by

$$\begin{aligned} I_1 &= \operatorname{tr}\boldsymbol{C}, \\ I_2 &= \operatorname{tr}(\operatorname{Cof}\boldsymbol{C}), \\ I_3 &= \det\boldsymbol{C}, \\ J_4 &= \operatorname{tr}(\boldsymbol{C}\boldsymbol{G}), \\ J_5 &= \operatorname{tr}\left[(\operatorname{Cof}\boldsymbol{C})\boldsymbol{G}\right] \end{aligned}$$

and the cofactor operator defined via $\operatorname{Cof}\boldsymbol{A} = (\det\boldsymbol{A})\boldsymbol{A}^{-\mathrm{T}}$. Metric tensor $\boldsymbol{G}$ depends on the specific material symmetry, which in case of hcp materials is given by

$$\boldsymbol{G} = \operatorname{diag}(1, 1, C^2) \qquad \Rightarrow \qquad \operatorname{Cof}\boldsymbol{G} = \operatorname{diag}(C^2, C^2, C^4). \tag{3.20}$$

For magnesium we have $C = c/a = 1.624$, where a and c denote the length of the basal-plane's Burgers vector in the $\langle 11\bar{2}0\rangle$ direction and the hcp unit cell height, respectively. Following Schröder et al. (2008), our specific choices of the isotropic and anisotropic energy densities are

$$W_{\mathrm{iso}}(I_1, I_2, I_3) = \alpha_1\, I_1 + \alpha_2\, I_2 + \delta_1\, I_3 - \delta_2\, \log\sqrt{I_3}, \tag{3.21}$$

$$W_{\mathrm{aniso}}(J_4, J_5) = \frac{\eta_1}{\alpha_4\, g^{\alpha_4}}\left(J_4^{\alpha_4}, +J_5^{\alpha_4}\right), \tag{3.22}$$

for which the constraints of ellipticity and a stress-free reference configuration impose the restrictions

$$\alpha_1 > 0, \qquad \alpha_2 > 0, \qquad \delta_1 > 0, \qquad \eta_1 > 0, \qquad \alpha_4 > 1, \qquad \delta_2 = 2\alpha_1 + 4\alpha_2 + 2\delta_1 + 2\eta_1. \tag{3.23}$$

To fit these unknown elastic material parameters to experimental data, we compute the components of the elastic modulus tensor

$$\mathbb{C}_{IJKL}(\boldsymbol{F}) = 8\,\frac{\partial W_{\mathrm{e}}}{\partial C_{IJ}\,\partial C_{KL}}(\boldsymbol{F}), \tag{3.24}$$

	C_{11}	C_{33}	C_{44}	C_{13}	C_{12}	C_{66}
experimental:	59.74	62.00	16.59	21.48	25.65	17.05
model:	59.72	57.26	17.27	21.93	25.81	16.95

Table 3.1: Experimentally-determined transversely-isotropic elastic constants of pure Mg at 280 K (all values in GPa), from Slutsky and Garland (1957) as well as the corresponding elastic constants of the polyconvex energy density.

which yields the following elastic moduli in the undeformed ground state:

$$\begin{aligned}\mathbb{C}_{IJKL}(\boldsymbol{I}) &= 4(\alpha_2+\delta_1+\alpha_4\eta_1)\delta_{IJ}\delta_{KL} + 2\,(\alpha_1+\alpha_2)\,(\delta_{IK}\delta_{JL}+\delta_{IL}\delta_{JK}) \\ &\quad + 2\frac{\eta_1}{g}\left[G_{JK}\delta_{LI}+G_{JL}\delta_{IK}+G_{IL}\delta_{JK}+G_{IK}\delta_{LJ}-2\alpha_4(\delta_{IJ}G_{KL}+G_{IJ}\delta_{KL})\right] \\ &\quad + 8(\alpha_4-1)\frac{\eta_1}{g^2}\,G_{IJ}\,G_{KL}\end{aligned}$$

with $g = \operatorname{tr}\boldsymbol{G} = 2 + C^2$. Notice that in the isotropic case ($\boldsymbol{G} = \boldsymbol{I}$), we recover the isotropic form with Lamé moduli

$$\lambda = 4(\alpha_2+\delta_1+\alpha_4\eta_1), \qquad \mu = 2(\alpha_1+\alpha_2). \tag{3.25}$$

Using the specific form (3.20) for hcp crystals, the components of the elasticity tensor become (in Voigt notation)

$$C_{11} = \mathbb{C}_{1111} = 4\left[\alpha_1+2\alpha_2+\delta_1+\alpha_4\eta_1-\frac{2a^2(a^2+c^2)(\alpha_4-1)\eta_1}{(2a^2+c^2)^2}\right], \tag{3.26}$$

$$C_{33} = \mathbb{C}_{3333} = 4\left[\alpha_1+2\alpha_2+\delta_1+\alpha_4\eta_1-\frac{4a^2c^2(\alpha_4-1)\eta_1}{(2a^2+c^2)^2}\right], \tag{3.27}$$

$$C_{44} = \mathbb{C}_{2323} = 2\left[\alpha_1+\alpha_2+\eta_1-\frac{a^2\eta_1}{2a^2+c^2}\right], \tag{3.28}$$

$$C_{13} = \mathbb{C}_{1133} = 4\left[\alpha_2+\delta_1+\frac{a^2\eta_1\left(2\alpha_4a^2+(3\alpha_4-2)c^2\right)}{(2a^2+c^2)^2}\right], \tag{3.29}$$

$$C_{12} = \mathbb{C}_{1122} = 4\left[\alpha_2+\delta_1+\frac{\eta_1\left(2a^4(\alpha_4-1)+\alpha_4(2a^2+c^2)c^2\right)}{(2a^2+c^2)^2}\right], \tag{3.30}$$

$$C_{66} = \mathbb{C}_{1212} = 2\left[\alpha_1+\alpha_2+\frac{2a^2\eta_1}{2a^2+c^2}\right]. \tag{3.31}$$

To confirm transverse isotropy, we note that the chosen form of the energy density satisfies auto-

matically

$$C_{66} = \frac{C_{11} - C_{12}}{2}. \tag{3.32}$$

The elastic moduli have been fit to those determined experimentally by Slutsky and Garland (1957), shown in Table 3.1, which results in the material parameters for the polyconvex strain energy density summarized in Table 3.2. In addition, the corresponding surface of directional Young moduli is illustrated in Figure 3.2. Table 3.1 also contains the experimental data for comparison. With the exception of C_{33}, the anisotropic elastic moduli are well captured by the chosen strain energy density, which is deemed sufficient for subsequent simulations.

α_1	α_2	δ_1	δ_2	α_4	η_1
4.82	3.46	0.06	23.76	10.0	0.45

Table 3.2: Best-fit results for the parameters used in the polyconvex strain energy density (all values in GPa except dimensionless α_4).

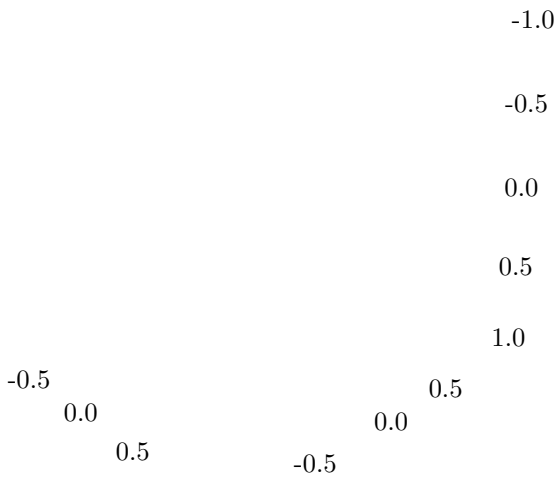

Figure 3.2: Elastic surface of the directional Young moduli for pure magnesium as obtained from the polyconvex energy density (qualitative graphic only rescaled to maximum).

It should be noted that the elastic modulus depends on the lattice structures, and thus should be reoriented in the twinned orientation. This could be addressed by the reorientation of the resulting stress tensor and stiffness matrix if the material is considered fully twinned. In the subsequent

calculations, we do not account for this reorientation as the elastic anisotropy of Mg is very small ($C_{11} \approx C_{33}, C_{12} \approx C_{13}$ and $C_{44} \approx (C_{11} - C_{12})/2$), and the elastic behavior is often approximated as an isotropic response (Clayton and Knap, 2011a; Staroselsky and Anand, 2003; Zhang and Joshi, 2012).

3.3.2 Inelastic deformation mechanism in pure magnesium

From all possible slip systems, basal slip is the dominant mode in Mg due to the significantly lower critical resolved shear stresses on basal slip systems with slip directions $\{11\bar{2}0\}$ and slip plane normal $\{0001\}$. In addition, prismatic and pyramidal $\langle a \rangle$ slip systems are frequently observed when the activation of basal slip is suppressed (Burke and Hibbard, 1952; Reed-Hill and Robertson, 1958). Since the slip directions of these three systems all lie within the basal plane, they can operate on only four independent shear systems, which is insufficient to accommodate arbitrary plastic straining (Taylor, 1938; von Mises, 1928). Therefore, pyramidal $\langle c + a \rangle$ slip has been identified as a further slip mode active in Mg, see e.g., Obara et al. (1973) and Ando and Tonda (2000), in particular to accommodate compression along the c-axis. The various types of slip systems are illustrated in Figure 1.2 and summarized in Table 1.1.

Some of the previous models for Mg have incorporated only a subset of the aforementioned slip systems due to redundancy and in order to reduce computational complexity and costs. In particular, the inclusion of pyramidal $\langle c+a \rangle$ slip was shown to beneficially reproduce experimental results, see e.g., Agnew et al. (2001). On the other hand, prismatic and pyramidal $\langle a \rangle$ slips show quite similar effects to the prismatic ones (Agnew et al., 2006; Chapuis and Driver, 2011) but at considerably higher resolved shear stresses. Therefore, we choose to not include the pyramidal $\langle a \rangle$ systems. Overall, our set of modeled slip systems is thus given by the basal, prismatic, and pyramidal $\langle c + a \rangle$ systems, which already provided realistic results for alloy AZ31B (Agnew and Duygulu, 2005; Agnew et al., 2003).

Deformation twinning is the most common mechanism in Mg to allow plastic deformation along the c-axis (requiring considerably lower activation stresses than the aforementioned non-basal slip systems). The most frequently observed twinning mode in Mg is the $\{10\bar{2}1\}\langle\bar{1}011\rangle$ tensile twin system, which is activated when the c-axis is in tension. The critical shear strain associated with this twinning mode for pure Mg is $\gamma_{\text{tw}} = 0.1295$ (Christian and Mahajan, 1995). Furthermore, compression twinning can be observed when the c-axis is in compression (Barnett, 2007; Kelley

and Hosford, 1968a). However, as pointed out, e.g., by Zhang and Joshi (2012), and as seen in experiments (Brown et al., 2005), this twinning mode is difficult to activate due to its much higher critical resolved shear stress and large critical shear strain. Tensile twins are considerably easier to nucleate and their mobility is significantly higher, too, which can be explained by the differences in the twinning dislocation core structures of tensile and compressive twinning (Christian and Mahajan, 1995). The relevant twin systems to be included in our model are included in Table 1.1 along with their critical shear strains. As an important difference between slip and twinning, dislocations are free to glide in either positive or negative direction, whereas twinning is only allowed to occur in the twinning direction. This fact is automatically accounted for in the model presented here due to the twinning description via volume fractions. We will discuss the relevance of the tension and compression twin systems later in our numerical examples.

3.3.3 Stored energy: choice of hardening energies and dissipation potentials

The mechanical resistance differs dramatically between the various slip and twin systems, which leads to the observed highly-anisotropic plastic response. These differences are captured in the model by the hardening energies and associated dissipation potentials for all slip and twin systems. Plastic work is stored in self-energy of each slip system and in interaction energy. For the self-energy, we assume the general representation

$$W_{\mathrm{p,self}}(\boldsymbol{\epsilon}) = \sum_{\alpha} \sigma_{\alpha}^{\infty} \left[\epsilon_{\alpha} + \frac{\sigma_{\alpha}^{\infty}}{h_{\alpha}} \exp\left(-\frac{h_{\alpha}\, \epsilon_{\alpha}}{\sigma_{\alpha}^{\infty}} \right) \right], \tag{3.33}$$

whose parameters differ between systems. The exponential law mimics Voce hardening (Agnew et al., 2001; Graff et al., 2007) and is well suited to describe the high-resistance of non-basal slip systems in hcp metals (Homayonifar and Mosler, 2011). σ_{α}^{∞} is the ultimate stress on each system, and h_{α} captures the corresponding hardening rate. In practice, small σ_{α}^{∞} and large h_{α} will result in a low activation. The slip hardening response is completed by assuming linear latent hardening for reasons discussed in Homayonifar and Mosler (2011, 2012), which implies

$$W_{\mathrm{p,lat}}(\boldsymbol{\epsilon}) = \frac{1}{2} \boldsymbol{\epsilon} \cdot \mathcal{H} \boldsymbol{\epsilon}, \tag{3.34}$$

where $\mathcal{H}$ is a symmetric matrix containing the hardening moduli on its off-diagonals (and having a zero diagonal).

The rate dependence of all slip systems is accounted for by a power-law dissipation potential commonly used in crystal plasticity, see e.g., Ortiz and Stainier (1999),

$$\Psi_{\mathrm{p}}^{*}(\dot{\boldsymbol{\gamma}}) = \sum_{\alpha} \frac{\tau_0 \dot{\gamma}_0}{m+1} \left(\frac{\dot{\gamma}_\alpha}{\dot{\gamma}_0} \right)^{m+1}. \tag{3.35}$$

with material constants τ_0, $\dot{\gamma}_0$ and m (one set of these for each slip system).

The tensile twin system is activated when the c-axis is in tension. Zhang and Joshi (2012) assumed a hard threshold for its activation. Beyond this yield point, they assumed that the resolved shear stress stress remains constant, which essentially implies a linear growth of the stored energy without hardening. Here, we take a different standpoint and assume linear hardening and linear rate dependence, i.e., we choose quadratic forms for both the hardening energy. For comparison, the similar formulation of Homayonifar and Mosler (2011) used a linear twin hardening energy. The associated dissipation potential must describe the rate-dependence of twinning. The recent work of Ulacia et al. (2010) shows a very low sensitivity of twinning in Mg alloys, and even negative strain rate sensitivity has been reported (Chun and Davies, 2011); see also the discussion in Li and Ma (2009) about twinning in Mg as a dissipative vs. elastic reshuffling process. To account for the low rate sensitivity, we here set the dissipation potential associated with twinning to zero. In summary, this results in

$$W_{\mathrm{tw}}(\boldsymbol{\lambda}) = \sum_{\beta} \frac{1}{2} h_\beta \lambda_\beta^2 + \frac{1}{2} \boldsymbol{\lambda} \cdot \mathcal{K} \boldsymbol{\lambda}, \tag{3.36a}$$

$$\Psi_{\mathrm{tw}}^{*}(\dot{\boldsymbol{\lambda}}) = 0, \tag{3.36b}$$

where h_β is the hardening parameter of twin system β, and $\mathcal{K}$ denotes the matrix containing all cross-hardening moduli.

To illustrate the different hardening laws and associated stress-strain responses, we perform a simple-shear test with only a single active system by aligning the slip or twinning direction with the macroscopic shear direction. The resulting stress-strain curves are shown in Figure 3.3. Obviously, basal slip and tensile twinning are easiest to activate, whereas prismatic and pyramidal slip require higher stress levels. Note that (in the absence of slip) the twinning curve becomes elastic once

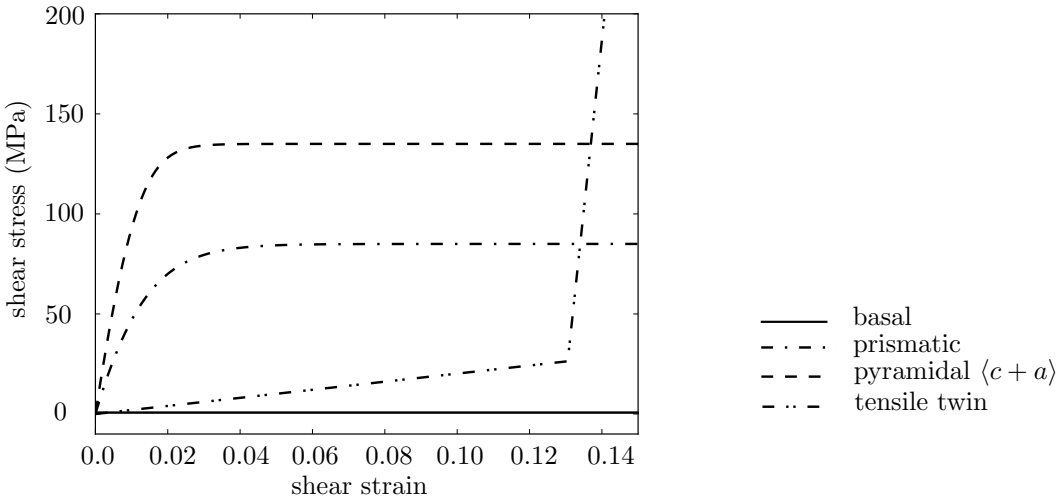

Figure 3.3: Hardening response of the different hardening energies

the twin volume fraction has reached 1 and the crystal is fully twinned. The material parameters used for these simulations have been determined by fitting experiments, which will be discussed in Section 5.3.

Chapter 4

Numerical Realization

The model is implemented via two numerical schemes: explicit updates and variational constitutive updates (implicit). Explicit updates compute the new the internal variables according to the evolution law in each time step after the global solver reaches convergence. This approach is widely used to solve initial value problems because of its simple formulation and easy implementation. However, it suffers from the same problem as most explicit solvers in that it requires a large number of short time steps, which results in high computational cost. In contrast, variational updates (Ortiz et al., 2000; Ortiz and Stainier, 1999) equilibrate the balance law and evolution equations simultaneously, which produces the exact solution to the discretized PDEs. Thus, fewer and longer time steps can be used compared to the conventional explicit approaches.

In the rest of the chapter, we explain these two different approaches in great detail for discretizing the previously discussed model and making it amenable for numerical implementations. A performance comparison of these two schemes will be shown in Chapter 5.

4.1 Variational constitutive updates

Variational constitutive updates discretize the dissipation potential in (3.9) with constant time steps Δt by defining an incremental energy density (Ortiz et al., 2000; Ortiz and Stainier, 1999),

$$\begin{aligned}\mathcal{F}(\boldsymbol{F}^{n+1},\boldsymbol{\gamma}^{n+1},\boldsymbol{\lambda}^{n+1};\boldsymbol{F}_{\text{in}}^{n},\boldsymbol{\epsilon}^{n},\boldsymbol{\lambda}^{n}) = W(\boldsymbol{F}^{n+1},\boldsymbol{F}_{\text{in}}^{n+1},\boldsymbol{\epsilon}^{n+1},\boldsymbol{\lambda}^{n+1}) - W(\boldsymbol{F}^{n},\boldsymbol{F}_{\text{in}}^{n},\boldsymbol{\epsilon}^{n},\boldsymbol{\lambda}^{n}) \\ + \Delta t\,\Psi_{\text{p}}^{*}\left(\frac{|\gamma^{n+1}-\gamma^{n}|}{\Delta t}\right) + \Delta t\,\Psi_{\text{tw}}^{*}\left(\frac{|\boldsymbol{\lambda}^{n+1}-\boldsymbol{\lambda}^{n}|}{\Delta t}\right),\end{aligned} \tag{4.1}$$

where superscript $(\cdot)^n$ denotes a quantity evaluated at time t^n, and $t^{n+1} = t^n + \Delta t$. The discretization of the flow rule follows a forward-Euler scheme and approximates $\boldsymbol{F}_{\text{in}}^{n+1}$ by

$$\boldsymbol{F}_{\text{in}}^{n+1} = \text{dev}\left(\sum_{\alpha} \Delta\gamma_\alpha \, \boldsymbol{p}_\alpha^n + \sum_{\beta} \Delta\lambda_\beta \, \gamma_\beta^{\text{tw}} \, \boldsymbol{a}_\beta \otimes \boldsymbol{n}_\beta + \boldsymbol{I}\right) \boldsymbol{F}_{\text{in}}^n, \tag{4.2}$$

where we take the deviatoric part of the flow rule increment to ensure isochoric inelastic deformation. Also, $\Delta\gamma_\alpha = \gamma_\alpha^{n+1} - \gamma_\alpha^n$ and $\Delta\lambda_\beta = \lambda_\beta^{n+1} - \lambda_\beta^n$ are the increments in the slip and twinning ratio respectively, for the corresponding systems. Thus, given $\boldsymbol{\epsilon}^n, \boldsymbol{\lambda}^n$ and $\boldsymbol{F}_{\text{in}}^n$ at the old time t^n and the new deformation gradient $\boldsymbol{F}^{n+1}$, the new internal variables at time t^{n+1} are obtained by minimization of (4.1), i.e.,

$$(\boldsymbol{\gamma}^{n+1}, \boldsymbol{\lambda}^{n+1}) = \arg\min \, \mathcal{F}(\boldsymbol{F}^{n+1}, \boldsymbol{\gamma}^{n+1}, \boldsymbol{\lambda}^{n+1}; \boldsymbol{F}_{\text{in}}^n, \boldsymbol{\epsilon}^n, \boldsymbol{\lambda}^n), \tag{4.3}$$

which is the time-discrete version of the flow rules in (3.9). This results in the condensed strain energy density,

$$W_{\text{cond}}(\boldsymbol{F}^{n+1}; \boldsymbol{F}_{\text{in}}^n, \boldsymbol{\epsilon}^n, \boldsymbol{\lambda}^n) = \inf_{\Delta\boldsymbol{\gamma}, \Delta\boldsymbol{\lambda}} \left\{ \mathcal{F}(\boldsymbol{F}^{n+1}, \Delta\boldsymbol{\gamma}, \Delta\boldsymbol{\lambda}; \boldsymbol{F}_{\text{in}}^n, \boldsymbol{\epsilon}^n, \boldsymbol{\lambda}^n) \;:\; 0 \leq \boldsymbol{\lambda}^n + \Delta\boldsymbol{\lambda} \leq 1 \right\}, \tag{4.4}$$

and the corresponding first Piola-Kirchhoff stress tensor,

$$\boldsymbol{P}^{n+1} = \frac{\partial W_{\text{cond}}}{\partial \boldsymbol{F}^{n+1}}(\boldsymbol{F}^{n+1}; \boldsymbol{F}_{\text{in}}^n, \boldsymbol{\epsilon}^n, \boldsymbol{\lambda}^n). \tag{4.5}$$

In this algorithm, all states are evaluated at time step t^{n+1}, which therefore follows an implicit framework. The scheme is implemented in a predictor-corrector fashion and the minimization problem is solved by a projected-line search algorithm, which is summarized in Algorithm 4.1.

Algorithm 4.1 updates the internal states with fixed deformation $\boldsymbol{F}^{n+1}$, which is fed through either Taylor model type material point calculations or finite element interpolations on the global level. In typical material point calculations, one or several components of $\boldsymbol{F}$ are prescribed, and the unknowns are solved via minimizing the free energy or the incremental potential. This global iteration is summarized in Algorithm 4.2. The finite element calculation follows in a similar fashion, but instead the deformation gradient is interpolated from the nodal displacements. In both cases,

Algorithm 4.1:

Given $\boldsymbol{F}^n, \boldsymbol{F}^n_{\text{in}}, \boldsymbol{\epsilon}^n$ and $\boldsymbol{\lambda}^n$ from the previous time step and $\boldsymbol{F}^{n+1}$ from current step:

a) calculate the reoriented slip systems based on the twinnning ratio $\boldsymbol{\lambda}^n$;

b) use initial guesses $\boldsymbol{\gamma}^{n+1} = \boldsymbol{\gamma}^n, \boldsymbol{\lambda}^{n+1} = \boldsymbol{\lambda}^n$ and $\boldsymbol{F}^{n+1}_{\text{in}} = \boldsymbol{F}^n_{\text{in}}$;

c) calculate τ^{p}_α and τ^{tw}_β defined in equation (3.16) via the Mandel stress tensor in equation (3.17);

d) calculate the resolved shear stress from slip and twin hardening energies:

$$\tau^{\text{cr}}_\alpha = \frac{\partial W_{\text{p}}}{\partial \epsilon^n_\alpha}, \qquad \tau^{\text{cr}}_\beta = \frac{\partial W_{\text{tw}}}{\partial \lambda^n_\beta}, \qquad \forall \alpha, \beta;$$

e) let $\Delta\tau_{\max} = \max\{|\tau^{\text{p}}_\alpha| - \tau^{\text{cr}}_\alpha, \tau^{\text{tw}}_\beta - \tau^{\text{cr}}_\beta\}$ for all slip/twin systems. If $\Delta\tau_{\max} \leq 0$, then return without updating the internal states; else do the following iterations until $\Delta\tau_{\max}$ is smaller than the desired tolerance:

- insert the most active slip/twin system corresponding to $\Delta\tau_{\max}$ into active set $\mathcal{S}_{\text{act}}$;
- equilibrate the evolution equation (3.18) with

$$|\tau^{\text{p}}_\alpha| = \frac{\partial W_{\text{p}}}{\partial \epsilon^{n+1}_\alpha} + \frac{\partial \Psi^*_{\text{p},\alpha}}{\partial \dot{\epsilon}_\alpha}, \qquad \tau^{\text{tw}}_\beta = \frac{\partial W_{\text{tw}}}{\partial \lambda^{n+1}_\beta} + \frac{\partial \Psi^*_{\text{tw},\beta}}{\partial \dot{\lambda}_\beta}, \qquad \forall \alpha, \beta \in \mathcal{S}_{\text{act}},$$

  by updating the internal states $\boldsymbol{\gamma}^{n+1}$ and $\boldsymbol{\lambda}^{n+1}$, where $\dot{\epsilon}_\alpha$ and $\dot{\lambda}_\beta$ are approximated by

$$\dot{\epsilon}_\alpha = \frac{\epsilon^{n+1}_\alpha - \epsilon^n_\alpha}{\Delta t}, \qquad \dot{\lambda}_\alpha = \frac{\lambda^{n+1}_\beta - \lambda^n_\beta}{\Delta t};$$

- if the twinning ratio on the active twinning system $\lambda^{n+1}_\beta > 1$, then set $\lambda^{n+1}_\beta = 1$, the remaining iterations only update the slips $\boldsymbol{\gamma}$;
- update the resolved shear stress from (3.18), and the critical resolved shear stresses on all systems by

$$\tau^{\text{cr}}_\alpha = \frac{\partial W_{\text{p}}}{\partial \epsilon^{n+1}_\alpha} + \frac{\partial \Psi^*_{\text{p},\alpha}}{\partial \dot{\epsilon}_\alpha}, \qquad \tau^{\text{cr}}_\beta = \frac{\partial W_{\text{tw}}}{\partial \lambda^{n+1}_\beta} + \frac{\partial \Psi^*_{\text{tw},\beta}}{\partial \dot{\lambda}_\beta}, \qquad \forall \alpha, \beta;$$

- update $\Delta\tau_{\max} = \max\{|\tau^{\text{p}}_\alpha| - \tau^{\text{cr}}_\alpha, \tau^{\text{tw}}_\beta - \tau^{\text{cr}}_\beta\}$ for all slip/twin systems.

Algorithm 4.1: Variational updates of the internal states.

Algorithm 4.2:

for each time step, given the deformation gradient $\boldsymbol{F}^n$ from the previous time step:

a) make the initial guess $\boldsymbol{F}^{n+1} = \boldsymbol{F}^n$ and modify the constrained components of $\boldsymbol{F}^{n+1}$ to satisfy the boundary conditions;

b) calculate the stress residue tensor $\boldsymbol{r} = \frac{\partial W}{\partial \boldsymbol{F}} - \boldsymbol{P}_0$, where $\boldsymbol{P}_0$ is the non-zeros force applied. We iterate the following steps until the residue norm $\|\boldsymbol{r}\|$ is smaller than prescribed tolerance:

- update $\boldsymbol{F}^{n+1} = \boldsymbol{F}^{n+1} + \mathrm{d}\boldsymbol{F}$, where $\mathrm{d}\boldsymbol{F}$ is determined by the typical line-search method, e.g, by the Newton-Raphson update

$$\mathrm{d}\boldsymbol{F} = -\left(\frac{\partial^2 W}{\partial \boldsymbol{F}\partial \boldsymbol{F}}\right)^{-1} \frac{\partial W}{\partial \boldsymbol{F}};$$

- update internal states with the current $\boldsymbol{F}^{n+1}$ according to Algorithm 4.1;
- update the residue vector $\boldsymbol{r}$.

c) set the current internal variable state to the new state from the last iteration and go to the next time step.

Algorithm 4.2: Variational updates of the global deformation gradient.

iteration stops when the system equilibrium condition is satisfied.

4.2 Explicit updates

The explicit approach updates the internal states by inverting the evolution equations (3.18). Following the slip dissipation potential defined in (3.35), we arrive at the corresponding slip update rule:

$$\gamma_\alpha^{n+1} = \dot{\gamma}_0 \Delta t \left(\frac{|\tau_\alpha^{\mathrm{p}}| - \tau_\alpha^{\mathrm{cr}}}{\tau_0}\right)^{\frac{1}{m}} + \gamma_\alpha^n, \qquad \tau_\alpha^{\mathrm{cr}} = \frac{\partial W_{\mathrm{p}}}{\partial \epsilon_\alpha^n}, \tag{4.6}$$

where $\tau_\alpha^{\mathrm{cr}}$ is the critical resolved shear stress on slip system α based on slips from the old time step. A quick note about the above explicit rule: for most common crystals, the choice of the rate sensitivity parameter m is less than 0.1, which makes the exponent a large number ($1/m > 10$). Thus, the increase in deformation should be sufficiently small enough that the resulting increment in resolved shear stress is smaller than τ_0, otherwise the updated slip might become extremely large because of the large exponent. On the twinning side, since explicit updates cannot handle the case

Algorithm 4.3:

for each time step, given the deformation gradient $\boldsymbol{F}^n$ from the previous time step:

a) make the initial guess $\boldsymbol{F}^{n+1} = \boldsymbol{F}^n$ and modify the constrained components of $\boldsymbol{F}^{n+1}$ to satisfy the boundary condition;

b) equilibrate the balance law to get the new deformation gradient $\boldsymbol{F}^{n+1}$;

c) update internal variables according to (4.6) and (4.8). If the twinning ratio is greater than 1, the remainder of the calculation only considers slips;

d) go to the next time step.

Algorithm 4.3: Explicit updates algorithm.

of zero dissipation, we assume the dissipation to be of Newtonian viscous type, i.e.,

$$\Psi^*_{\text{tw}}(\dot{\boldsymbol{\lambda}}) = \sum_{\beta} \frac{1}{2}\mu\dot{\lambda}^2_{\beta}. \tag{4.7}$$

By inverting the evolution equation, the update rule for twinning ratio follows as

$$\lambda^{n+1}_{\beta} = \Delta t \frac{\tau^{\text{tw}}_{\beta} - \tau^{\text{cr}}_{\beta}}{\mu} + \lambda^n_{\alpha}, \qquad \tau^{\text{cr}}_{\beta} = \frac{\partial W_{\text{tw}}}{\partial \lambda^n_{\beta}}. \tag{4.8}$$

Slips and twinning are updated after the global solver has converged, which could be either a Taylor type material point calculation or a finite element simulation as previously discussed. This algorithm is summarized in Algorithm 4.3. As we discussed earlier, in this algorithm, the deformation and internal states together do not give an exact solution to the energy minimization problem in (4.1). Thus, in order to ensure numerical stability and ensure that the solution is close to the true solution, the time step used needs to be much smaller than in the variational approach. This study will be shown in the next chapter.

Chapter 5

Model Validation via Magnesium Single Crystal Simulation

The previously discussed variational model as well as the explicit numerical scheme are implemented in a generic C++ object oriented numerical framework, which is able to perform both Taylor type simulations and finite element calculations. In this section, we investigate a series of numerical experiments on single crystals to validate our model. In Section 5.1, we compare the twinning side of our model with the phase field approach (Clayton and Knap, 2011a,b) using nano-indentation tests on calcite and sapphire, whose deformation are usually dominated by twinning. In Section 5.2, we perform simple shear and compression tests on Mg signle-crystals with a single isolated slip/twin system to show the reorientation mechanisms as discussed in Chapter 3. The rest of the chapter is dedicated to studying and validating our model by comparing with experimental data on Mg single crystals. At last, a performance study between variational approach and explicit updates is shown in Section 5.4.

5.1 Comparison with the phase field approach

The phase field approach has been popular for studying the mechanics and physics of materials with different phases. The recent study by Clayton and Knap (2011a) reported a phase field theory to understand twin nucleation and twin interface propagation, which has been applied to study calcite and sapphire in a nanoindentation test (Clayton and Knap, 2011b). In the experiment, calcite and sapphire were oriented such that the direction of twinning shear was parallel to the loading

direction. Under such conditions, experimental evidence (Kosevich and Boĭko, 1971) shows that twinning appears at the left side of the indenter and forms a sharp tip (Figure 5.1). The length of the tip increases as the indentation depth increases. Twinning under such conditions was often reported as elastic, i.e., twins disappeared fully or partially upon load removal. The reason for the asymmetry lies in the fact that twinning is restricted to only occur in one direction (twinning is a unipolar mechanism).

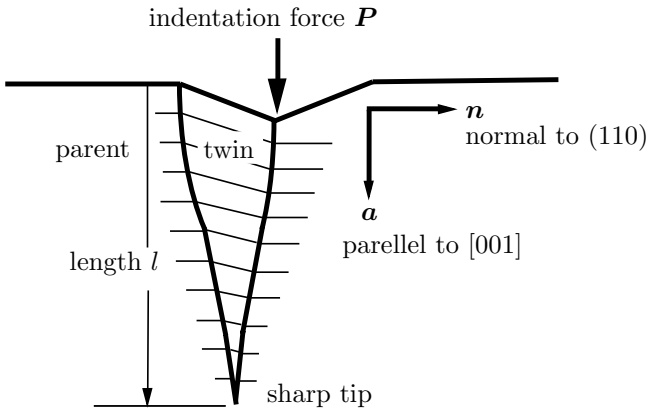

Figure 5.1: Experimental results for calcite in a nanoindentation experiment show that twinning appears on the left side of the indenter (picture taken from Clayton and Knap (2011b)).

In the phase field approach (Clayton and Knap, 2011a), an order parameter taking values between 0 and 1 is used to identify the material's orientation: 0 for parent and 1 for twin, and the twin interface is denoted by a value between 0 and 1 exclusively. In this approach, we solve for the order parameter field by minimizing the total free energy defined in (1.4) without the input of slip systems. In Figure 5.2, we summarize two results from Clayton and Knap (2011b). In the figure, the twin distributions are plotted via order parameter η for calcite e^+ twins (left) and sapphire Rhombohedral (R) twins (right). In both tests, sharp indentors of 90° wedge geometry were used and the indentation depths are the same for both cases. Calcite and sapphire are characterized by different critical twinning shears γ_{tw} (0.694 for calcite e^+ twin, and 0.202 for sapphire R twin). In both figures, sharp twins form on the left side of the wedge, where the driving stress for twinning is positive in sign, and therefore consistent with experimental observations. In addition, for the same indentation depth, the sapphire R twin is significantly longer than the corresponding calcite e^+ twin, which is because the critical twinning shear for calcite is larger than that for the sapphire

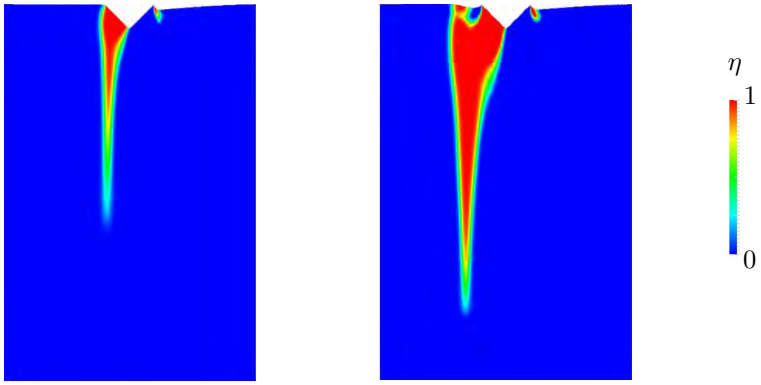

Figure 5.2: Phase field modeling of calcite e^+ twin (left) and sapphire R twin (right) with different critical twinning shear for a nanoindentation test (Clayton and Knap, 2011b).

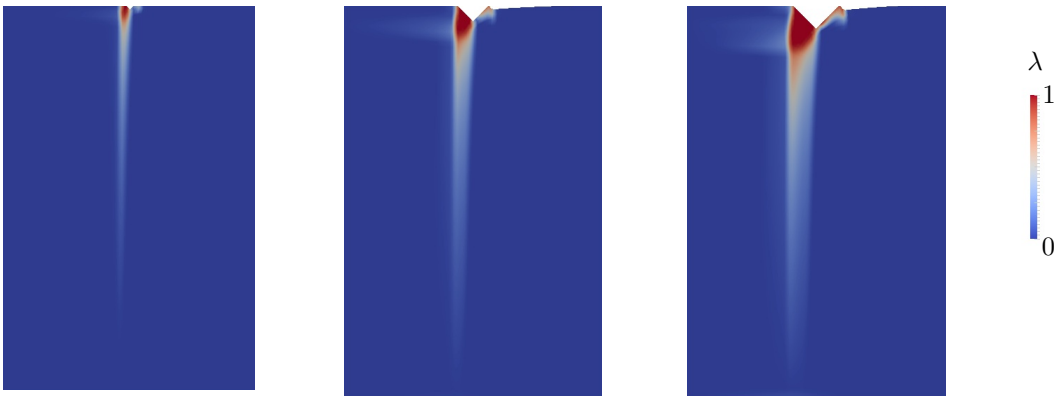

Figure 5.3: Twin evolution in terms of the twinning ratio of calcite e^+ twin for a nanoindentation test predicted by our crystal plasticity theory.

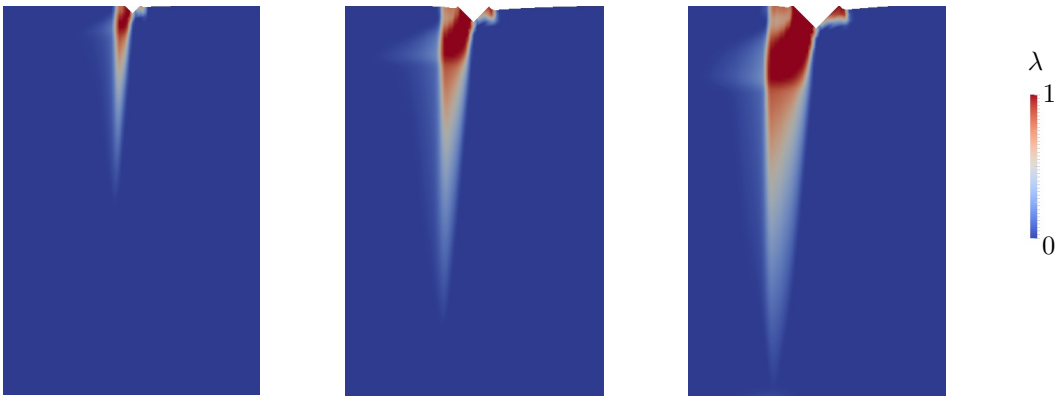

Figure 5.4: Twin evolution in terms of the twinning ratio of sapphire R twin for a nanoindentation test predicted by our crystal plasticity theory.

twin (0.635 versus 0.202), so that larger/longer twins are required to achieve comparable relaxation in elastic energy for smaller stress-free shear γ_{tw}.

For comparison, we apply the crystal plasticity model and computational techniques summarized in Chapter 3 and 4 to simulate this experiment, and the results are summarized in Figure 5.3 and Figure 5.4. As in the phase field simulation, the nanoindentation tests were performed on calcite and sapphire with one twin system placed parallel to the loading direction. In these simulations, all the slip systems are suppressed and not taken into account. In the figures, the evolution of the twinning ratio at different indentation depth is plotted. As a result, we see qualitatively quite similar shapes of twins formed at the left side of the indenter and the twin expands as the indenter goes deeper. Similar to the phase filed simulation, we see a bigger twin forming in sapphire because of the smaller critical twinning strain for the same reason discussed before. Thus, both phase field approach and the crystal plasticity model give reasonable predictions for both the twin shape and the qualitative characteristics occuring in the two materials.

Although we see quite similar material responses between the two models, there are inherent discrepancies which can be explained by the difference between the fundamental model ideas: in the crystal plasticity model, we assume material forming infinitely fine twins at each material point and our goal is to capture the effective twinning response from a higher scale. In addition, the crystal plasticity-based model is defined locally at each material point and does not involve length scales. Thus, only qualitative comparisons with experimental observations are made. In contrast, in the phase field model, individual twins and the twinning interface are explicitly modeled by the introduction of the interface energy, which prevents large regions of intermediate twinning ratios. Instead, the model prefers completely twinned and untwinned regions, which results in thin twin interfaces. In constrast, the crystal plasticity model does not penalize intermediate values of the twin ratios. We note that the scale of the phase field model is usually on the same scale as where twinning happens, thus it is very difficult to model large systems because of the fine resolution required near the twin interface. However, the concept of the twinning ratio is introduced naturally to handle this scale separation problem, thus making it amenable to study problems such as slip-twinning interactions.

5.2 Slip-twinning interations for a single slip/twin system

The model introduced in Chapter 3 involves complex interactions between slip and twinning in the sense that the crystal lattice is reflected across the twinning plane in the twinned orientation. In this section, we use simple examples to show the material response because of this direct influence by the choice of different slip/twin systems and loading conditions. In the following study, we consider a material with one slip system and one twin system whose critical shear strain is $\gamma_{\text{tw}} = 0.1$. We orient the slip and twin system differently and perform simple shear or compression tests. As a result, we look at both stress-strain responses and the slip activities. The hardening response with the slip is taken from the exponential energy used for prismatic slip system, where the ultimate shear stress is 85MPa, as shown in Figure 3.3 and parameters are summarized in Table 5.1. On the twinning side, we take a linear energy, i.e, $W_{\text{tw}} = \tau_{\text{cr}}^{\text{tw}}\lambda$ with $\tau_{\text{ct}}^{\text{tw}} = 20\text{MPa}$, which gives a constant critical resolved shear stress (CRSS) $\tau_{\text{cr}}^{\text{tw}}$ for twinning. The specific choice of this parameter follows from the experimental observation in Mg that twinning typically has a lower level of the activation stresses.

Figures 5.5 and 5.6 show two material point simulations we have performed. In Figure 5.5, simple shear deformation is applied to a single crystal with the same slip and twinning directions aligned with the applied shear. In this test, we see a three-stage deformation behavior: in the early stage, the critical shear stress is below 20MPa, and thus only the slip system is activated. Because of the slip hardening, the resolved shear stress increases as we deform the sample. When reaching 20MPa, the twin system is activated, which completes around a strain of 10%. During the activation of twinning, the stress level remains constant because of the non-hardening energy we assumed. Upon the completion of twinning, where the twinning ratio reaches 1.0, we see that the stress increases because of the reactivation of slip and eventually reaches the ultimate stress of 85MPa. In the same plot, we also record the amount of slip during the experiment, which reconfirms our analysis: below 10% of the applied strain, only a small amount of slip is observed since the deformation is dominated by twinning; once twinning completes, slip is active again to accommodate further deformation.

In the simple shear test example, the slip and twin systems coincide, and thus the interaction between slip and twinning is only coming from the different CRSS of different systems rather than lattice reorientation. In Figure 5.6, the single crystal is deformed under a plane-strain compression

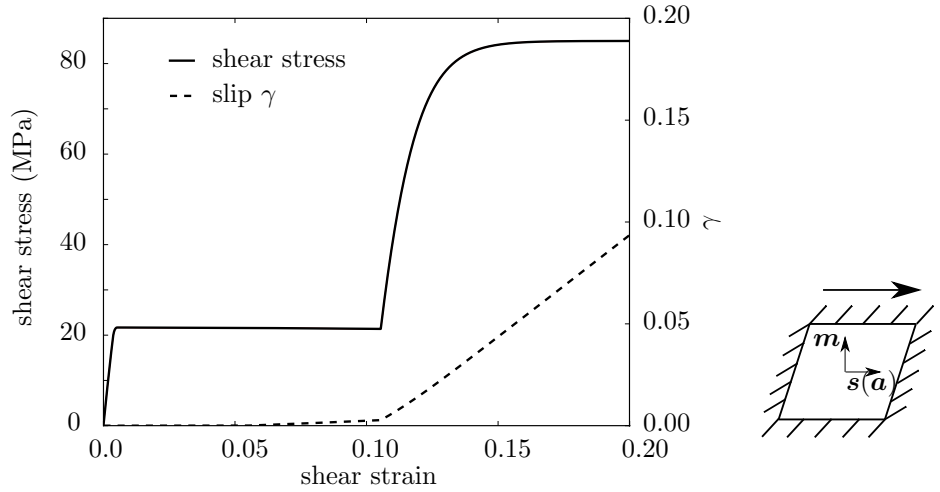

Figure 5.5: Stress-strain response of a simple toy material with single slip/twin systems under simple shear shows a three-stage response because of the low activation stress of twinning.

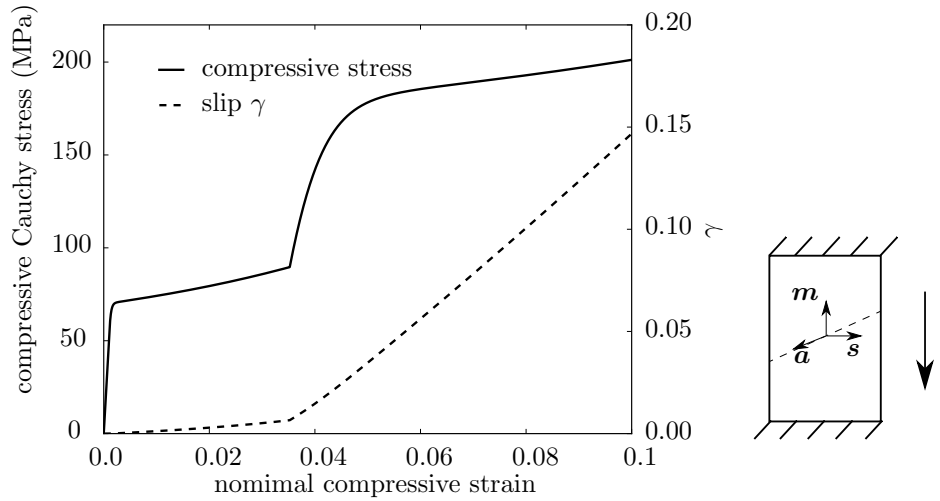

Figure 5.6: Stress-strain response of a simple toy material with single slip/twin systems under compression shows activation of slip after material lattice reorientation due to the completion of twinning.

test, where the slip and twin systems are oriented differently: the slip direction is perpendicular to the compressing direction and is thus impossible to activate alone; the twinning shear direction is 22.5° from the compression plane, which makes it the only active system in the early stage of compression. In the figure, we see a similar three-stage deformation as in the previous simple shear test: in the early stage of deformation when the resolved stress on the twinning system is lower than the CRSS of twinning, we see a purely elastic deformation since none of the two systems is active, and thus no plastic deformation occurs to accommodate the deformation. In the second stage, where the stress is large enough to trigger twinning, we see a plateau in the stress-strain curve because it is relaxed by twinning; upon the the completion of twinning, the slip system is reoriented to 45° to the compression direction, so that we see a typical slip hardening response and an increase of slip after about 3% of compression strain.

Our simulation with single slip/twin system shows a very well defined three-stage twin-slip deformation sequence, where one system is activated in each stage. However, these are overly simplified examples. As we discussed earlier in Chapter 3, the twin hardening energy follows a quadratic form and thus does not exhibite a constant CRSS. The deformation mechanism usually involves complex competition between twinning and slips. In the next few examples, Mg single crystals with full slip/twin systems are studied to validate our model.

5.3 Parameter identification and model validation

The numerical model summarized in previous sections contains a large number of material parameters that require identification; in particular the 12 slip and 6 twin systems require individual parameters to be determined before running complex polycrystalline simulations. Kelley and Hosford (1968a) performed a series of elaborate plane-strain compression tests on pure single-crystalline Mg at room temperature, whose results will be used to determine the model parameters for each system. By carefully orienting the loading with respect to the hcp lattice, different slip and twin systems were activated in each case. Here, we numerically reproduce six loading scenarios from their experiments to calibrate the parameters of the independent slip and twin systems, as shown in Figure 5.7, where black and white arrows indicate the loading and constraint directions respectively. All simulations are performed as material-point calculations under quasistatic conditions.

The imposed deformation corresponds to a velocity gradient

$$\boldsymbol{l} = \begin{bmatrix} l_{11} & l_{12} & l_{13} \\ 0 & 0 & 0 \\ 0 & 0 & \dot{\varepsilon} \end{bmatrix}, \tag{5.1}$$

where the loading is in the 3-direction and characterized by loading rate $\dot{\varepsilon}$, while the sample is constrained in the transverse 2-direction. The unknown deformation in the 1-direction is found by solving for traction-free boundary conditions. These conditions are closest to experimental reality and do not impose the full deformation gradient as is frequently done in the literature for convenience.

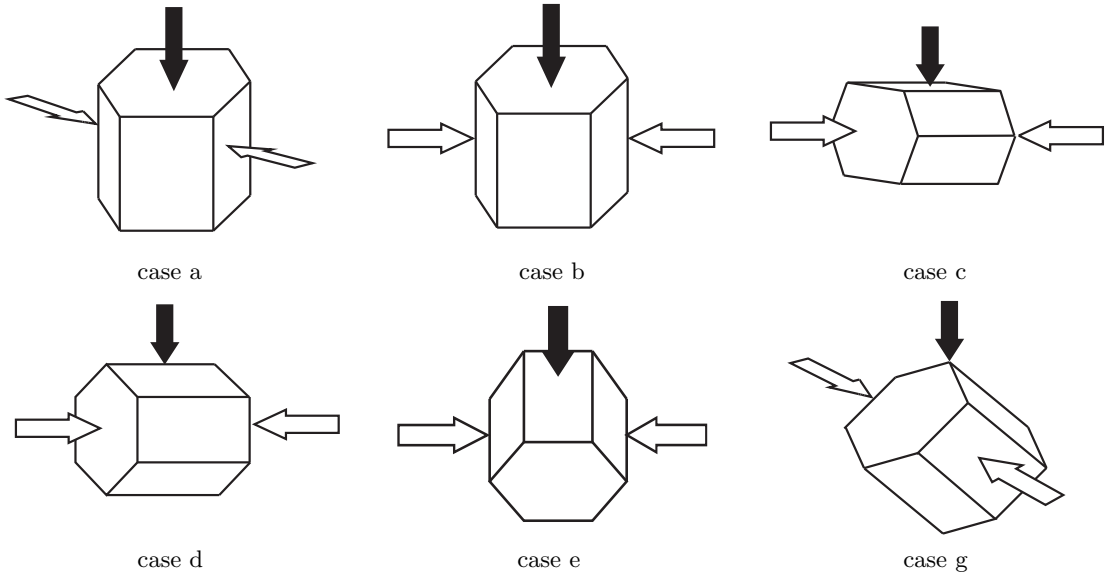

Figure 5.7: Schematic view of plane strain compression test on a differently oriented Mg single crystal from Kelley and Hosford (1968a), where black and white arrows correpond to loading and constraint direction, respectively.

The calibrated parameters for the 12 slip systems and 6 twin systems are summarized in Table 5.1. The corresponding numerical results are shown in Figures 5.8 and 5.9 along with experimental data from Kelley and Hosford (1968a) for comparison. The relative contributions of the various microstructural modes (defined as the ratio of each internal variable to the sum of the all internal

hardening and dissipation parameters		
basal	h_α(MPa)	7100
	σ_∞(MPa)	0.7
	h_{ij}(MPa)	0.0
	τ_0(MPa)	1.75
	m	0.05
	$\dot{\gamma}_0(\mathrm{s}^{-1})$	1.0
prismatic	h_α(MPa)	9000
	σ_∞(MPa)	85
	h_{ij}(MPa)	20
	τ_0(MPa)	1.75
	m	0.05
	$\dot{\gamma}_0(\mathrm{s}^{-1})$	1.0
pyramidal	h_α(MPa)	30000
	σ_∞(MPa)	150
	h_{ij}(MPa)	25.0
	τ_0(MPa)	1.75
	m	0.05
	$\dot{\gamma}_0(\mathrm{s}^{-1})$	1.0
tensile twin	h_0(MPa)	1.7
	k_{ij}(MPa)	40000

Table 5.1: Material parameters of the hardening energies and dissipation potentials for the slip and twin systems.

variables) are also included to demonstrate the activated slip and twin systems. The labeling of the individual load cases corresponds to the original orientations reported by Kelley and Hosford (1968a). We note that the above procedure assumed that only one individual slip or twin system is activated in each of the experiments by Kelley and Hosford (1968a). Of course, one cannot rule out that other systems were activated to a minor extent nor that cross-hardening took place during those experiments. Therefore, the reported hardening parameters should be understood as effective hardening parameters.

- **Compression along the** $\langle 0001 \rangle$**-axis**:

  In loading cases a and b, the loading direction is along the $\langle 0001 \rangle$-axis. These two loading scenarios are theoretically prone to activate the compression twin system, which, however, is rarely observed experimentally in the early stages of deformation. Kelley and Hosford (1968a) explained this behavior by a small albeit sufficient misalignment of the sample orientation, which immediately leads to the activation of basal slip. In the ideally oriented scenario

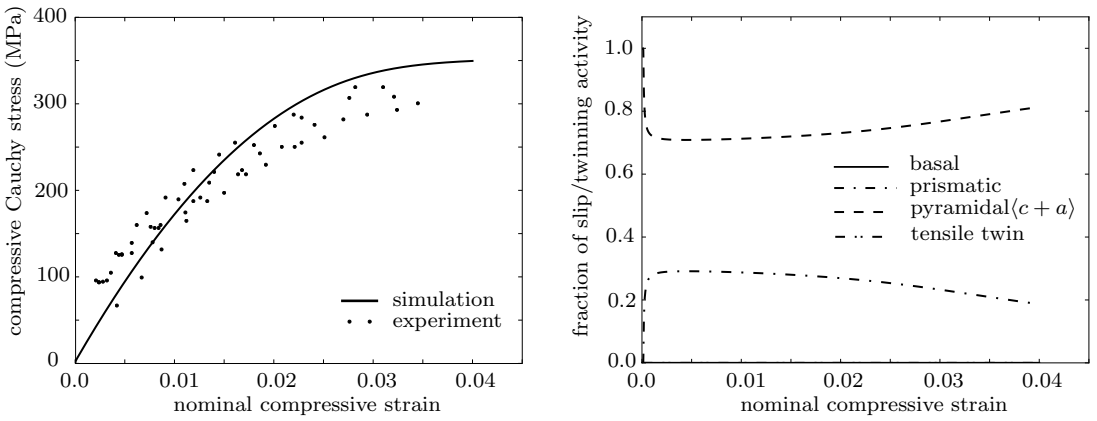

Case a: compression along the ⟨0001⟩-axis.

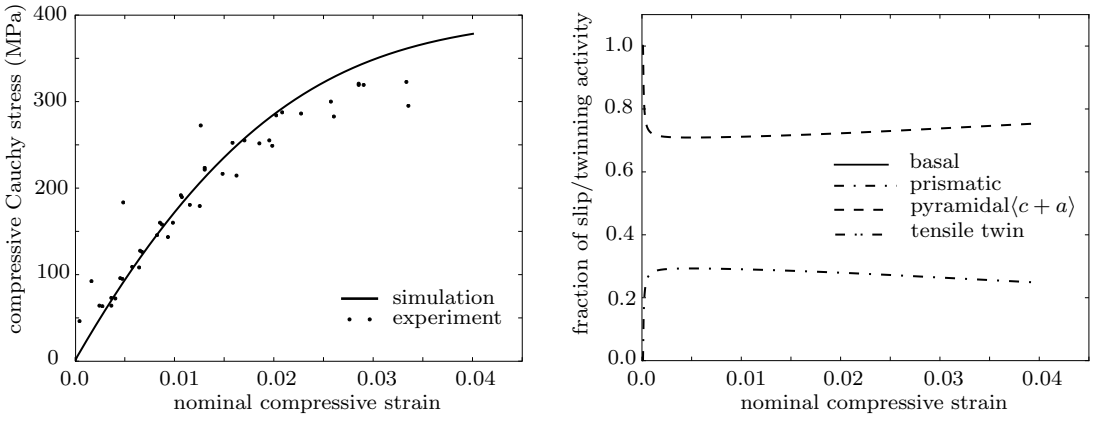

Case b: compression along the ⟨0001⟩-axis.

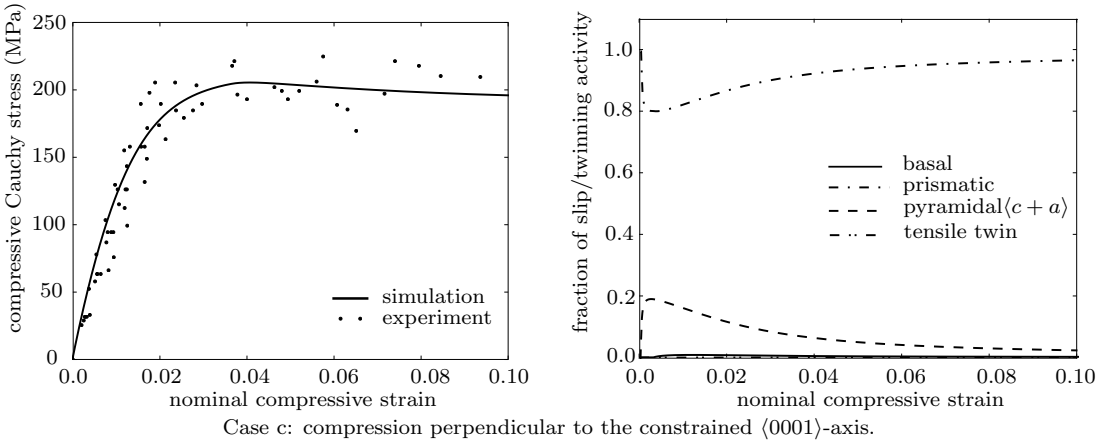

Case c: compression perpendicular to the constrained ⟨0001⟩-axis.

Figure 5.8: Numerical results for plane-strain compression compared to experimental data of Kelley and Hosford (1968a).

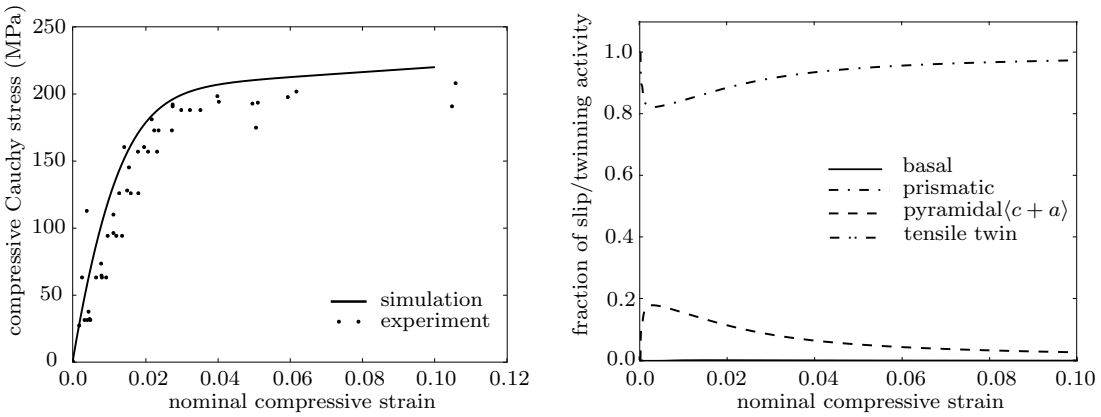

Case d: compression perpendicular to the constrained ⟨0001⟩-axis.

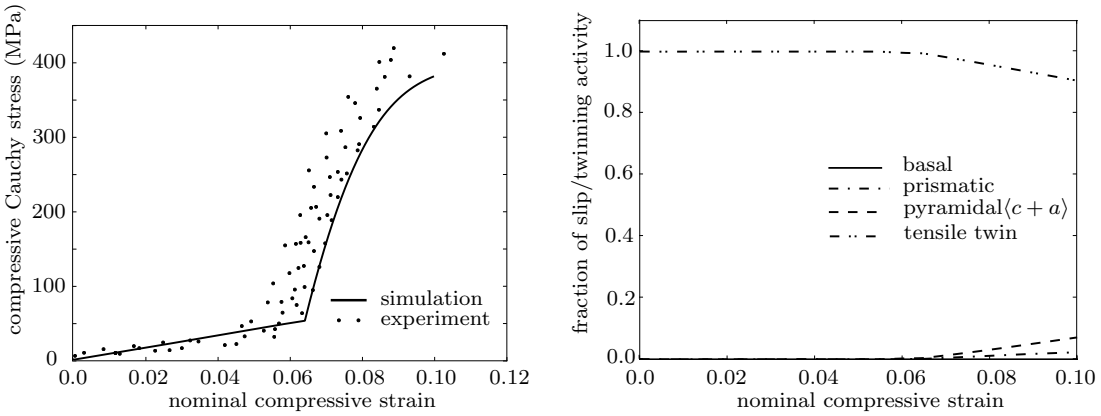

Case e: compression perpendicular to the unconstrained ⟨0001⟩-axis.

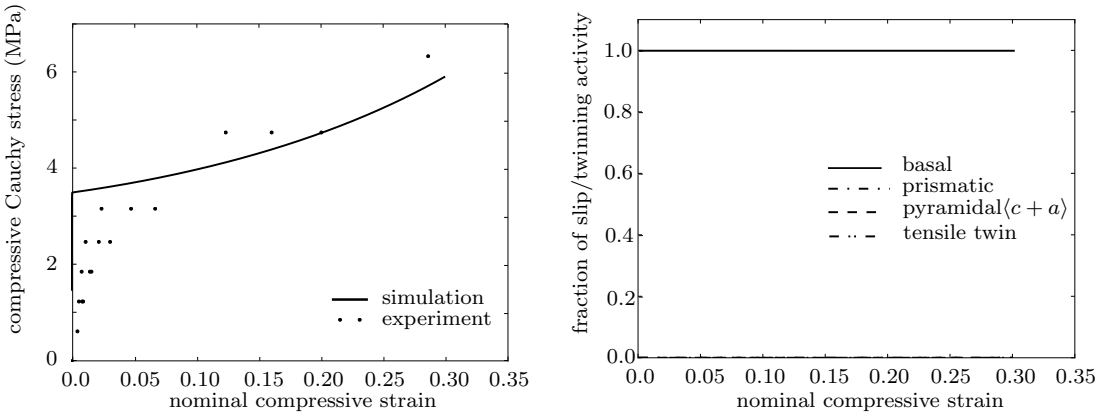

Case g: compression oriented for basal slip.

Figure 5.9: Numerical results for plane-strain compression compared to experimental data of Kelley and Hosford (1968a), continued.

studied here, we use this case to identify the parameters of the pyramidal $\langle c+a \rangle$ system in the model. As seen in Figure 5.8, the stress-strain responses observed in both cases are qualitatively identical with a slightly higher stress level in case b. This agrees with experimental observations by Kelley and Hosford (1968a) and with previous simulated results by Zhang and Joshi (2012). For both cases, the pyramidal slip mode dominates with over 80% of all slip activity, whereas contributions from basal slip and tensile twinning are negligible. The rather small contributions of prismatic slip in the early stages of deformation are immediate results of the reorientation of the crystal undergoing pyramidal slip. Yet, since the resolved shear stress on the pyramidal systems is considerably higher, the prismatic slip activity drops gradually.

- **Compression perpendicular to the constrained $\langle 0001 \rangle$-axis**:

  In loading cases c and d, compression is perpendicular to the $\langle 0001 \rangle$-direction and the sample is constrained in the $\langle 0001 \rangle$-direction, which is therefore oriented to produce prismatic slip. Kelley and Hosford (1968a) did not observe traces of prismatic slip, which they theorized to stem from early stages of prismatic slip prelude to the $\{10\bar{1}1\}$ banding. Our results in Figures 5.8 and 5.9 show that the stress-strain responses for these two cases are similar and that plastic deformation primarily stems from prismatic slip and small traces of pyramidal $\langle c+a \rangle$ slip (less than 10% beyond 4% of compression). Basal slip and tensile twinning are not activated in this case.

- **Compression perpendicular to the unconstrained $\langle 0001 \rangle$-axis**:

  In case e, compression is perpendicular to the now unconstrained $\langle 0001 \rangle$-axis, which is favorable to activate the $\{10\bar{1}2\}$ tensile twin system. Kelley and Hosford (1968a) reported the completion of twinning at about 6% of compressive strain, which is followed by a similar behavior as compression along the $\langle 0001 \rangle$-axis (see case a). This is consistent with our simulated results: tensile twinning is completed at about 6.5% compression. Since the $\langle 0001 \rangle$-axis has reoriented by only about 4° with respect to the loading direction, we indeed see a similar behavior as in case a where once the material is fully twinned. Figure 5.9 illustrates how twinning dominates the plastic deformation up to 6.5% compression, from where on we observe a combination of $\langle c+a \rangle$ pyramidal and prismatic slip as observed in experiments.

- **Compression resulting in basal slip**:

Case g is favorable for basal $\{0001\}\langle 1\bar{2}10\rangle$ easy glide, and all plastic straining can be accommodated by a single basal slip system. In fact, Kelley and Hosford (1968a) reported significant basal band formation for this case. Our simulations predict that the stress remains at a rather low level (below 10 MPa) even at large strains (up to 30% of compression). Plastic deformation is exclusively accommodated by basal slip since no other system can operate at such low stress levels.

We note that we have omitted case f from our validation tests for the following reason. This loading scenario is similar to case e (i.e., loading is perpendicular to the unconstrained $\langle 0001\rangle$-axis) but the crystal is rotated by 90° about the $\langle 0001\rangle$-axis. As a consequence, the preferred deformation mode is tensile twinning followed by basal slip (Kelley and Hosford, 1968a). However, the tensile twin system involved in this case results in deformation in the 2-direction, which is suppressed by imposing deformation gradient (5.1) in our material point calculations. In experiments, the boundary conditions can be accommodated since the deformation is not uniform throughout the sample, which allows for stress relaxation by tensile twinning inside the specimen. Such behavior can be accounted for by boundary value calculations, see also Zhang and Joshi (2012). The compression twin is of only little relevance in our subsequent numerical examples; therefore, we assign the same parameters as for the tensile twin systems but with a significantly higher activation stress (hardening modulus $h_0 = 170$MPa). Similarly, pyramidal $\langle a\rangle$ slip could not be calibrated; where required in the following, we adopt those parameters obtained for pyramidal $\langle c+a\rangle$ slip due to a lack of validation data.

Overall, we observe a good quantitative agreement between the experimentally-determined and the numerically-computed stress-strain responses for six of the seven loading cases. In addition (and more importantly), we obtain excellent qualitative agreement between the experimentally-observed slip and twin activity and the simulated evolution of plastic slips and twin volume fractions.

5.4 Model efficiency and stability: comparison to explicit update models

Most available crystal plasticity-based models for slip-twinning interactions in Mg use explicit updates of the internal variables in contrast to the implicit, variational approach presented here.

The latter possesses several advantages over the existing direct updates-based models which discretize the evolution equations (3.18) explicitly. As a consequence, such models commonly assume rate-dependent evolution laws for all internal variables, which is questionable for the evolution of twinning as discussed earlier, see e.g., Ulacia et al. (2010) for the low rate sensitivity of Mg alloys. The present model handles both rate-dependent and rate-independent evolution laws (here, for the plastic slips and the twin volume fractions, respectively) in the same manner. We note that rate-independent plasticity has been modeled successfully through a variety of alternative approaches, including regularized models that remove yield surface singularities (Franciosi and Berbenni, 2007; Yoshida et al., 2009) or new time integration schemes (Schmidt-Baldassari, 2003). However, any explicit scheme requires small load increments and lacks convergence properties, whereas implicit schemes bring about numerical challenges such as the identification of the active set of slip and/or twin systems. For a discussion of rate independence within implicit plasticity modeling and associated challenges see e.g., Kalidindi et al. (1992).

Our variational model admits the treatment of the evolution of the internal variables by both implicit and explicit updates. To demonstrate the advantages of the variational strategy, we have repeated the single-crystal simulations of Section 5.3 with the same model but using explicit updates comparable to conventional crystal plasticity-based models. For each simulation, we identify by numerical experimenting the minimum number of load steps required for the convergence of the variational approach (to less than 0.1% deviation of the stress-strain curve) as well as the minimum number of steps required for the stability of an explicit scheme (internal variables are updated explicitly upon each quasistatic equilibration). For each simulation, these along with the maximum applied strain can be translated into a maximum allowable strain increment. For comparison, we also report the actual run time of each case. Results are summarized in Table 5.2 for different values of the slip dissipation parameters τ_0 in (3.35) and for different strain rates (note that the twinning-dominanted case e is inconclusive since the rate-independent flow rule chosen here does not admit a direct treatment by explicit updates).

Figure 5.10 illustrates the typical oscillatory solution obtained from the explicit scheme before instability. The plot shows results for case d of Section 5.3 simulated by using $7,000$ and $5,000$ load steps (with the maximum strain of 10% this correspond to shear strain increments of $1.4 \cdot 10^{-5}$ and $2 \cdot 10^{-5}$, respectively). Using fewer steps will cause the solver to show exponential instability within the first few load steps. For comparison, we plot the analogous results obtained from the implicit

loading scenario:	a	b	c	d	e	g
implicit updates:	$8.0 \cdot 10^{-4}$ (50)	$1.3 \cdot 10^{-3}$ (30)	$1.0 \cdot 10^{-3}$ (100)	$1.4 \cdot 10^{-3}$ (70)	$6.7 \cdot 10^{-4}$ (150)	$7.5 \cdot 10^{-5}$ (4000)
run time (s):	0.89	0.54	1.09	0.76	2.09	6.58
explicit updates:	$7.3 \cdot 10^{-6}$ (5500)	$7.8 \cdot 10^{-6}$ (5100)	$1.0 \cdot 10^{-5}$ (10000)	$9.0 \cdot 10^{-6}$ (11000)	NA (NA)	$5.0 \cdot 10^{-6}$ (50000)
run time (s):	0.59	0.48	1.07	1.26	NA	4.60

(The above results are for $\tau_0 = 1.75$ MPa, the applied strain rate is 10^{-5}s^{-1}.)

loading scenario:	a	b	c	d	e	g
implicit updates:	$4.0 \cdot 10^{-3}$ (10)	$4.0 \cdot 10^{-3}$ (10)	$2.0 \cdot 10^{-3}$ (50)	$2.5 \cdot 10^{-3}$ (40)	$1.0 \cdot 10^{-3}$ (100)	$2.3 \cdot 10^{-4}$ (1300)
run time (s):	0.18	0.19	0.60	0.46	1.65	2.15
explicit updates:	$1.1 \cdot 10^{-5}$ (3500)	$1.5 \cdot 10^{-5}$ (2700)	$1.7 \cdot 10^{-5}$ (6000)	$1.4 \cdot 10^{-5}$ (7000)	NA (NA)	$1.0 \cdot 10^{-5}$ (30000)
run time (s):	0.33	0.24	0.66	0.79	NA	2.86

(The above results are for $\tau_0 = 3.5$ MPa, the applied strain rate is 10^{-5}s^{-1}.)

loading scenario:	a	b	c	d	e	g
implicit updates:	$1.3 \cdot 10^{-3}$ (30)	$4 \cdot 10^{-3}$ (10)	$1.7 \cdot 10^{-3}$ (60)	$3.3 \cdot 10^{-3}$ (30)	$7.7 \cdot 10^{-4}$ (130)	$3.8 \cdot 10^{-4}$ (800)
run time (s):	0.91	0.23	1.01	0.49	3.27	3.63
explicit updates:	$1.0 \cdot 10^{-5}$ (4000)	$1.1 \cdot 10^{-5}$ (3800)	$1.4 \cdot 10^{-5}$ (7200)	$1.25 \cdot 10^{-5}$ (8000)	NA (NA)	$1.0 \cdot 10^{-5}$ (30000)
run time (s):	0.40	0.37	0.85	0.94	NA	2.74

(The above results are for $\tau_0 = 1.75$ MPa, the applied strain rate is 10^{-2}s^{-1}.)

Table 5.2: Summary of the maximum strain increments suitable for the stable convergence of the implicit and explicit schemes (numbers in parentheses denote the corresponding minimum numbers of load steps) for different values of the slip dissipation parameter and for different strain rates, as determined by numerical experimenting.

updates for 50 load steps in Figure 5.11 on the right (which corresponds to strain increments of 0.2%). Similarly, Figure 5.11 also illustrates implicit results for case a using only 10 load steps and producing convincing agreement with the exact solution obtained from very small strain increments. This confirms the stability and accuracy of the chosen implicit variational scheme at considerably larger steps, thus resulting in superior efficiency over comparable explicit schemes. The increased efficiency enables the investigation of larger samples, more complex grain distributions, and the homogenized material response, to name but a few examples. Here we point out that in Table 5.2, the actual run times from the variational approach do not exhibit strong advantages over the explicit updates. This is due to the fact that the variational approach requires solving a nonlinear system of

equations at the material level of each iteration and is thus more expensive than conventional explicit updates, which only updates the internal variable using an explicit equation after convergence. However, this example is based on a computationally-inexpensive material point calculation, which requires little run time on the global level. Currently, the computation load of most numerical PDE solvers is superlinear (e.g., $\mathcal{O}(N^3)$ for finite elements, $\mathcal{O}(N \log N)$ for spectral methods, where N is interpreted as the number of degrees of freedom of the problem), but the load on the material level scales linearly ($\mathcal{O}(N)$). Thus, the reduction in the number of time steps would be essential for reducing the total run time when dealing with large systems. In addition, it is worth pointing out that the implicit scheme also bears major advantages in terms of numerical stability, whereas the explicit updates are prone to numerical instability.

Of course, the exact findings depend on the details of the chosen numerical algorithms but the general trend is apparent. The results in Table 5.2 show that the number of steps required for the variational approach are significantly (viz., on average a factor of 100) smaller than those of the explicit scheme. Note that we still need a fair amount of steps in order for several cases to converge, especially for easy-glide case g for basal slip. This, however, is purely a convergence issue arising from the employed Newton-Raphson solver.

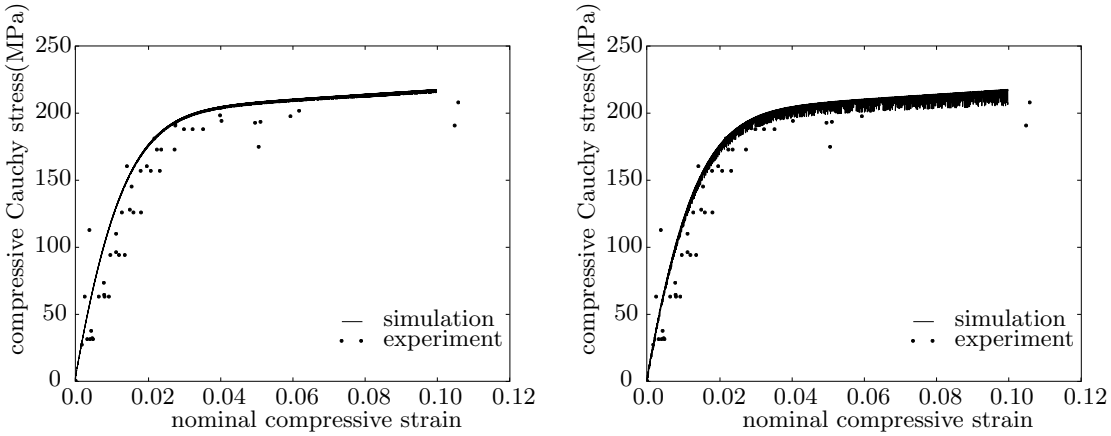

Figure 5.10: Results obtained by using explicit updates for case d of Section 5.3, computed via a total of 7000 load steps (left) and 5000 load steps (right) with $\tau_0 = 3.5$ MPa (i.e., simulations are run right at the stability limit).

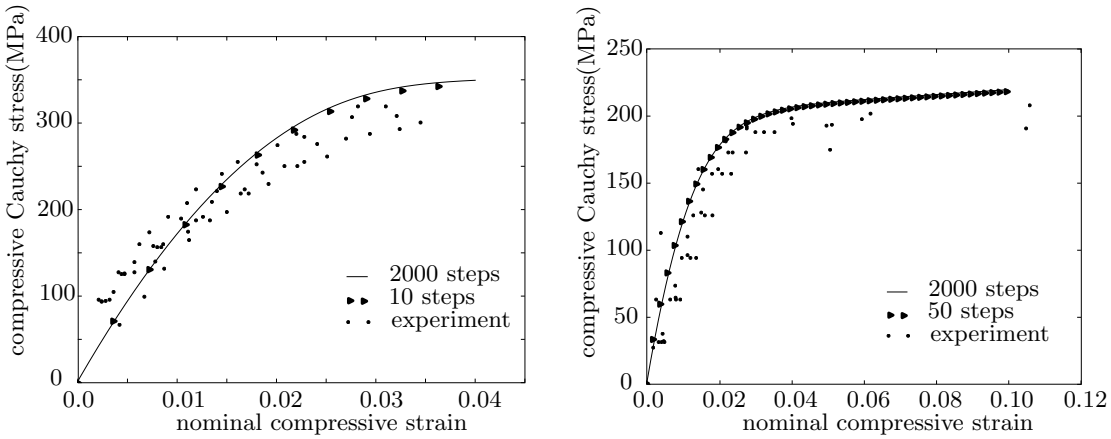

Figure 5.11: Results obtained by using implicit updates for cases a (left) and d (right) of Section 5.3, computed via a total of 10 load steps (left) and 50 load steps (right) and compared to the (approximately) exact solution obtained from a very fine load step in the implicit scheme (with a total of 2000 load steps); as before, $\tau_0 = 3.5$ MPa.

Chapter 6

Simulation of Polycrystalline Magnesium and Texture Evolution

Having validated the single-crystalline response of the variational model for each individual slip system, we use this model to study the combined effects of slip and twinning in polycrystalline Mg. This can be achieved in various ways with different levels of complexity. Here, we use two different approaches and compare their results (this will provide guidelines for their suitability). First, we use a Taylor-type model which does not account for grain interactions and grain boundary mechanisms but allows for the simulation of large numbers of grains, which will allow us to study polycrystalline texture evolution. The averaging scheme of Taylor (1938) assumes that each grain undergoes the same total (macroscopically-applied) deformation; it provides an upper bound on the stress-strain relation and has traditionally been used in texture calculations. For a polycrystal containing n_{g} grains with orientations defined by rotation tensors $\boldsymbol{R}_i \in SO(3)$, the total energy is assumed to be

$$W(\boldsymbol{F}) = \frac{1}{n_{\mathrm{g}}} \sum_{i=1}^{n_{\mathrm{g}}} W(\boldsymbol{R}_i \boldsymbol{F}), \tag{6.1}$$

and the energy of each grain is defined by (4.4). Stress and incremental modulus tensors follow accordingly. Here we mention that our subsequent simulations do not follow a conventional fully-constrained Taylor model assumption. We mimic experiments by a partially defined deformation gradient and solve for the unknown components of the deformation gradient by the stress-free conditions, so that we achieve a more accurate replication of the real experiment. In the subsequent sections, all the Taylor model simulations are performed with this relaxed assumptions on the

deformation gradient, so one may speak of a *relaxed Taylor model*.

Since the Taylor assumption is too restrictive for certain microstructures to develop, we alternatively employ finite element simulations to determine the polycrystalline response. In close analogy to the single-crystal experiments studied above, Kelley and Hosford (1968b) also performed channel die tests on polycrystalline Mg. Here, a finite element simulation of a cubic block undergoing constrained compression is much more suitable than using the Taylor assumption since it admits the operation of slip/twin systems which are otherwise suppressed by the out-of-plane constraints. The spatial variation of deformation mechanisms within the specimen are modeled by linear tetrahedral elements (each quadrature point is assigned a different grain orientation) and the macroscopic response is obtained by imposing suitable boundary conditions.

6.1 Representing texture evolution due to slip and twinning

Although Section 3.1 gives a complete description of the kinematics of slip and twinning, a specific rule based on the kinematics must be given to export information about the lattice orientations for postprocessing purposes. The changes of the lattice orientation during severe plastic deformation can be extracted from the evolution of the internal variables, as is commonly performed in the context of crystal plasticity, see e.g., Asaro (1983), Asaro and Needleman (1985) and Ahzi et al. (1993). Here, we follow a similar approach but with modifications to incorporate the reorientation effects due to twinning. Using (3.3), the plastic contribution to the rate of stretching tensor is given by

$$\dot{\boldsymbol{F}}\boldsymbol{F}^{-1} - \dot{\boldsymbol{F}}_{\mathrm{e}}\boldsymbol{F}_{\mathrm{e}}^{-1} = \boldsymbol{D}_{\mathrm{in}} + \boldsymbol{\Omega}_{\mathrm{in}} = \boldsymbol{F}_{\mathrm{e}}\tilde{\boldsymbol{l}}_{\mathrm{in}}\boldsymbol{F}_{\mathrm{e}}^{-1}, \tag{6.2}$$

where $\boldsymbol{D}_{\mathrm{in}}$ and $\boldsymbol{\Omega}_{\mathrm{in}}$ are the symmetric and antisymmetric parts of the inelastic velocity gradient, defining the stretching rate and the spin tensor of the inelastic deformation. The total rates of the stretch and spin tensors decompose additively into their elastic and inelastic parts, i.e.,

$$\boldsymbol{D} = \boldsymbol{D}_{\mathrm{e}} + \boldsymbol{D}_{\mathrm{in}}, \qquad \boldsymbol{\Omega} = \boldsymbol{\Omega}_{\mathrm{e}} + \boldsymbol{\Omega}_{\mathrm{in}}, \tag{6.3}$$

where $\boldsymbol{D}$ and $\boldsymbol{\Omega}$ correspond to the stretching rate and spin tensor of the total deformation, respectively. Since the lattice structure is assumed to remain unaffected by plastic deformation, the reorientation is governed by the elastic spin tensor $\boldsymbol{\Omega}_{\mathrm{e}} = \boldsymbol{\Omega} - \boldsymbol{\Omega}_{\mathrm{in}}$, which we use to obtain the lattice

rate of rotation, i.e., the rate of rotation of the c-axis (represented by unit vector $\boldsymbol{c}$):

$$\dot{\boldsymbol{c}} = \boldsymbol{\Omega}_{\mathrm{e}}\, \boldsymbol{c}, \tag{6.4}$$

In incremental form this results in

$$\boldsymbol{c}(t^{n+1}) = \exp(\boldsymbol{\Omega}_{\mathrm{e}} \Delta t)\, \boldsymbol{c}(t^{n}). \tag{6.5}$$

Twinning affects the lattice orientation by a reflection about the twin plane, which can have a significant effect on the texture evolution in polycrystals (Clausen et al., 2008) and is therefore accounted for. As discussed in Section 3.3.3, we only allow one twin system to operate at a time. Consequently, we apply the corresponding lattice reflection as soon as one of the twin volume fractions λ_β exceeds a system-specific threshold, i.e.,

$$\boldsymbol{c}(t^{n+1}) = \boldsymbol{Q}_\beta\, \boldsymbol{c}(t^{n}) \qquad \text{if} \quad \lambda_\beta(t^n) < \lambda_{\mathrm{cr},\beta}, \quad \text{and} \quad \lambda_\beta(t^{n+1}) > \lambda_{\mathrm{cr},\beta}, \tag{6.6}$$

where $\boldsymbol{Q}_\beta$ is the reflection tensor of twin system β as defined in (3.5). The values of $\lambda_{\mathrm{cr},\beta}$ represent the physical thresholds at which the crystal may be regarded as being in a fully-twinned orientation. In the following numerical examples, we use $\lambda_{\mathrm{cr},\beta} = 0.8$ (the exact numerical value has only a limited influence on the simulated final results since it only affects the postprocessing of the simulated internal variable evolution).

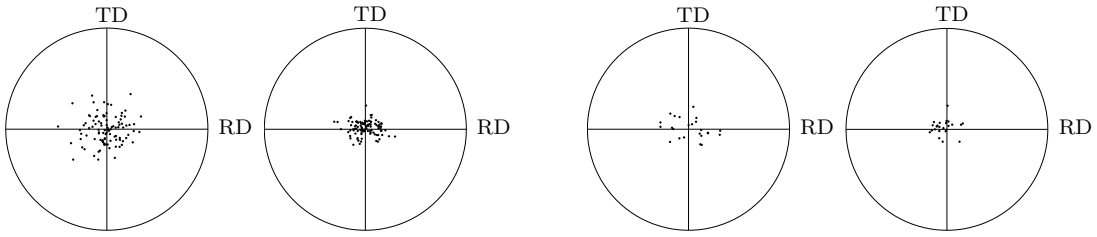

(a) initial textures used in the relaxed Taylor model

(b) initial textures used in FE simulations

Figure 6.1: Initial textures used for polycrystalline Mg samples for plane-strain compression tests (total of 100 grains for the Taylor model and a reduced set of 24 grains for FE simulations); shown are (0001)-poles aligned with the ND. Left and right pole figures in both (a) and (b) are for cases loading cases zt and rt, respectively.

6.2 Polycrystalline Mg – comparison with experiments

Kelley and Hosford (1968b) performed compression experiments on polycrystalline Mg, whose general setup is identical to that used for our single-crystalline simulations in Section 5.3. In their experiments, the polycrystalline Mg samples were obtained from cold rolling, which implies an initial texture with basal poles closely aligned with the rolling normal direction (ND). Here, we adopt the notation of Kelley and Hosford (1968b): each plane-strain compression test is characterized by two letters, the first denoting the axis of compression and the second one denoting the unconstrained axis. Therefore, the orientations in the cold-rolled samples are defined by the normal direction (ND, denoted by z), the rolling direction (RD, abbreviated as r), and the transverse direction (TD, t). As two selected examples, we demonstrate the performance of our model by simulating the responses of cases zt and rt and comparing to the experimental data using both a finite element model and the Taylor model. Both models start with initial grain distributions whose basal poles are closely aligned with the rolling ND, as shown in Figure 6.1. Experiments may be expected to have exhibited a spread of the initial textures as well. Numerical results for both loading cases are summarized in Figure 6.2. Because of the constraints in the Taylor model (and because of its efficiency), we simulate more grains (here, a total of 100) than in FE calculations (where only 24 grains appear sufficient). Results in Figure 6.2 indicate that both models predict similar stress-strain responses (with a slightly better qualitative agreement of the finite element results). The relative contributions of the slip/twin systems (also shown in the figure) are almost identical in the Taylor and FE models, which is why we only show results obtained from the Taylor approach.

- In **case** zt, the loading direction is aligned with the ND while the TD is unconstrained. The initial texture is assumed to have a wider spread than in case rt, cf. Figure 6.1. This is reasonable since the experimentally-determined stress level of Kelley and Hosford (1968b) for this case is low (around 200 MPa) compared to the single-crystal compression cases a and b in Section 5.3 (stress levels were near 300 MPa). Hence, a fair amount of basal activity is required to reduce the stress. The results obtained from FE calculations and from the Taylor model are quite similar both in the stress-strain response and in the relative contributions of the different slip/twin systems. Unlike in the single-crystal cases in Section 5.3, not a single slip system dominates the process but all slip modes are activated, combining basal, prismatic,

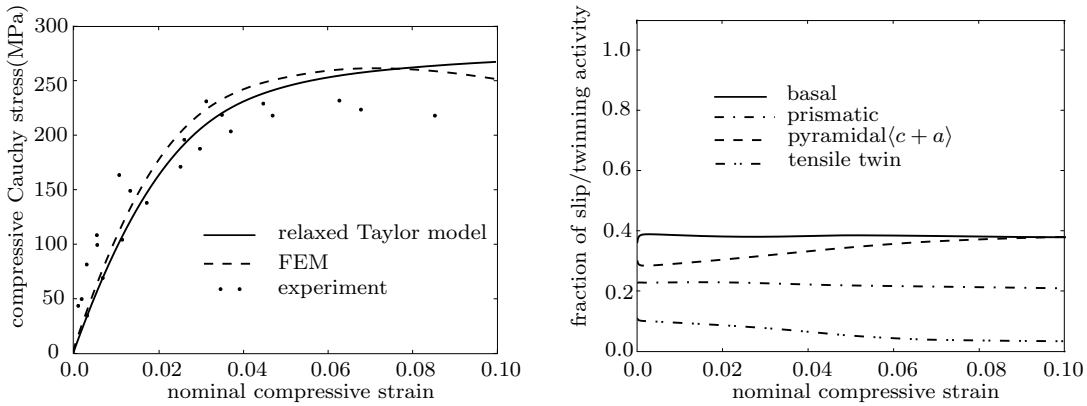

Case zt: loading in the normal direction (ND); transverse direction (TD) unconstrained

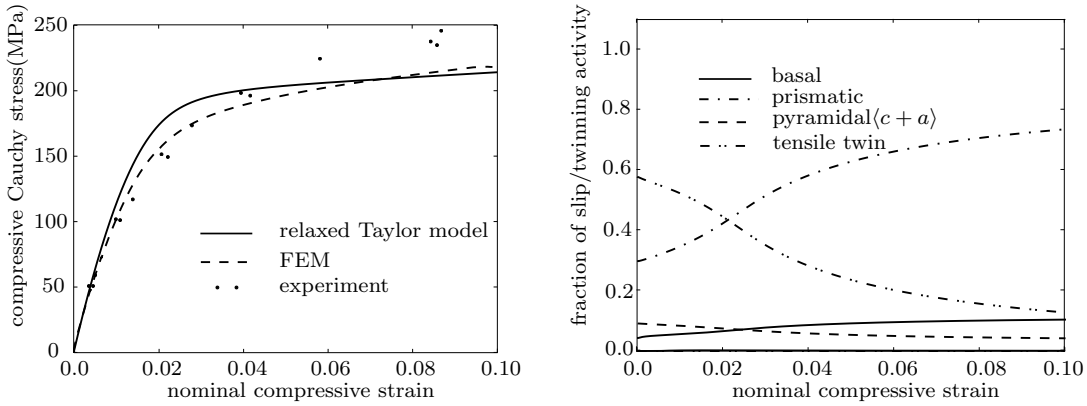

Case rt: loading in the rolling direction (RD); transverse direction (TD) unconstrained

Figure 6.2: Numerical results for plane-strain compression of Mg polycrystals compared to experimental data of Kelley and Hosford (1968b). Shown are the stress-strain responses as well as the relative contributions of all slip/twin modes.

and pyramidal $\langle c+a \rangle$ slips. In contrast, tensile twinning appears less pronounced.

- In **case** rt, the loading direction coincides with the RD and the TD remains unconstrained. The results from FE calculations and from the Taylor model again agree fairly well. The dominant deformation mode in both cases is prismatic slip like in single-crystal cases c and d in Section 5.3. We also see a small amount of tensile twinning at low strains, which results from the spreading of basal poles around the ND.

It is important to note that we compare numerical stress-strain predictions (without having fitted the model to any polycrystalline data) to independent polycrystalline experimental results. Both experiments and simulations contain numerous potential error sources which may lead to the

discrepancies between the simulated results and the experimental data, including the following: the texture evolution depends significantly on the initial texture and on the loading history, in almost all computational approaches, our simulations start with a specific initial texture which mimics the experimental reality but cannot agree exactly with the physical microstructure, among others due to limited resolution and computational costs; we assume a textured but virgin state of the material; i.e., although an initial texture is accounted for, we assume that the internal variables display no hardening history. This is, of course, not the case in experiments, since the textured sample was produced by large plastic deformation. Unfortunately, there is no (simple) way to infer the exact amounts of pre-existing plastic slips in the initial sample (and no such data are available). In addition, as explained in Section 5.3, the only way to identify the model parameters for pyramidal $\langle c+a \rangle$ slip is through experimental data for c-axis compression, which is consistent with the approaches of Homayonifar and Mosler (2011, 2012), and Zhang and Joshi (2012), for example. However, this loading scenario is prone to produce small amounts of basal slip due to sample misalignment. Thus, a further error source arises from the difficulty in cleanly isolating the individual slip and twin modes in experiments. In summary, various potential error sources exist which are hard to account for in simulations. However, considering that the results were produced without fitting the model to polycrystalline data (and considering that the model is the first variational model of its type), the comparison of the experimental and simulated responses shown in our simulation are convincing.

6.3 Cold rolling example

Cold rolling is a common metal forming process that results in pronounced texture evolution. In the process, metals pass through the roller several times (Figure 6.3), during which the metal undergoes severe shear-compression deformation in the extrusion plane.

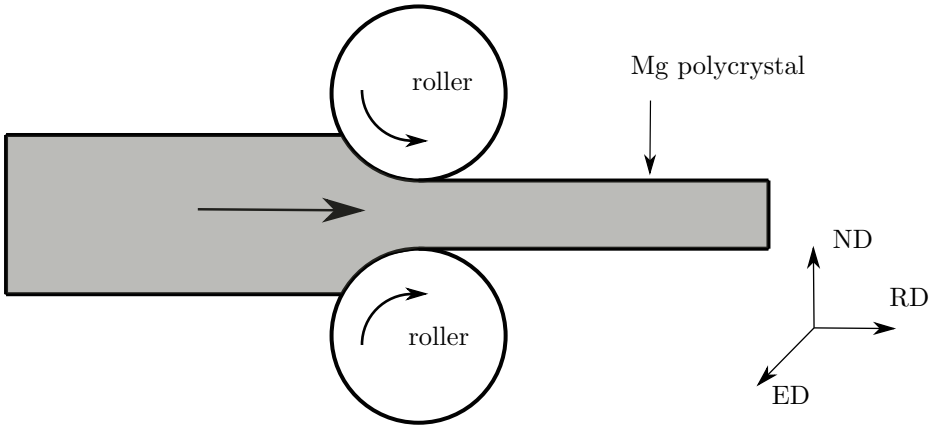

Figure 6.3: Schematic of cold rolling process.

Experimental evidence indicates that plastic deformation during cold rolling primarily leads to the alignment of basal planes with the rolling direction (RD) with increasing deformation (Sandlöbes et al., 2011). As pointed out e.g., by Lee and Duggan (1991), the deformation during the rolling process is characterized by superimposed shear and compressive strains. Following Ahzi et al. (1993), we simulate the effect of cold rolling by imposing a total velocity gradient $\boldsymbol{l}$ that contains both shear (with rate $\dot{\gamma}$) and plane-strain tension-compression (with rate $\dot{\varepsilon}$) according to

$$\boldsymbol{l} = \begin{bmatrix} \dot{\varepsilon} & 0 & \dot{\gamma} \\ 0 & 0 & 0 \\ 0 & 0 & -\dot{\varepsilon} \end{bmatrix}. \tag{6.7}$$

Here, the three coordinate directions (1, 2, and 3) correspond to the rolling direction (RD), the transverse direction (TD), and the normal direction (ND), respectively. The shear to normal strain rate ratio

$$\alpha = \dot{\gamma}/\dot{\varepsilon} \tag{6.8}$$

is a characteristic property of the geometry of the rolling device. Here and in the following, we take $\alpha = 3$ to account for the fact that shear deformation dominates the rolling process, cf. Ahzi et al. (1993) for a discussion. When starting from the virgin state of the material at time $t = 0$, the velocity gradient (6.7) can be integrated analytically, which leads to the volume-preserving total

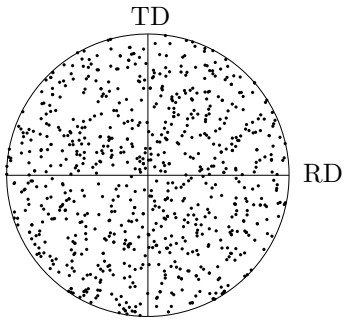

Figure 6.4: Initial texture distribution showing (0001)-poles are randomly-oriented at the beginning of each cold rolling simulation (with a total of 800 grains)

deformation gradient

$$\boldsymbol{F}(t) = \begin{bmatrix} e^{\dot{\varepsilon}t} & 0 & \dot{\gamma}t \\ 0 & 1 & 0 \\ 0 & 0 & e^{-\dot{\varepsilon}t} \end{bmatrix}. \tag{6.9}$$

Consequently, for an initial thickness H of a sample being rolled to thickness h, the relative thickness reduction during the rolling process follows as

$$\Delta H/H = (H-h)/H = 1 - e^{-\dot{\varepsilon}t}. \tag{6.10}$$

6.3.1 Texture evolution during cold rolling

As discussed in Section 3.3.2, the complexity of the lattice structure of Mg is oftentimes described by only a reduced set of slip and twin systems, whose choice may lead to different material behavior. Here, we demonstrate the importance of an appropriate choice of the relevant systems by studying texture evolution in polycrystalline Mg, specifically accounting for

i) basal, prismatic, and pyramidal $\langle a \rangle$ slip systems and $\{10\bar{1}2\}\langle\bar{1}011\rangle$ tensile twin systems.

ii) basal, prismatic, and pyramidal $\langle c+a \rangle$ slip systems and $\{10\bar{1}2\}\langle\bar{1}011\rangle$ tensile twin systems.

iii) basal, prismatic, and pyramidal $\langle a \rangle$ slip systems and $\{10\bar{1}1\}\langle\bar{1}012\rangle$ compression twin systems.

For each case, Taylor-type simulations contain 800 initially randomly-oriented grains without pre-texture, as shown in the (0001)-pole figure in Figure 6.4 (each dot in the figure denotes an individual grain, and is projected into the TD-RD plane using a stereographic projection). We

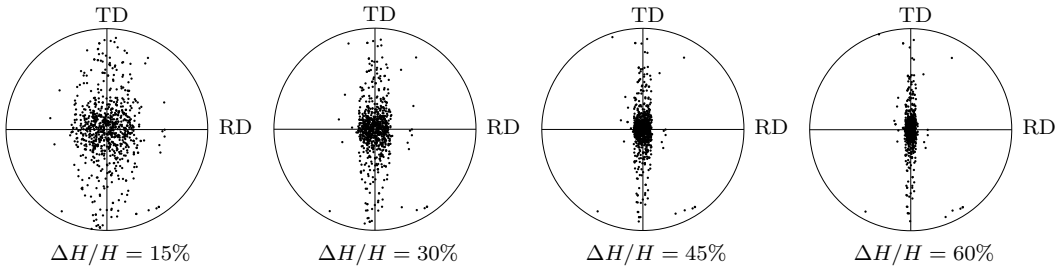

Figure 6.5: Case i: texture evolution during the cold rolling process, showing (0001)-poles moving towards the ND.

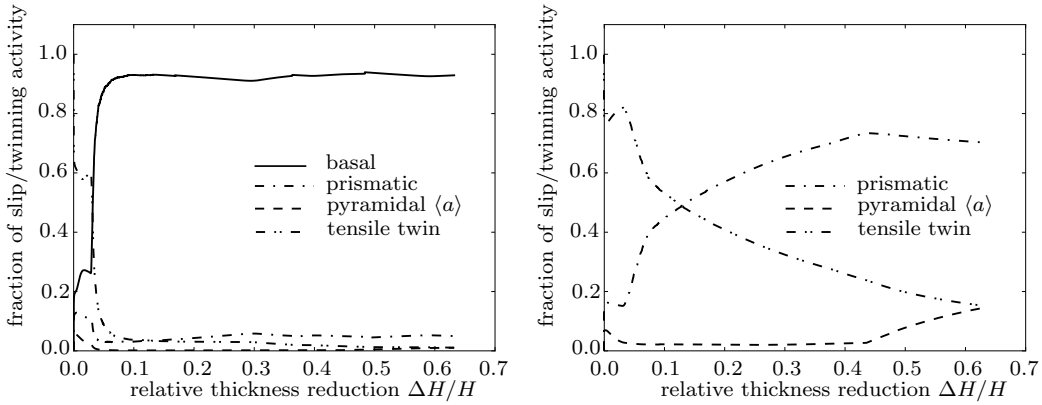

Figure 6.6: Case i: relative contributions of slip and twin systems to the response shown in Figure 6.5. The left figure shows all slip/twin system contributions; the right figure shows the contributions without the dominant basal slip.

apply a constant strain rate of $\dot{\varepsilon} = 1 \times 10^{-5}$. The resulting grain distribution for each of the three cases at thickness reductions of $\Delta H/H = 15\%$, 30%, 45% and 60% is illustrated by (0001)-pole figures as well as the fraction of relative slip-twin activity during the process. Since basal slip dominates with more than 90% of all plastic activity, we also show the relative activity of the remaining slip/twin systems excluding basal slip.

- **case i: pyramidal $\langle a \rangle$ slip systems are included while pyramidal $\langle c+a \rangle$ slip systems are not included**

  Pyramidal $\langle c + a \rangle$ slip has been rarely observed during cold rolling, which is why we include the pyramidal $\langle a \rangle$ systems rather than pyramidal $\langle c + a \rangle$ slip. Figure 6.5 illustrates the resulting grain distributions with increasing levels of thickness reduction. Figure 6.6 shows

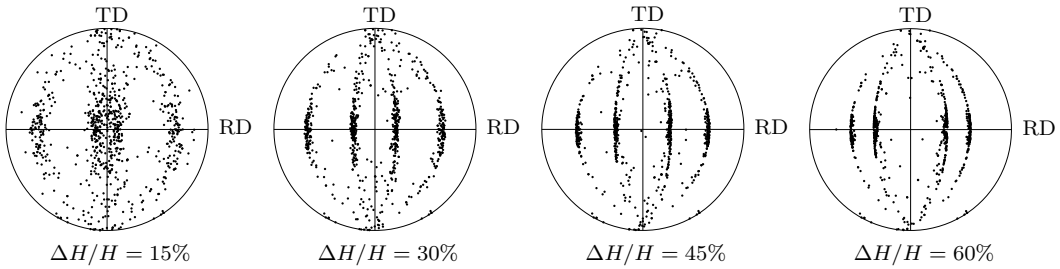

Figure 6.7: Case ii: texture evolution during the cold rolling process shown by (0001)-pole figures.

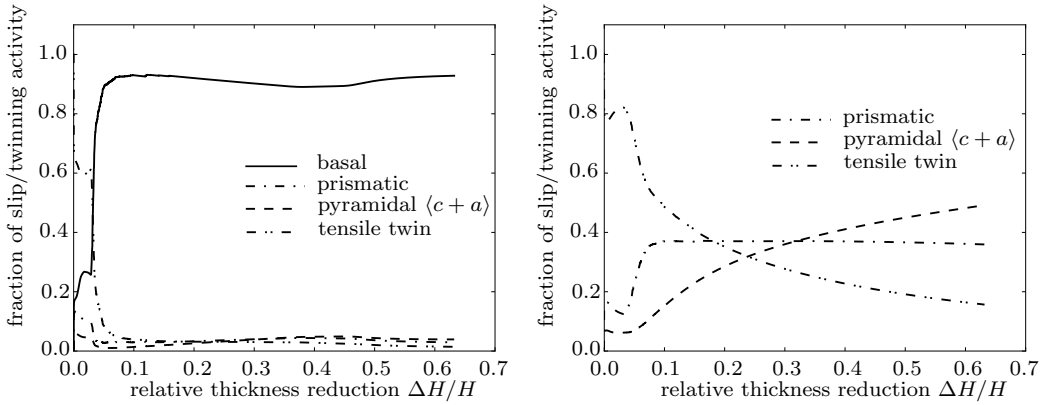

Figure 6.8: Case ii: relative contributions of slip and twin systems to the response shown in Figure 6.7. The left figure shows all slip/twin system contributions; the right figure shows the contributions without the dominant basal slip.

the relative activities of each slip/twin system. Obviously, the (0001)-poles gradually move towards the rolling ND, which is mainly due to activity on the basal slip systems (more than 90% of the total slip is basal). Note that the alignment of the grain orientations in the rolling direction is considerably faster than in the transverse direction. This can be explained by the direction of the applied simple shear. In technological applications, typical cold rolling procedures often involve several passes of a single work piece through the rolling device, and each pass can be performed with a different rolling direction, which ultimately leads to a faster directional alignment. It is important to note that, although the overall plastic deformation of the polycrystal is mainly the result of basal slip activity, we do observe a significant number of grains undergoing tensile twinning at low deformation levels. At small thickness reductions of $\Delta H/H < 7\%$ more than 60% of the total plastic deformation comes from twinning, see

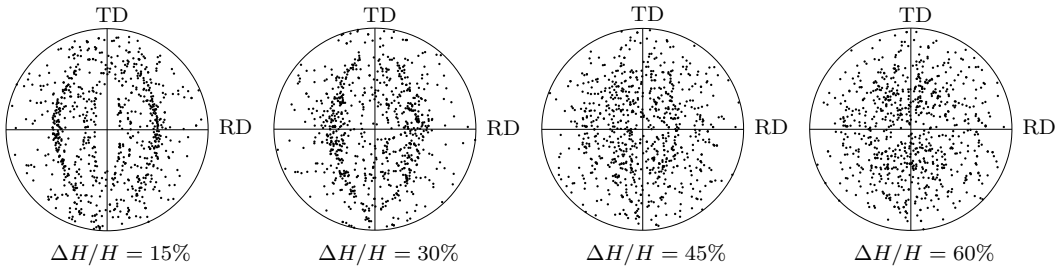

Figure 6.9: Case iii: texture evolution during the cold rolling process shown by (0001)-pole figures.

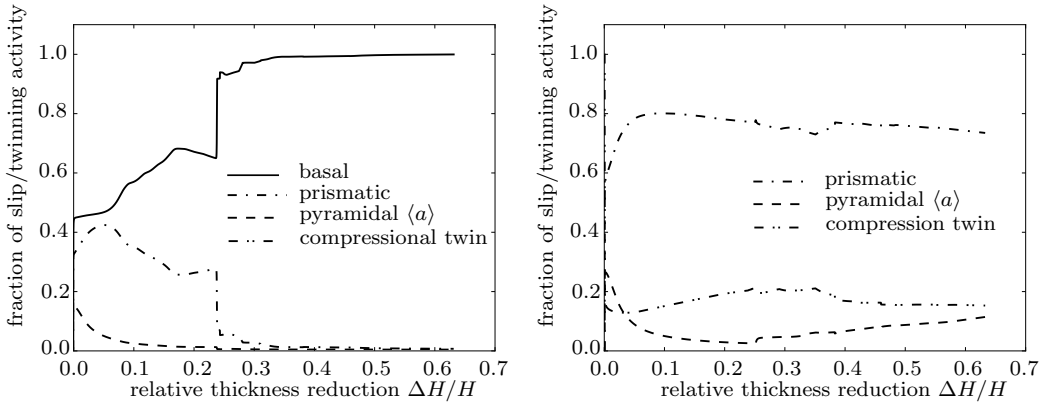

Figure 6.10: Case iii: relative contributions of slip and twin systems to the response shown in Figure 6.9. The left figure shows all slip/twin system contributions; the right figure shows the contributions without the dominant basal slip.

Figure 6.6. However, as those grains approach the twinned states, basal slip activity in the twinned grains catches up and dominates the ensuing deformation.

- **case ii: pyramidal $\langle c+a \rangle$ slip systems are included while pyramidal $\langle a \rangle$ slip systems are not included**

  Most models in the literature have included pyramidal $\langle c + a \rangle$ systems (like we did in Section 5.3) to accommodate non-basal slip. For this case, the grain distribution and the relative activity of each slip/twin system for the same cold rolling scenario are summarized in Figures 6.7 and 6.8, respectively. Here, we observe a quite different texture evolution compared to the previous case. Indeed, the final grain distribution resembles that of plane-strain compression of fcc metals, see e.g., Wang et al. (2010). The activation of the pyramidal $\langle c + a \rangle$ systems tends to reorient the basal slip systems. Although the overall deformation is dom-

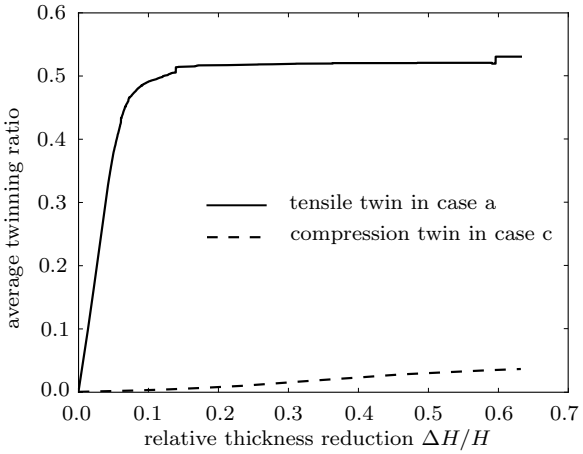

Figure 6.11: Comparison of the average twin volume fractions across all grains for cases i) and iii).

inated by basal activity, the contributions of the pyramidal slip systems (the dashed line in Figure 6.8) are significantly higher than in the previous case.

- **case iii: compression twin systems are included while tensile twin systems are not included** Because of the high critical resolved shear stress and large critical shear strain, compression twins are rarely observed and often omitted in simulated texture predictions, see e.g., Proust et al. (2009) and Homayonifar and Mosler (2011). For illustrative purposes, we include compression twinning (and suppress tensile twinning) to demonstrate its effect on the texture evolution. Grain distribution and relative slip/twin activities for this case are shown in Figures 6.9 and 6.10, respectively. The polycrystal does not develop any preferably-oriented texture in this case because of the high barrier to activate compression twins. Figure 6.11 plots the average volume fractions of tensile twins in case i) and of compression twins in this case across all grains. In case i), the averaged twin volume fractions reach 50% at about 15% of thickness reduction and remain at this level because almost 50% of all grains exhibit tensile twinning. There, due to the low critical shear strain of tensile twinning, after around 15% of thickness reduction nearly all grains that undergo twinning are fully in the twinned orientation and basal slip proceeds to dominate almost all plastic deformation for grains both in the parent and in the twinned orientation. Here, in contrast, compression twins are hard to activate and difficult to complete. When they are the only means to accomodate deformation along the $\langle 0001 \rangle$-axis, we see the average twin volume fractions remain at a very low level

and only increase at large strains. As a consequence, grains will update their orientation even at large strains because of the lattice reorientation due to twinning, which is why the Mg polycrystal is unlikely to develop texture preferences, as seen in Figure 6.9.

In summary, texture development in Mg polycrystals during cold rolling have been simulated by the presented variational model. Basal pole alignment with the normal direction, as frequently seen in experiments on both pure and alloyed Mg (Al-Maharbi et al., 2011; Bohlen et al., 2007; Sandlöbes et al., 2011), can only be predicted without including the pyramidal $\langle c+a \rangle$ slip systems in the Taylor-type model, which is an important observation. No texture development is observed when including the compression twin systems as the only non-basal relaxation scheme because of the high critical resolved shear stress and critical twin volume fraction of the compression twin systems.

6.3.2 Yield surface evolution during cold rolling

In Section 6.3.1, we showed that the simulation of the cold rolling process could predict the typical rolling texture observed in experiments. Here, we go a step further and investigate the impact of severe plastic deformation during the rolling process (up to more than 60% of thickness reduction in the simulation) on the evolution of the material's yield surface. The plastic deformation history permanently alters the material behavior, including an expansion of the elastic stress space due to hardening under combined slip and twinning, e.g., see recent simulations by Lloyd and Becker (2016). The associated evolution of the effective yield surface of the polycrystal is characteristic of the underlying deformation mechanisms and illustrated in Figures 6.12 to 6.15. Specifically, after each level of thickness reduction, we compute the critical resolved shear stresses (CRSS) for each slip and twin system in each grain of the polycrystal. As shown in the graphics, when considering the biaxial tension–compression stress space in the rolling direction (RD) and normal direction (ND), to indicate the yield limit, each slip system in each grain corresponds to two lines lying symmetrically around the origin since slip can happen in both directions, while each twin system is represented by one line because twinning is restricted to occur in only one direction. The total yield surface is then the combination of the yield surfaces of every slip/twin system of all grains (for clarity we illustrate all slip and twin systems separately, whereas the effective yield surface is obtained from their superposition). It is important to note that we consider twinning as plastic deformation

that is not easily removed upon unloading. If twinning is considered as an elastic process so that twinned volume fractions un-twin during unloading, then the twinning yield surface will remain unchanged during the entire simulation. Here, we assume that the twin volume fractions do not change significantly during the unloading process.

We observe that, as can be expected, the yield surfaces corresponding to all slip systems expand with increasing inelastic deformation. Due to the vastly different stress levels that become apparent from Figures 6.12 to 6.15, the basal slip systems dominate the overall yield surface (flow stresses are on the order of 1 MPa). Also apparent is the difference in yield behavior of the slip and twin systems. For all slip systems the yield surface expands symmetrically because the yield stress depends on the accumulated slip ϵ (which evolves irrespective of the sign of plastic slip). In contrast, for the twinning-dominated grains, the yield surface expands asymmetrically, see Figure 6.15, because twinning is a unidirectional mode on each twin system for crystallographic reasons (Christian and Mahajan, 1995).

A further discrepancy between the slip and twin yield surfaces emerges from the activation of the various grains in the polycrystal. Recall that the plots include contributions from all grains. Therefore, the gradual expansion of the innermost yield surface for all slip systems in Figs. 6.12 to 6.14 indicates that most grains must undergo slip-dominated deformation at some point during the rolling process (if a grain does not exhibit plastic slip, the corresponding yield surface contributions remain constant). By contrast, Figure 6.15 shows that the innermost yield surface of the twin systems does not expand significantly, which can be explained by the initially random orientation of grains assumed in our simulation. As a consequence, tensile twinning can only be activated in those grains whose twin system is oriented favorably for tension along the c-axis. However, the random initial orientation distribution implies that this applies to only about half of all grains, while all others cannot activate twinning. Since the yield surface plot includes all crystals in the sample, the total twinning behavior is thus dominated by those grains that remain in their original twinning state. Of course, compression twins would alter the results but are less frequently observed and require much higher activation stresses that would not affect the effective yield surface shown here.

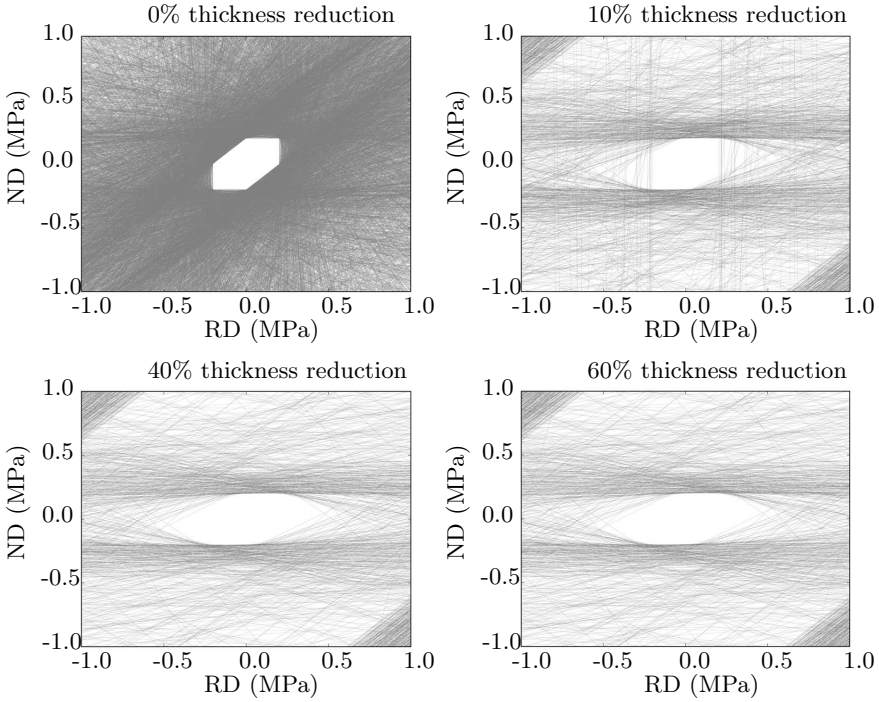

Figure 6.12: Yield surface evolution of the basal slip systems during cold rolling.

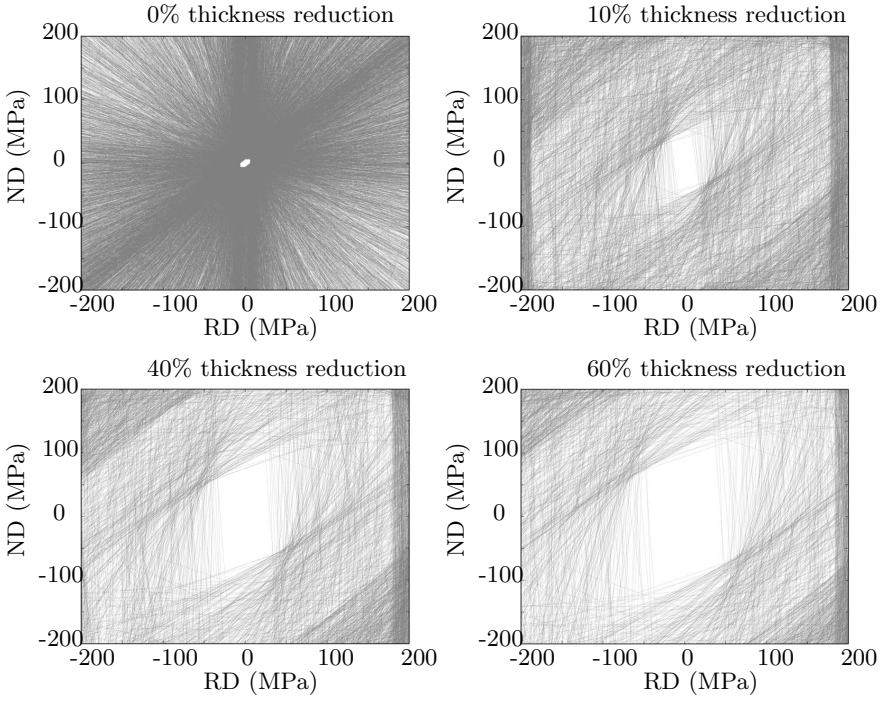

Figure 6.13: Yield surface evolution of the prismatic slip systems during cold rolling.

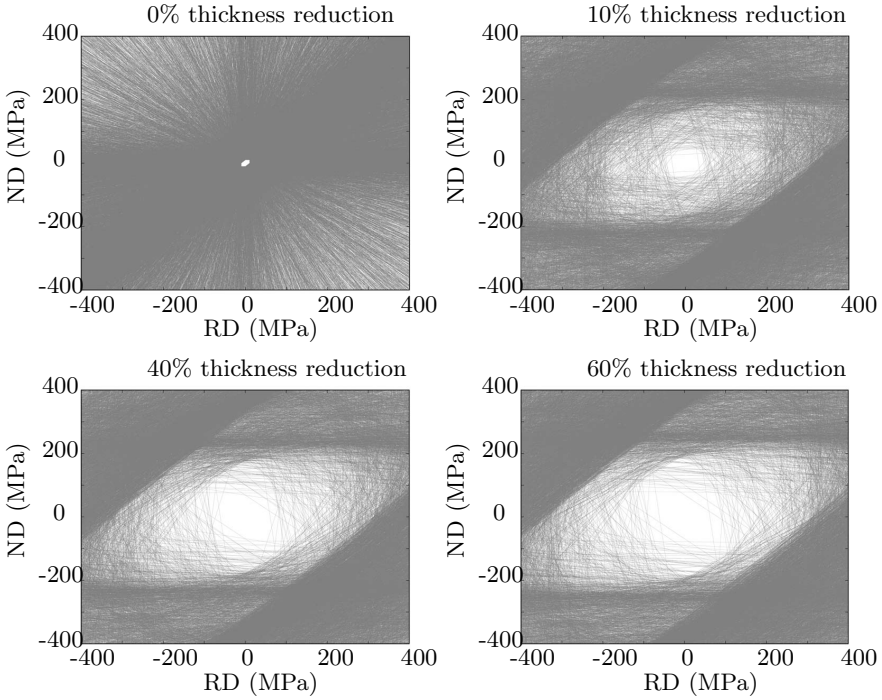

Figure 6.14: Yield surface evolution of the pyramidal slip systems during cold rolling.

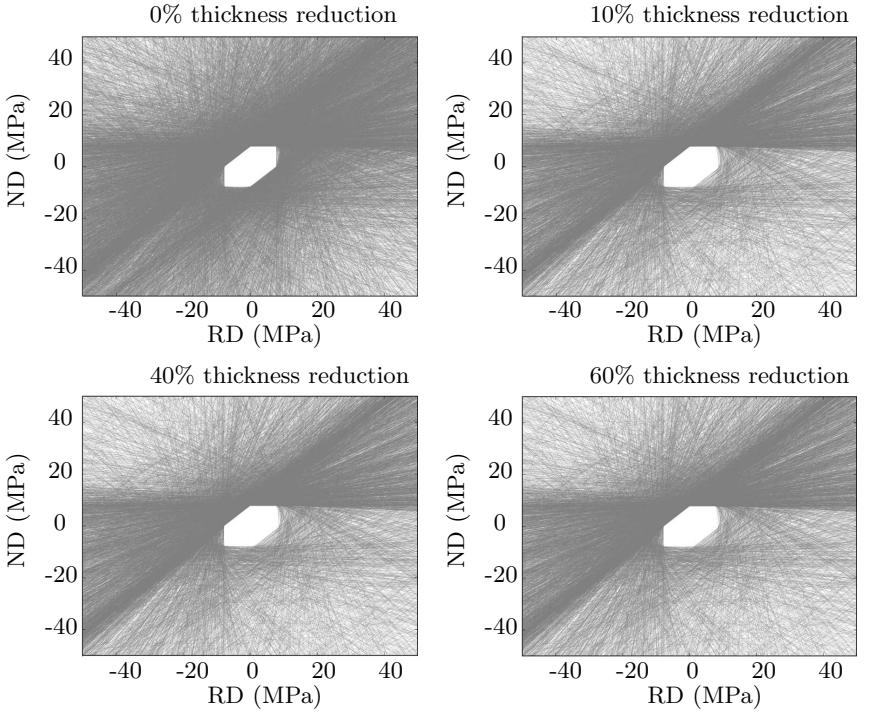

Figure 6.15: Yield surface evolution of the tensile twin systems during cold rolling.

Chapter 7

Uniaxial Compression Study of a Textured Mg Polycrystal

In previous chapters, our model was fit to experimental data from plane strain compression tests (Kelley and Hosford, 1968a,b) and was proven effective to predict the material response during the simulation of the cold rolling process. In this chapter, following the same theoretical framework, we perform a uniaxial compression study on textured Mg polycrystals. In Section 7.1, a hot-extruded Mg polycrystal sample with basal poles spreading around the rolling direction (RD) is studied. Both experiments and our simulation show a two-stage stress-strain curve indicating a twinning-dominated deformation followed by basal/pyramidal slip activity. In Section 7.2, we take a cold-rolled material and compress in both RD and ED, which leads to twinning- and non-twinning-dominated deformation. And lastly, compression with different strain rates is studied to understand the rate dependency of the model. In both sections, simulations are performed with the efficient Taylor model to extract the average material response and the finite element method to capture the detailed deformation of each grain and the microstructural evolution across grains.

7.1 Uniaxial compression of extruded Mg polycrystal

Along with cold rolling, hot extrusion is another common metal processing technique that creates textured Mg polycrystals (Godet et al., 2006). An illustration of this process and the resulting texture charateristics are depicted in Figure 7.1. During the process, the materials are constrained in the die, which imposes shear deformation in the extrusion direction (ED) and compression in the

rolling direction (RD). This deformation reorients the normal to the basal plane to align with the RD. Since the deformation is symmetric around the ED, unlike cold rolling, the basal (0001) poles uniformly spread perpendicular around the ED (Figure 7.1). Because of the spreading of the basal pole, the texture from the extrusion process is considered weaker than the cold rolling process, as pointed out by Dixit et al. (2015).

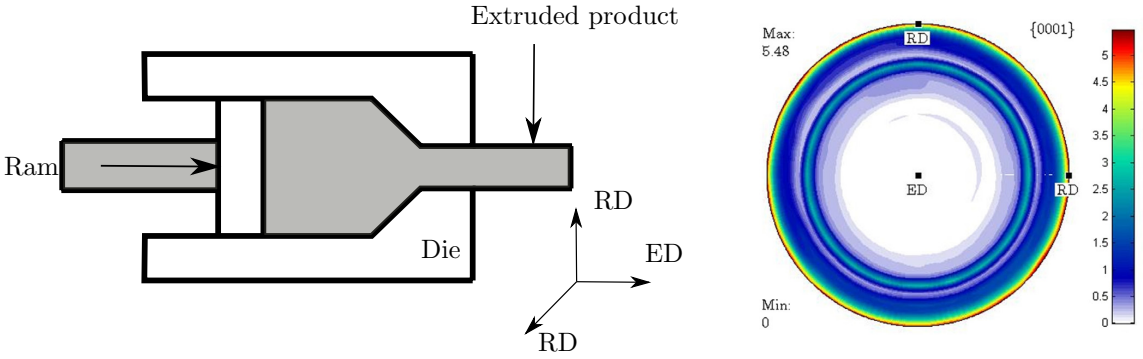

Figure 7.1: Schematic of the extrusion process (left) and the typical resulting texture (right) measured via X-ray diffraction (XRD) from the ED showing a spread of basal (0001)-poles to the ED (Dixit et al., 2015)

.

7.1.1 Experimental study of an extruded Mg polycrystal under uniaxial compression test

Recent experiments (Dixit et al., 2015) investigated the mechanical response of hot-extruded polycrystalline rods of 99.9% pure Mg, where samples were loaded via a conventional Kolsky bar in the ED at high strain rates ($\dot{\varepsilon} \approx 10^3 \mathrm{s}^{-1}$). As shown in Figure 7.1, the hot extrusion process results in samples whose basal poles are spread over the RD, so that the subsequent deformation in uniaxial compression is dominated by tensile twinning in the early stages, followed by a combination of basal and pyramidal slip.

In Figures 7.2 and 7.3, we briefly summarize the major results from Dixit et al. (2015). Figure 7.2 shows the stress-strain behavior from different samples with two loading rates ($\dot{\varepsilon} = 2 \times 10^3 \mathrm{s}^{-1}$ and $4 \times 10^3 \mathrm{s}^{-1}$). These stress-strain curves reflect the commonly observed two-stage behavior, which results in the typical S-shape: at low strains, the stress remains at a low level because of the

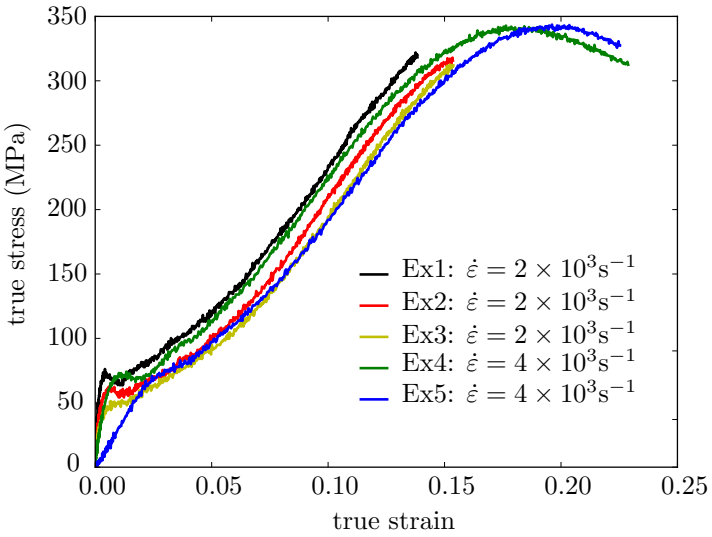

Figure 7.2: Stress-strain responses from Mg polycrystal samples loaded at two different strain rates during Kolsky bar experiments (Dixit et al., 2015), which show a twinning-dominated two-stage deformation.

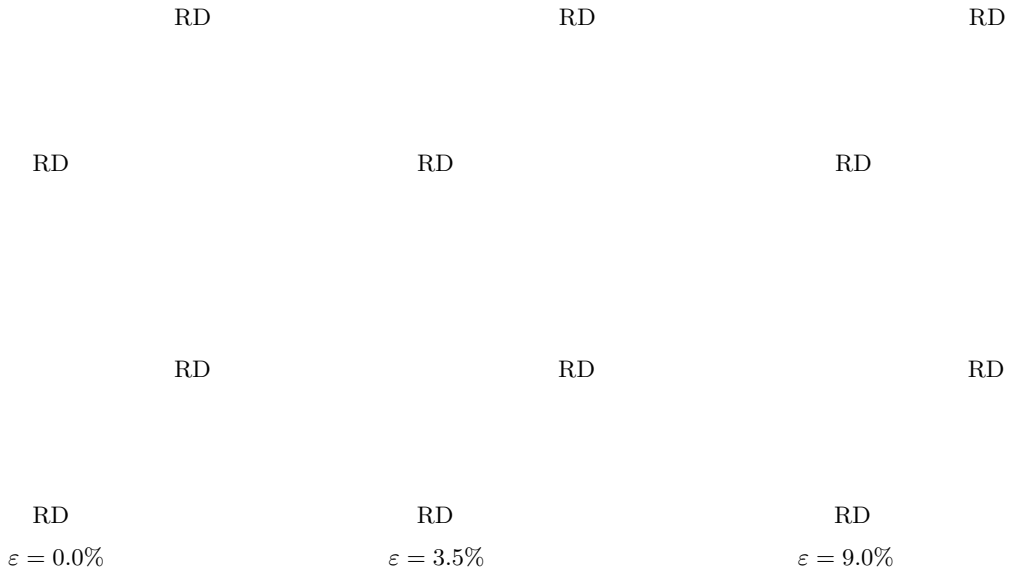

Figure 7.3: Texture evolution depicted by (0001)-pole figures during Kolsky bar experiments obtained from EBSD data measured on three different Mg polycrystal samples (Dixit et al., 2015).

twinning dominance, until twinning is complete and the crystal has reoriented. The second stage after reorientation activates the slip mechanisms and, since most basal poles are aligned with the ED (which is also the loading direction), the majority of plastic deformation comes from the basal systems because of the misalignment between the basal poles and the loading direction. This results in the higher stress level that is observed experimentally. This behavior can also be observed from the (0001)-pole figures shown in Figure 7.3, which are measured through EBSD on three differnt Mg polycrystal samples with different compression strains ($\varepsilon = 0\%, 3.5\%$ and 9.0%). At the start of the experiment, both figures show strong extruded texture, where basal poles are spread around the RD. Since the polycrystal undergoes twinning-dominated deformation, before 9.0% strain, almost all the grains are completely twinned, making the basal poles reoriented towards the ED, which indicates that the rest of the deformation is governed by basal/pyramidal slip. Finally, we need to point out that we do not observe a strong rate dependency in this experiment (the small differences in the stress-strain curve between different samples are due to measurement noise and sample differences).

In the following two sections, we use the models of Chapter 3 to compare the simulated response for the aforementioned compression experiments to the experimental findings. Simulations make use of either a Taylor model (Taylor, 1938) or a finite element (FE) discretization of the polycrystal. The Taylor model is efficient and assumes that all the grains undergo the same deformation, so that the stress response is determined from averaging over all grains (Chang and Kochmann, 2015). The FE model (see Figure 7.4) captures interactions between grains and resolves microstructure evolution with much more detail at the expense of higher computational costs.

The initial texture for the simulation is obtained from the EBSD data in Dixit et al. (2015), as shown in Figure 7.4, which consists of 168 grains whose basal poles are roughly aligned with the RD. For the FE simulation, we construct a cylindrical pillar made up of 168 grains and a total of $18,814$ tetrahedral elements; the ED is aligned with the longitudinal axis of the pillar. To mimic the Kolsky bar test, the sample is compressed quasistatically at a strain rate of $\dot{\varepsilon} = 10^3 \mathrm{s}^{-1}$ up to a total compressive strain of 15%. The loading is sufficiently slow to neglect inertial effects and therefore to admit the assumption of quasistatic conditions. We note that since the EBSD data in Dixit et al. (2015) were obtained from the sample surface, the actual texture distribution may deviate from the one used in our simulations but, as in their study, we assume that the obtained EBSD data are representative for the entire sample.

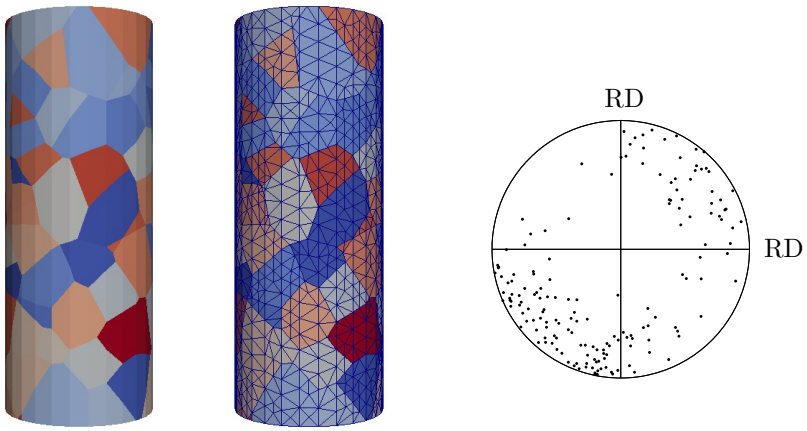

Figure 7.4: FE representation of the extruded polycrystalline sample for uniaxial compression testing: the left graphics show the FE mesh containing 168 grains and 18,814 tetrahedral elements; the right image shows a (0001)-pole figure of the initial grain orientation distribution used in simulations.

7.1.2 Taylor model results

As discussed in Chapter 6, Taylor model assumes that each grain undergoes the same total deformation; it provides an upper bound on the stress-strain relation and has traditionally been used in texture calculations. For a brief review, the total energy is assumed to be

$$W(\boldsymbol{F}) = \frac{1}{n_{\mathrm{g}}} \sum_{i=1}^{n_{\mathrm{g}}} W(\boldsymbol{R}_i \boldsymbol{F}), \tag{7.1}$$

for a polycrystal containing n_{g} grains with orientations defined by rotation tensors $\boldsymbol{R}_i \in SO(3)$.

To mimic the uniaxial compression test using the relaxed Taylor model discussed in Chapter 6, we impose a velocity gradient of the type

$$\boldsymbol{l} = \begin{bmatrix} l_{11} & l_{12} & l_{13} \\ l_{21} & l_{22} & l_{23} \\ 0 & 0 & \dot{\varepsilon} \end{bmatrix}, \tag{7.2}$$

where the loading is in the 3-direction and characterized by loading rate $\dot{\varepsilon}$. The unknown deformation in the 1 and 2-direction (i.e., all shown l_{ij} components) is found by imposing traction-free

boundary conditions.

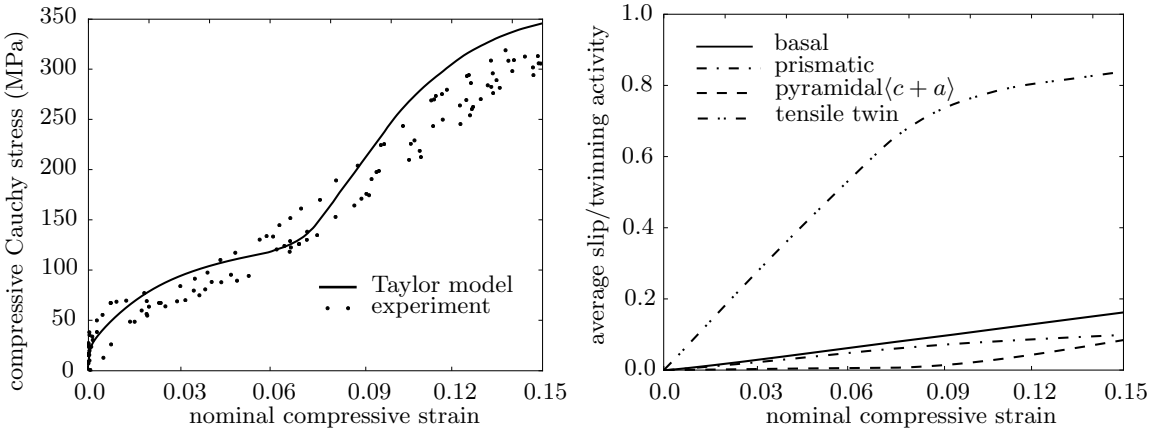

Figure 7.5: Stress-strain response obtained from the Taylor model and compared to experimental data of Dixit et al. (2015).

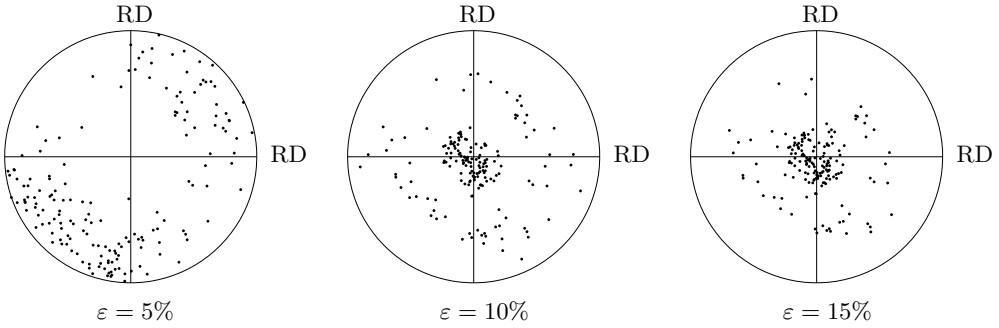

Figure 7.6: Texture evolution during uniaxial compression showing that twinning reorients the (0001)-poles to align with the ED.

The stress-strain response from the Taylor model is shown in Figure 7.5 along with the experimental stress-strain data of Dixit et al. (2015). In both simulation and experiment we see the characteristic two stages of the stress-strain response, which is also reflected by the average slip/twin activity plot also included in Figure 7.5: at low strains, the c-axes of most grains are perpendicular to the loading direction (ED), so that tensile twins are active. At about 9% compression strain, twinning is complete and most c-axes have been reoriented towards the loading direction. This is confirmed by Figure 7.6, which shows the texture evolution in terms of (0001)-pole figures. From the average activity plot in Figure 7.5 we further infer that about 80% of all grains are twinning-dominated (the average twinned volume fraction is about 0.8 at the end of the

simulation).

It is important to note that we do not fit any material parameters to the experiments of Dixit et al. (2015); all material parameters were obtained a-priori from single-crystal experiments, see Chang and Kochmann (2015). The only experimental input here is the EBSD grain distribution data. It is quite remarkable that the rate-dependent crystal plasticity model that was calibrated by comparison to low-rate experiments captures well the high-strain-rate response of the Kolsky bar experiment (on the order of $10^3 s^{-1}$). Of course, the match between experiment and simulation is not perfect, which may be attributed to a number of potential error sources. For example, the EBSD map stems from the specimen surface, no measurements from within the sample are available. Furthermore, the uniform-deformation assumption of the Taylor model is known to over-predict stresses (indeed, simulated stresses are higher than experimental data).

7.1.3 Finite element results

As in previous section, we simulate uniaxial compression of extruded pure Mg, this time using the finite element model of Figure 7.4. The polycrystalline pillar is compressed axially (i.e., in its ED) up to a compressive strain of 15%. The resulting stress-strain curve and the associated average slip/twin activity over all quadrature points in the model are shown in Figure 7.8. In addition, the slip and twin mechanisms are highlighted in Figure 7.7 at compressive strains of $\varepsilon = 2.5\%$, 5.0%, 7.5%, and 10% (twinning is already complete near 10% so that further plots do not show interesting changes in behavior).

FE results are qualitatively similar to those obtained from the Taylor model. The typical two-stage stress-strain behavior is characterized by the completion of twinning before 8% (affecting about 80% of all grains). As expected, the stress level is lower than in Figure 7.5. We note that the small number of grains and the large surface area in the FE model provide stress relaxation mechanisms that may contribute to an artificial reduction of the simulated stress response. Figure 7.7 highlights the large amount of twinning inside the pillar during compression, and most grains complete twinning before 10% compression. Besides tensile twinning, basal slip is the dominant inelastic deformation mode because of its lower activation stress. After the completion of twinning, the misalignment of the (0001)-poles with the loading direction gives rise to the observed stress increase.

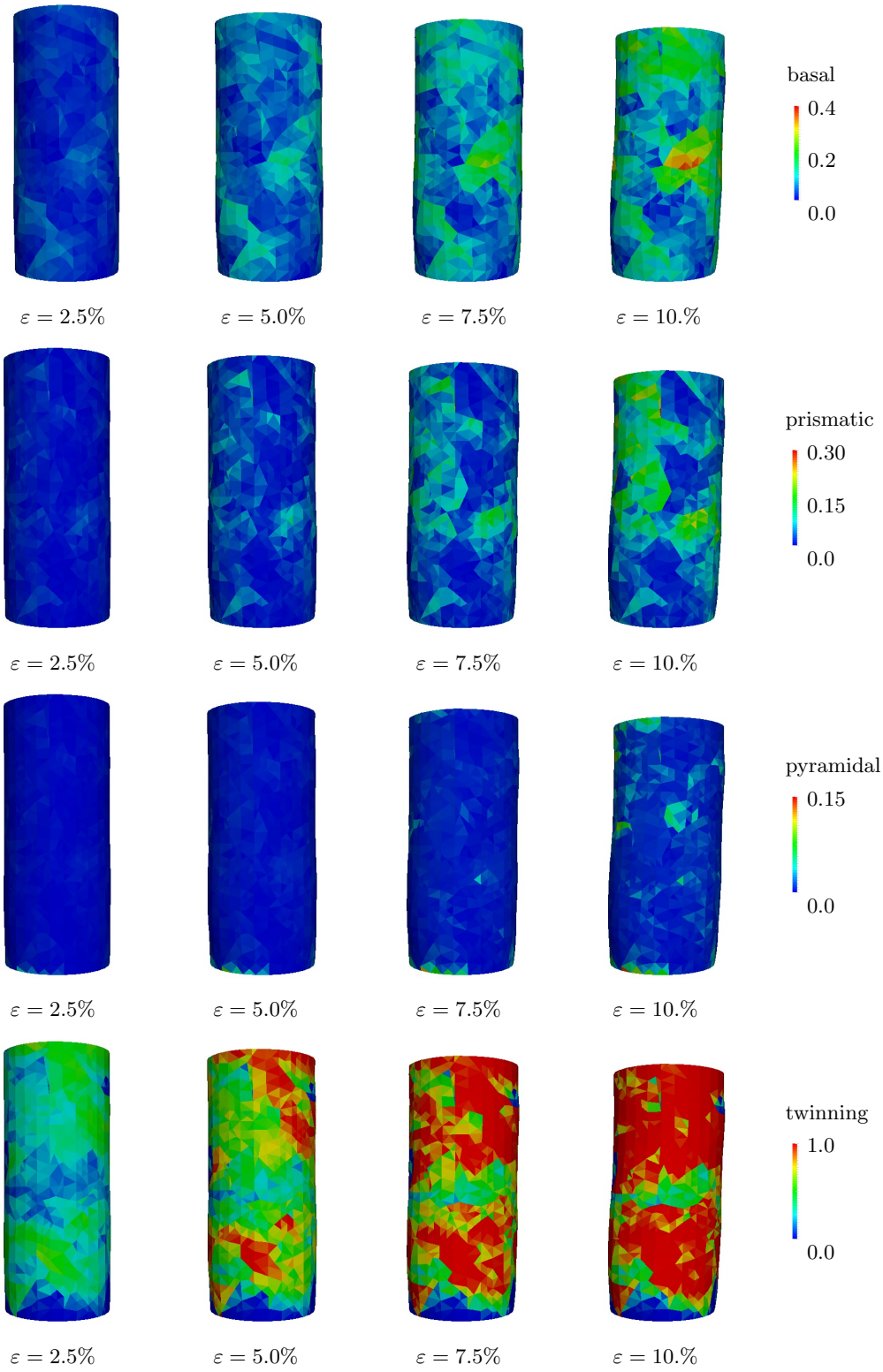

Figure 7.7: Microstructural evolution during unixial compression simulation of extruded Mg polycrystal depicted in terms of slip/twinning on different systems.

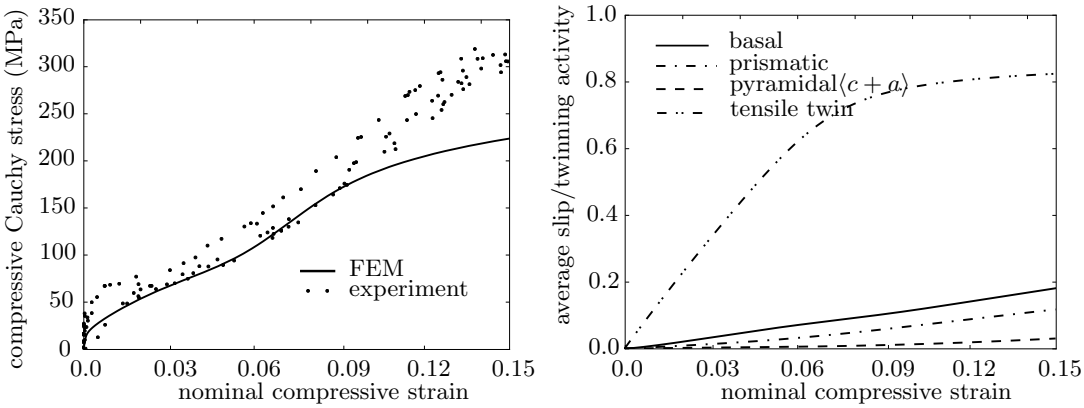

Figure 7.8: Stress-strain response from an FE simulation compared to experimental data of Dixit et al. (2015).

7.1.4 Comparing to an efficient Mg material model

A computationally efficient model for hcp crystals was developed by Becker and Lloyd (2015). The goal for this efficient crystal plasticity model is to retain several essential behaviors of the underlying crystal plasticity mechanism while introducing approximations that reduce computational complexity. Similarly to our model, twinning is captured through the average volume fraction (twinning ratio) and incorporated as an additional slip system. The efficiency is obtained through the following approximations: the specific slip direction on the basal system is given secondary importance and therefore basal slip is represented by a single slip whose direction is determined from the maximum resolved shear stress inside the basal plane; prismatic and pyramidal slips are combined as an isotropic function and approximated by the J2 flow theory. The hardening of twin systems is modeled by assigning different hardening laws to different twin stages as in Graff et al. (2007). In particular, the reorientation of the lattice structure due to twinning is not explicitly included and is only captured during post processing; thus the activation of multiple twin systems is allowed and does not create additional numerical difficulties, such as those discussed in Section 3.2.

Uniaxial compression simulations of extruded Mg polycrystals are run using the finite element method with 168 grains and 16,800 hexagonal elements by our ARL collaboraters, but this time with the efficient crystal plasticity model. Results are summarized in Figure 7.9 through Figure 7.11. Since the model does not explicitly include prismatic and pyramidal slip systems, the effects of those two systems are captured by the effective plastic strain due to non-basal slip ϵ_{eff}. Figure 7.9

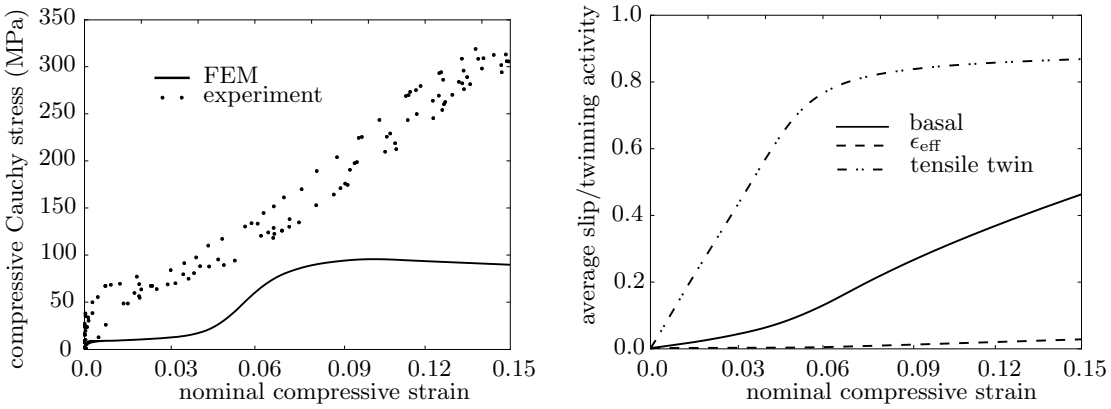

Figure 7.9: Stress-strain response from an FE simulation compared to experimental data of Dixit et al. (2015). Simulation results were obtained using the efficient crystal plasticity model of Becker and Lloyd (2015).

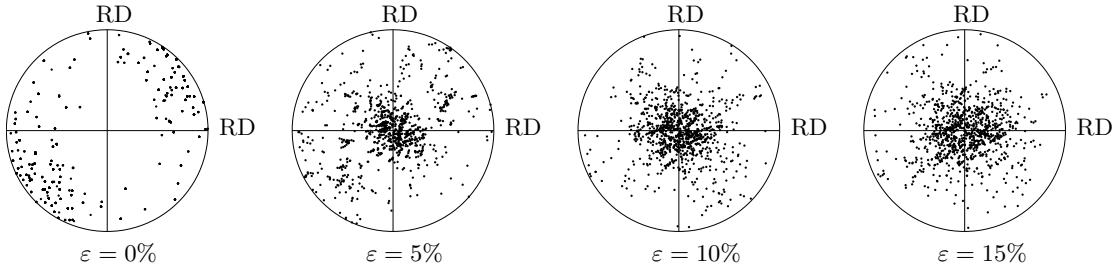

Figure 7.10: Texture evolution during uniaxial compression showing that twinning reorients the (0001)-poles to align with the ED. Simulation results were obtained using the efficient crystal plasticity model of Becker and Lloyd (2015).

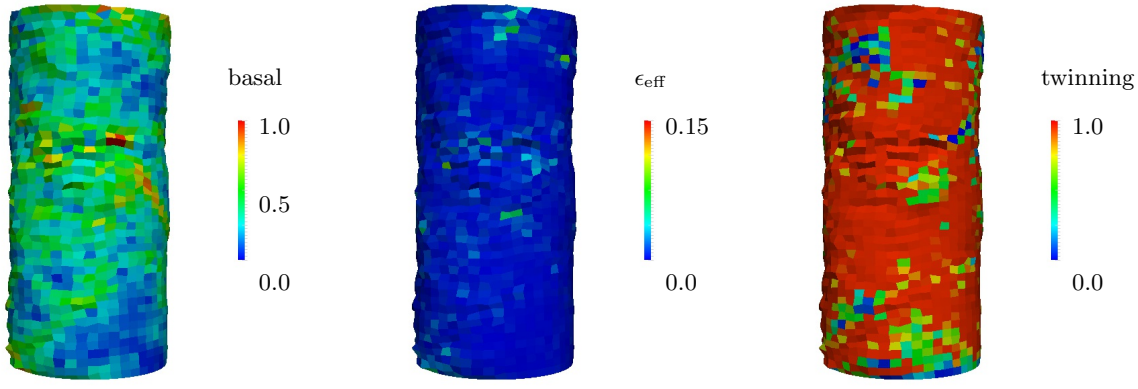

Figure 7.11: Slip and twin activity at 10% compressive strain during uniaxial compression of an extruded Mg polycrystal depicted in terms of slip/twinning on different systems. Simulation results were obtained using the efficient crystal plasticity model of Becker and Lloyd (2015).

shows the resulting stress-strain curve with the same experimental data from Dixit et al. (2015), and the average slip/twin activity is plotted on the right. Similarly to our simulations, we see a two-stage S-shaped response predicted by this model, indicating a twinning-dominated deformation at an early stage. In addition, we see the average twinning ratio reaches more than 0.80 towards the end of the simulation, meaning that more than 80% of the grains are dominated by twinning. However, in these plots, the stress level is lower than both experimental data and that predicted by our model, which can be explained by the non-reorientation scheme that was employed, allowing for improved efficiency: after twinning completes, the basal poles are reorientated to align with the ED. However, this reorientation is not taken into account in the subsequent calculations, which makes basal slip remain at a comparatively lower activation. Thus, we see the stress stays at a relatively lower level due to the significant amount of basal activation. This can also be demonstrated by the average basal slip activity plot on the right of Figure 7.9, where the efficient model predicts more than double the basal activity seen in our model.

Figure 7.10 reports the (0001)-pole figure during the simulation. Since the model does not account for the determination of the lattice frame in the twinned orientation, the activation of multiple twinning systems is allowed so that we do not need to worry about the reorientation rule to deal with more than one twin reflections. The lattice reorientation is captured in the post-processing. Because of the heterogeneity in each grain, i.e., each element has its unique orientation, 1000 orientations from the mesh are randomly picked to generate the plots. In this figure, the majority of basal poles reorient towards the ED by the activation of the tensile twin systems and we see most grains finish reorientation before 5% strain, which is earlier than what our model predicts. This is due to the late reorientation rule our model imposes: we consider the lattice to be reoriented only when the twinning ratio is greater than 0.8. In Figure 7.11, the microstructures at 10% strain are depicted by different slip/twin activities, where we see a significant amount of basal slip and twinning for reasons explained before.

7.2 Uniaxial compression of cold-rolled Mg polycrystal

In the previous section, extruded Mg polycrystals were loaded in the ED, so the plastic deformation was dominated by tensile twinning (the loading direction exposed the c-axis of most grains to tensile loading). In this section, we use the same computational techniques to study the response of cold-

rolled pure Mg.

7.2.1 Taylor model and finite element study of uniaxial compression of cold-rolled Mg polycrystal

Compared with the extrusion process, cold rolling is a more common metal-forming process that results in more pronounced texture characteristics. Both experiments (Sandlöbes et al., 2011) and our simulations in Section 6.3.1 have shown that basal poles are spread around the rolling normal directions (ND) after the process. Here, we take rolled Mg polycrystals and perform uniaxial compression in the ND and TD and observe the resulting material behavior (undergoing both twinning and non-twinning dominated deformation). As before we employ both a Taylor model with deformation gradient (7.2) and the finite element representation of Figure 7.13. The Taylor model uses a polycrystal consisting of 1000 grains, while the finite element simulations are performed separately with pillars containing 100 and 1000 grains. The 100-grain pillar has $67,815$ tetrahedral elements, and the $1,000$-grain pillar has $107,131$ tetrahedral elements. We assume that each grain corresponds to one orientation in the shown pole figure (Figure 7.12) exported from EBSD characterization. As is clearly visible, the polycrystal exhibits strong texture with the (0001)-poles clustered near the ND. In the simulation, we compress the sample in both the ND and TD at a low strain rate of $\dot{\varepsilon} = 10^{-3}\mathrm{s}^{-1}$ up to a compressive strain of 10%.

The stress-strain curve and the texture evolution in terms of (0001)-pole figures for TD and ND compression are shown in Figures 7.14 and 7.15, respectively. As expected, the stress levels obtained the from the Taylor model are higher in both simulations than those from FEM because of the relaxation between grains and the free surface effects as discussed in Section 7.1.3, which can also explain the higher stress level predicted in the 1000-grain FE simulation compared to the 100-grain FE simulation. The microstructural evolution is visualized in Figures 7.16 to 7.19, which illustrate the different slip and twin system activities.

In Figures 7.14, 7.18 and 7.16, the polycrystal is compressed in the TD, leaving the normal direction in tension. Similarly to the experimental results in Section 7.1, twinning dominates the early stages of deformation in most grains. The stress-strain response exhibits the typical two stages denoting the change in primary inelastic mechanisms after the completion of twinning. In Figure 7.16 and 7.18, we observe large numbers of grains being completely twinned at the end of

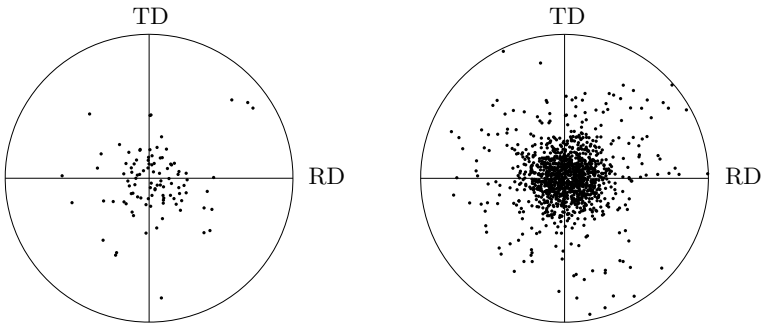

Figure 7.12: The (0001)-pole figure of rolled Mg polycrystals consisting of 100 and 1000 grains used in finite element and the Taylor model simulations.

100 grains 1000 grains

Figure 7.13: FE representation of the rolled polycrystalline sample: the left FE mesh contains 100 grains and $67,815$ tetrahedral elements; while the right mesh contains $1,000$ grains and $107,131$ tetrahedral elements.

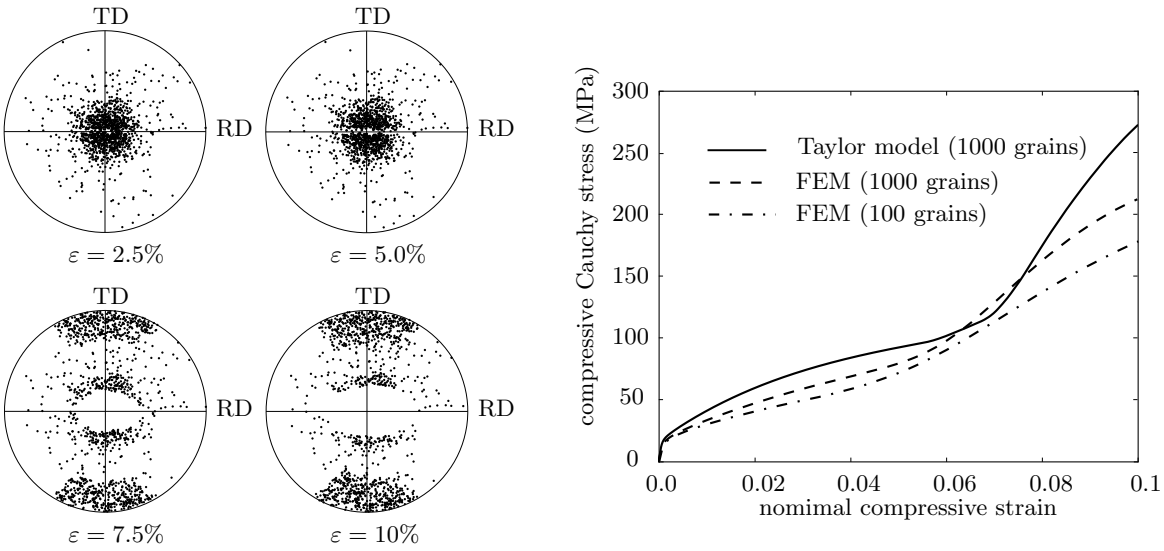

Figure 7.14: Texture evolution in terms of (0001)-pole figures and stress-strain response for the cold-rolled Mg polycrystal being compressed in the TD: the stress-strain response shows the typical two stages because of grain reorientation due to twinning.

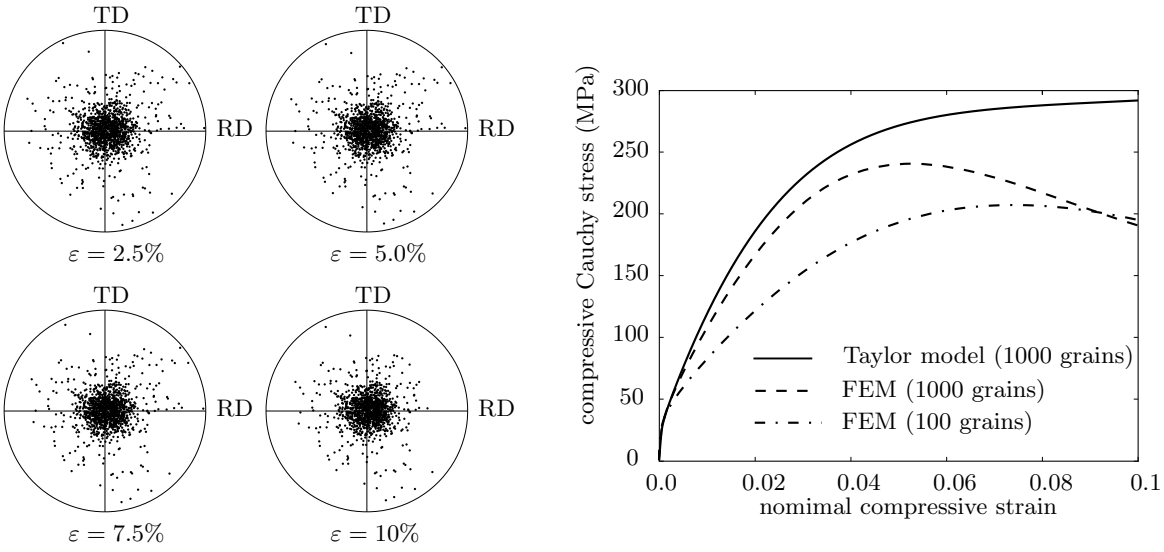

Figure 7.15: Texture evolution in terms of (0001)-pole figures and stress-strain response for the cold-rolled Mg polycrystal being compressed in the ND: texture reorientation is not observed because the tensile twin systems are suppressed.

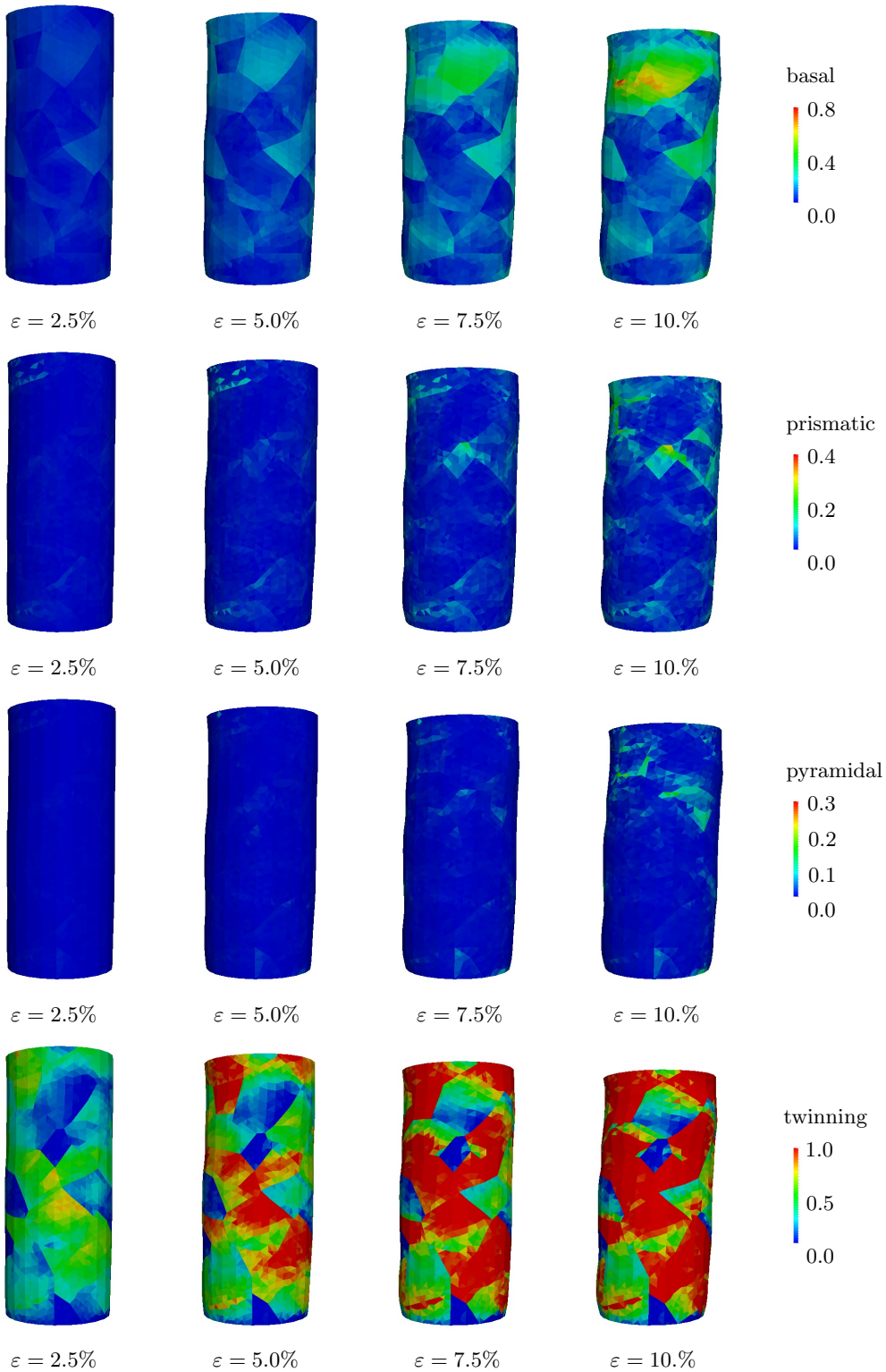

Figure 7.16: Microstructural evolution during uniaxial compression of a rolled 100-grain Mg polycrystal in the TD, visualized in terms of slip and twin system activities.

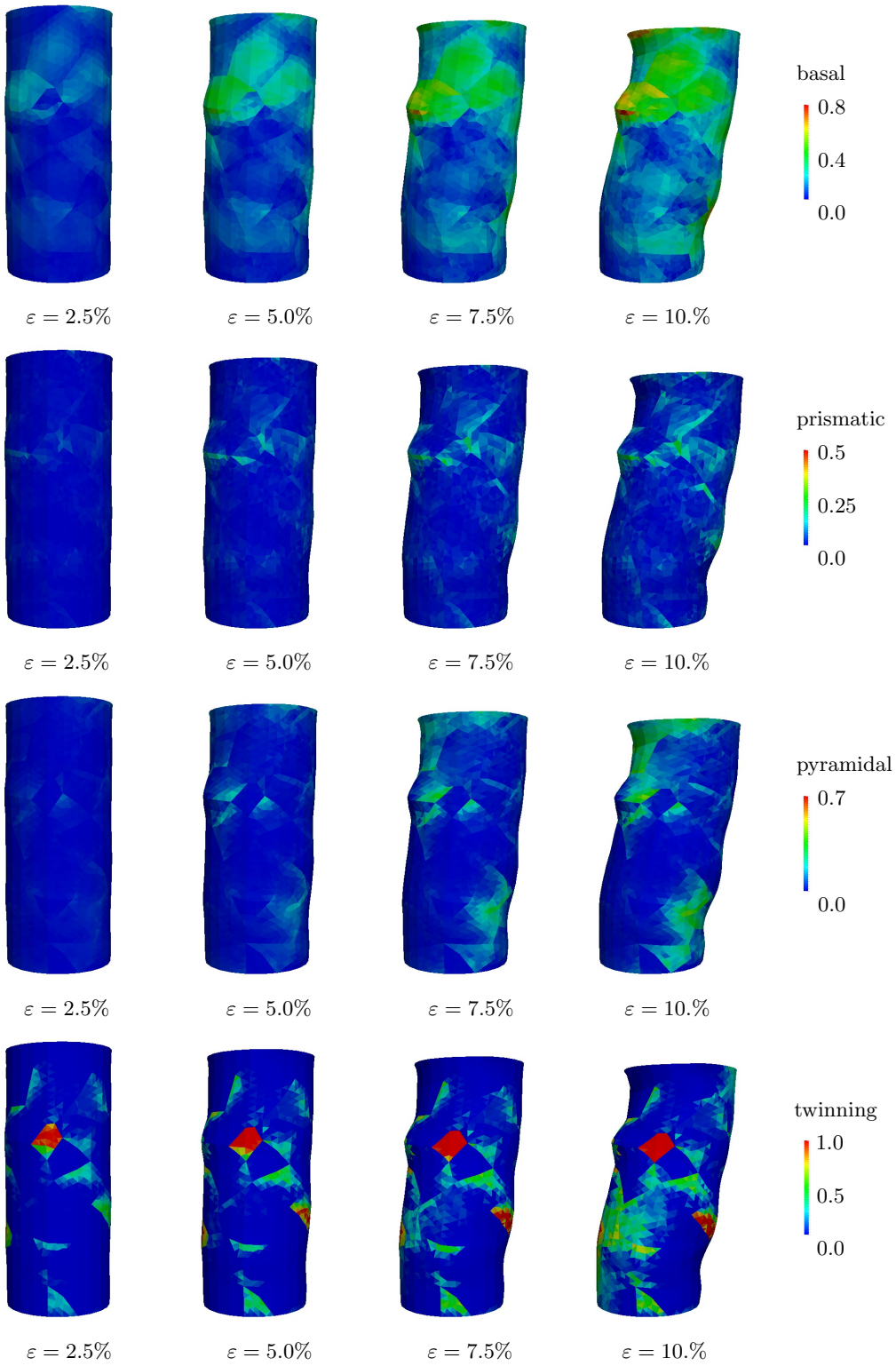

Figure 7.17: Microstructural evolution during uniaxial compression of a rolled 100-grain Mg polycrystal in the ND, visualized in terms of slip and twin system activities.

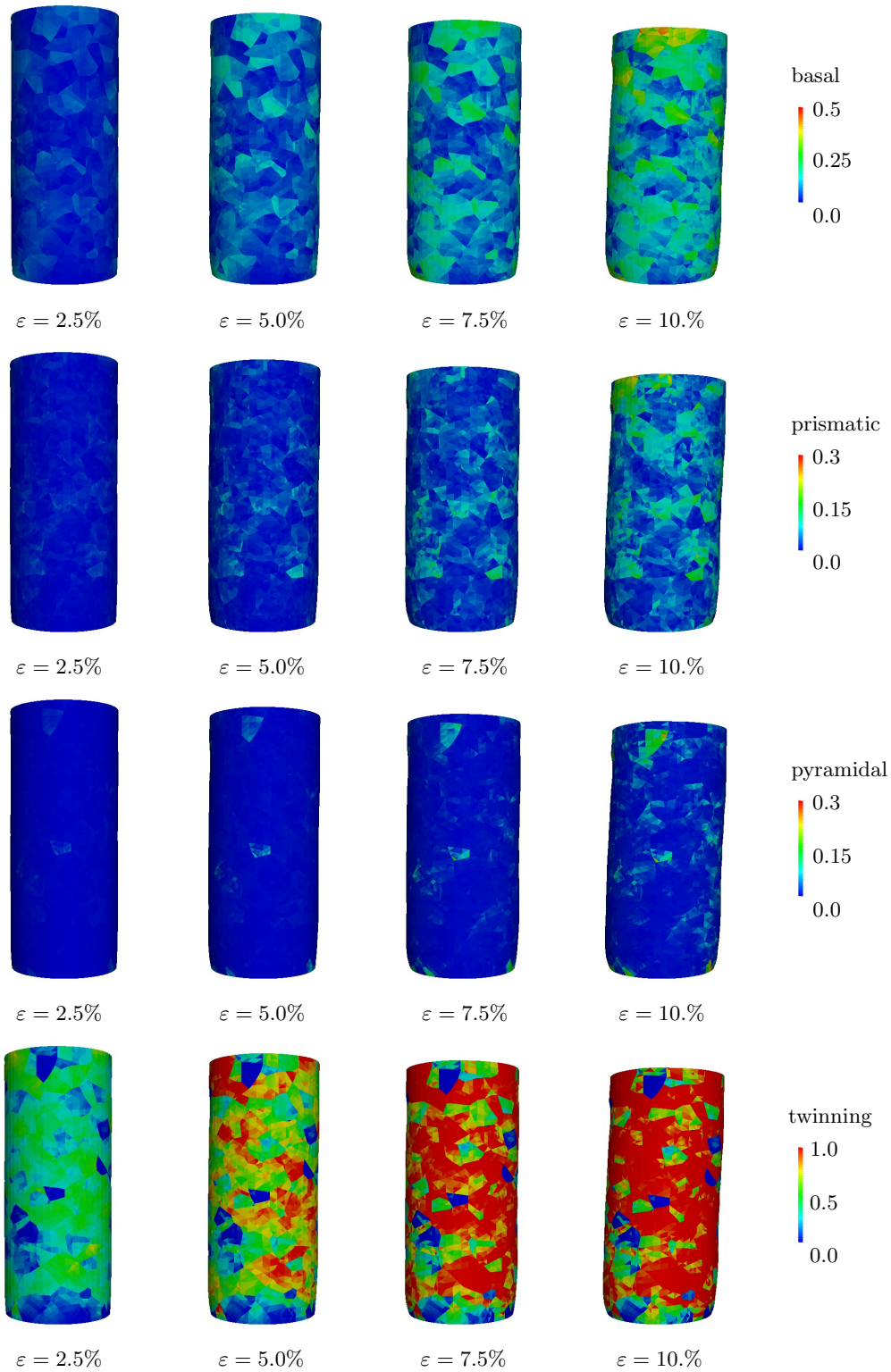

Figure 7.18: Microstructural evolution during uniaxial compression of a rolled 1000-grain Mg polycrystal in the TD, visualized in terms of slip and twin system activities.

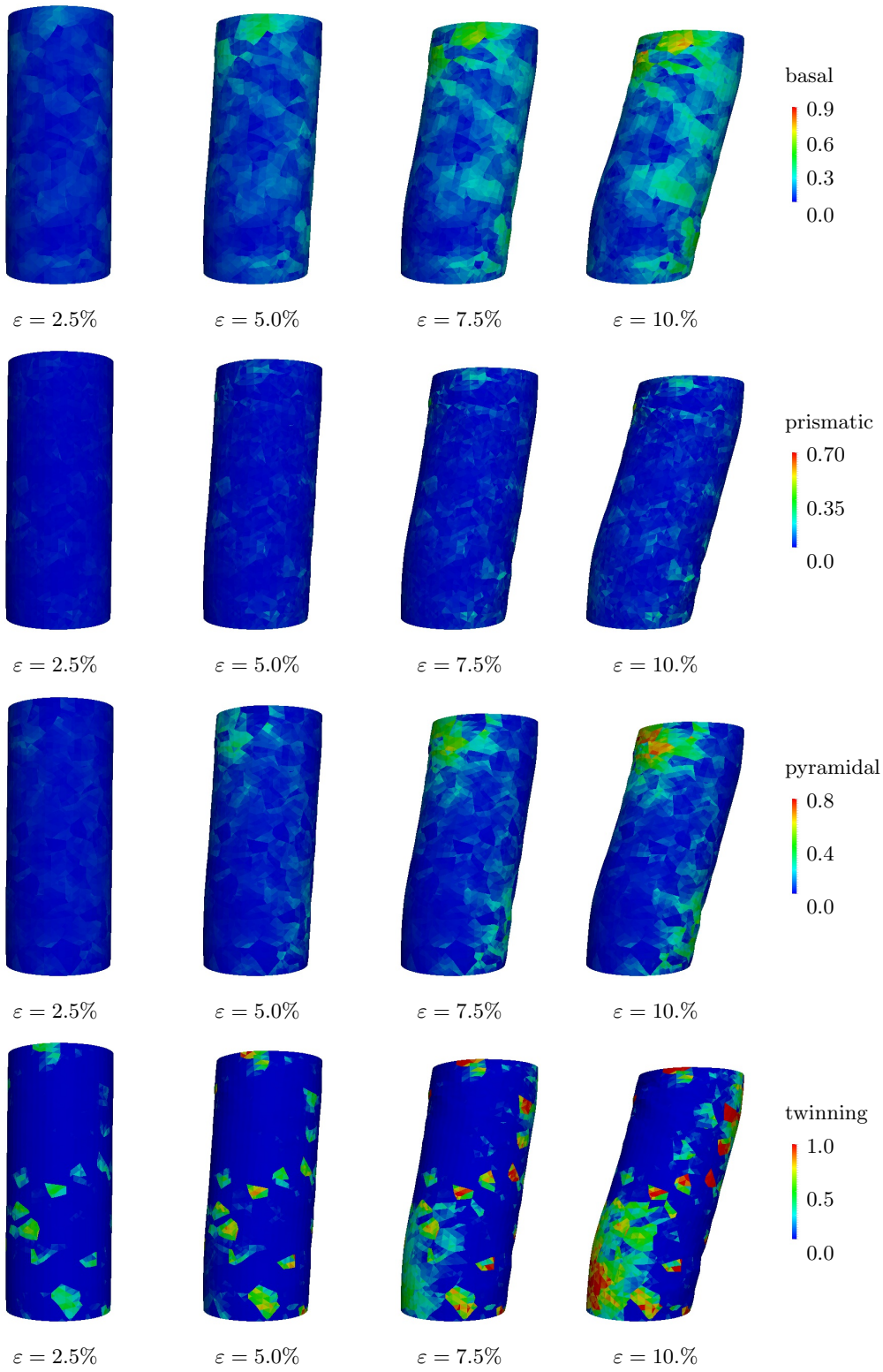

Figure 7.19: Microstructural evolution during uniaxial compression of a rolled 1000-grain Mg polycrystal in the ND, visualized in terms of slip and twin system activities.

the simulation. After the completion of twinning, the twinning-dominated grains are reoriented about the twinning plane (see the pole figure in Figure 7.14), leading to the shown stress increase due to small misalignments of the basal poles with the loading direction.

In Figures 7.15, 7.17 and 7.19, the polycrystal is compressed in the ND. In this case, most of the c-axes of the grains are spread around the compression direction, which is not in the twin-favored orientation. Therefore, during the early stages of deformation ($\varepsilon < 5\%$), we observe twinning only in a small number of grains. By contrast, the amount of slip across all slip systems is larger than that in the previous, twinning-dominated case. This is reasonable since twinning contributes little to the plastic deformation, which is accommodated mostly by slip in this case. We emphasize the stress decrease in the FE 1000-grain simulation of Figure 7.15 after about 5% of compressive strain, which can be explained by the extension twin activity in the bottom left and upper right corners of the pillar in Figure 7.19. Although the overall state of the pillar is in compression, during deformation some parts of the pillar are in tension because of the significantly deformed shape caused by the slip activity and the fixed boundary condition at the bottom. Those jointly lead to the activation of tensile twins at very large deformation. Since the activation stress for twins is lower than slip (in this case the basal slip direction is very close to the loading direction, and thus its activation stress is higher than twinning), we see the stress decrease as twinning is activated. This phenomenon is not observed in the Taylor model simulation, which does not admit local stress relaxation as in the FE model.

7.2.2 Comparison with the efficient material model

Similar to Section 7.1.4, a comparison study of uniaxial compression of rolled Mg polycrystals with the efficient crystal plasticity model of Becker and Lloyd (2015) is summarized in this section. A 1000-grain pillar of similar structure with $134,400$ hexagonal elements is compressed in the TD and ND using the efficient crystal plasticity model and results are summarized in Figure 7.20 through Figure 7.23.

As shown in Figure 7.20, compression along the TD shows an S-shaped curve because of the twinning dominance. However, the stress level is lower than the stress our models predicts and does not show significant strain hardening. As we discussed before, the reason is the efficient model does not account for slip system reorientation in the subsequent calculation, and thus the deformation is mostly accommodated by the easily activated basal slip, whose stored energy does not exhibit

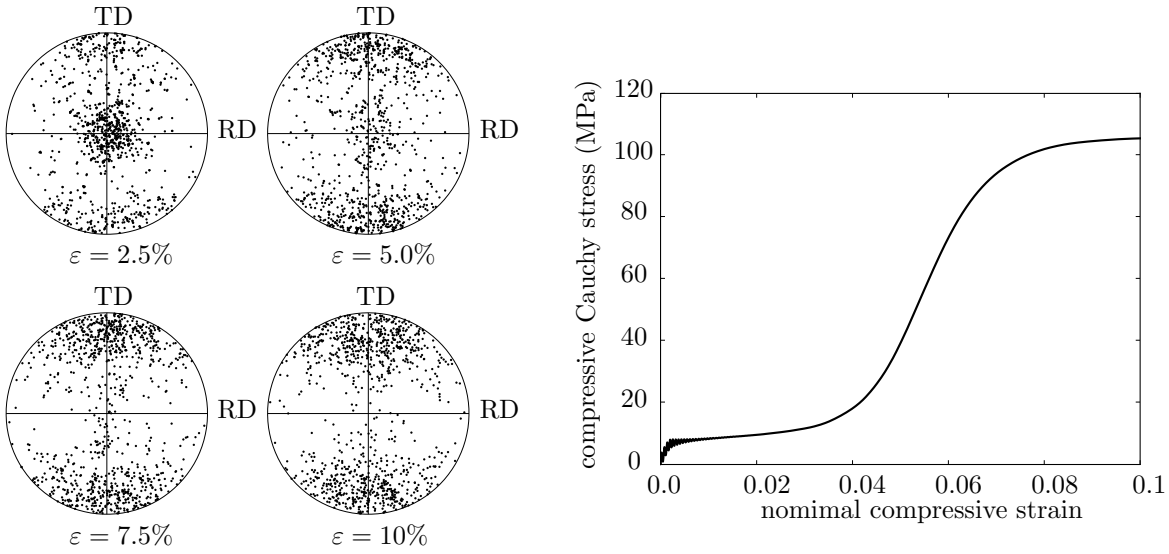

Figure 7.20: Texture evolution in terms of (0001)-pole figures and stress-strain response for the cold-rolled Mg polycrystal being compressed in the TD: the stress-strain response shows the typical two stages because of twinning activation. Simulation results were obtained using the efficient crystal plasticity model of Becker and Lloyd (2015)

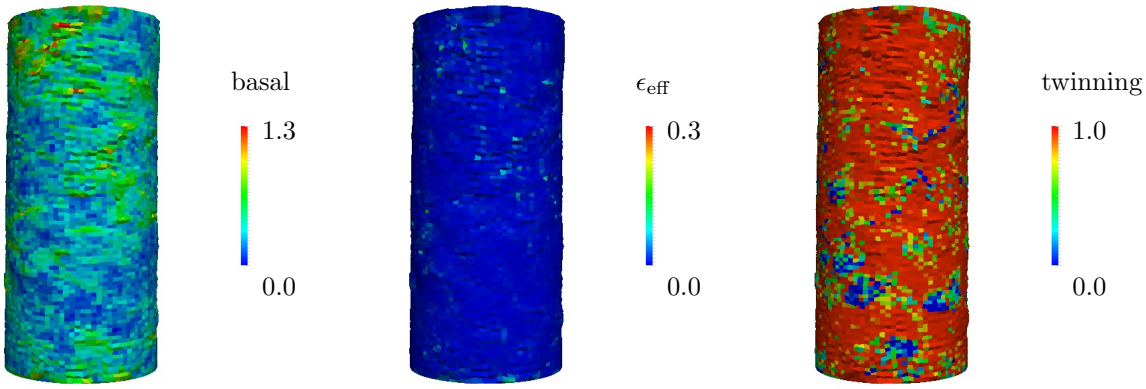

Figure 7.21: Microstructure at 10% compressive strain during uniaxial compression of rolled Mg polycrystal in the TD, visualized in terms of slip/twinning systems activities. Simulation results were obtained using the efficient crystal plasticity model of Becker and Lloyd (2015).

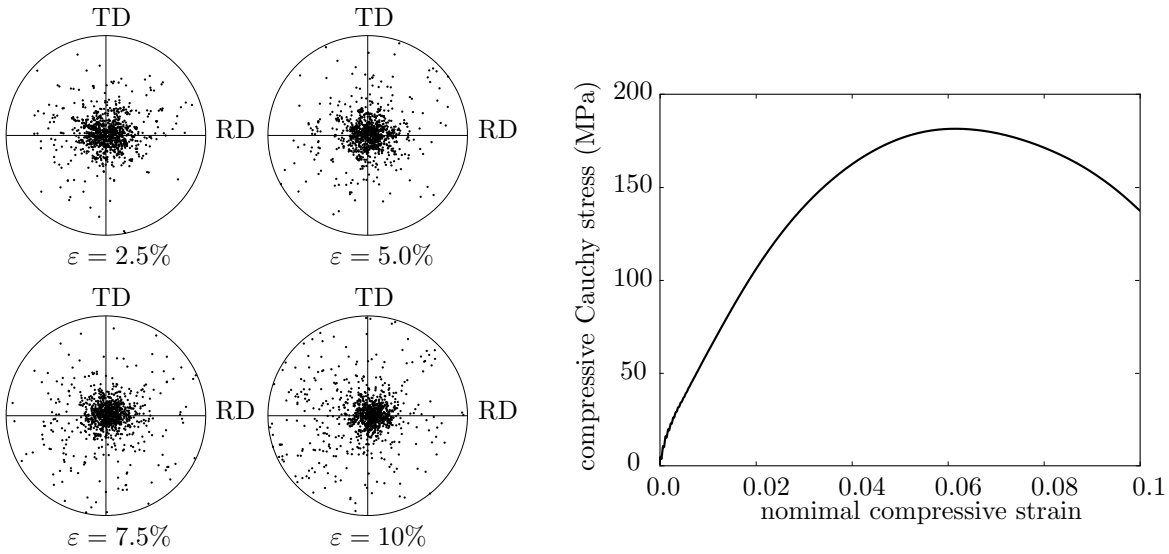

Figure 7.22: Texture evolution in terms of (0001)-pole figures and stress-strain response for the cold-rolled Mg polycrystal being compressed in the ND: texture reorientation is not observed because the tensile twin systems are suppressed. Simulation results were obtained using the efficient crystal plasticity model of Becker and Lloyd (2015).

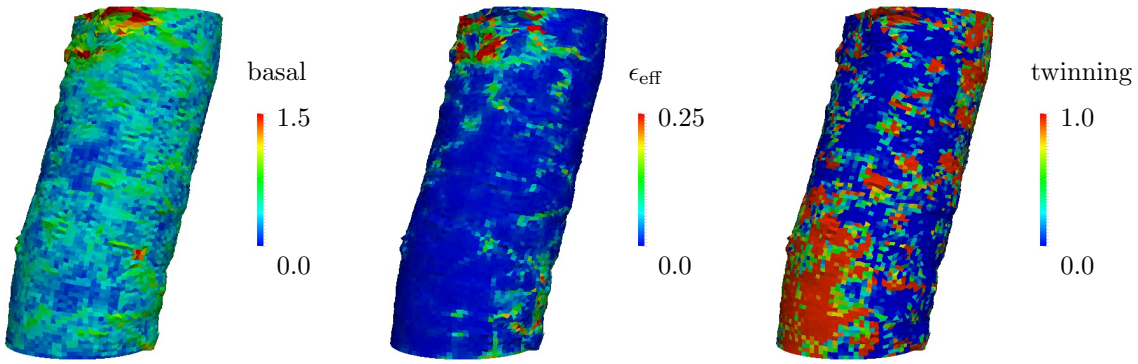

Figure 7.23: Microstructure at 10% compressive strain during uniaxial compression of rolled Mg polycrystal in the ND, visualized in terms of slip/twinning systems activities. Simulation results were obtained using the efficient crystal plasticity model of Becker and Lloyd (2015).

strong hardening behavior. The (0001)-pole figure is plotted by randomly populating 1000 grain orientations from all elements, which shows the reorientation of basal poles toward the loading direction (TD). Figure 7.21 depicts the slip/twin contour plot with 10% strain, where we see a significant amount of twinning and basal slip occurring inside the pillar.

Compression along the ND shows a similar behavior in both of the two models. A non-twinning-dominated deformation is predicted by both models and the resulting texture does not exhibit any reorientation as shown in Figure 7.22. In addition, the stress-strain responses are more similar in both stress level and curve shape. The slightly higher stress level predicted by our model might be due to the inclusion of the pyramidal slip system, which typically has a higher level of activation stresses and the deformation from the efficient model is mainly due to the misalignment of basal slip to the loading direction. In addition, both models predict a stress softening after about 5% of strain, which is explained by the late activation of the tensile twin system at the bottom left and upper right part of the pillar.

7.2.3 Rate dependency study

The irreversibility and rate dependency are modeled through the inclusion of dissipation potentials (3.35) and (3.36). As pointed out in Section 3.3.3, the rate sensitivity of twinning is very low (Ulacia et al., 2010).Thus the dissipation potential is assumed to be zero. The form of the slip dissipation potentials is taken as a power law, which is commonly used in crystal plasticity, see e.g.. (Ortiz and Stainier, 1999), and the dissipation parameters shown in Table 5.1 are taken from a micropillar nickel compression study (Hurtado and Ortiz, 2012) because of the lack of experimental data on Mg.

We perform the same uniaxial compression tests as in Section 7.2.1 of the cold-rolled Mg polycrystal with different strain rates ($\dot{\varepsilon} = 10^{-4}, 10^{0}, 10^{3}$ and $10^{5}\mathrm{s}^{-1}$) via the Taylor model. The compression is carried out in both the TD and ND for twinning and non-twinning-dominated deformations. The stress-strain responses are summarized in Figure 7.24 and Figure 7.25. In both figures, we see a similar shape of the stress-strain curves for all the strain rates as in Section 7.2.1, i.e., compression along the TD shows a two-stage deformation indicating a twinning-dominant deformation followed by basal/pyramidal slip activity, while compression along the ND shows a non-twinning-dominated deformation. Furthermore, we see a typical rate dependency in both simulations, i.e., the stress increases as we increase the strain rate, which shows our modeling capability to capture

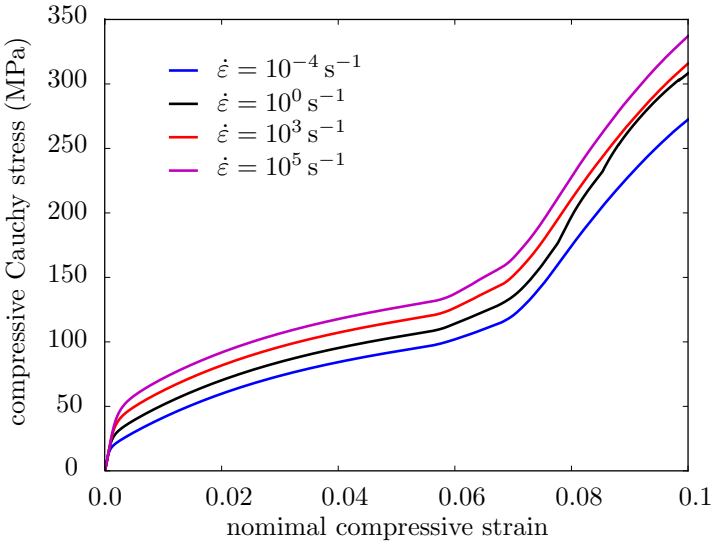

Figure 7.24: Stress-strain response of the uniaxial compression of a rolled Mg polycrystal in the TD at different strain rates.

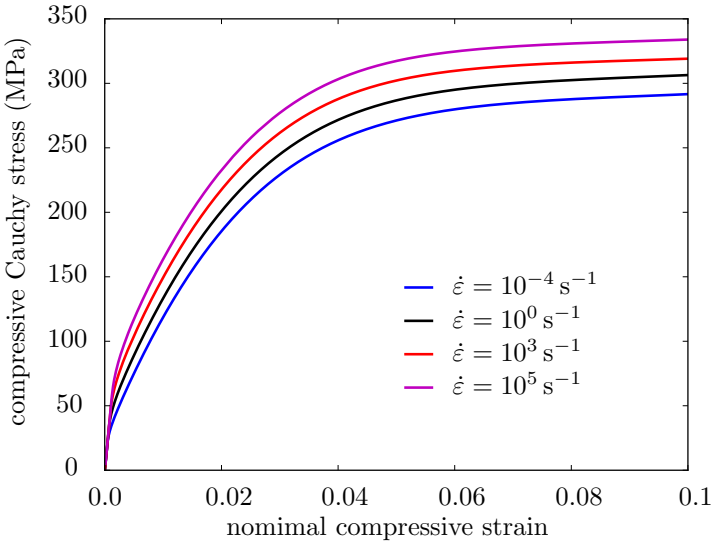

Figure 7.25: Stress-strain response of the uniaxial compression of a rolled Mg polycrystal in the ND at different strain rates.

the rate sensitivity of Mg, at least qualitatively. Since the rate dependency of twinning is assumed to be small and not captured by the dissipation potential, the observed rate-dependent hardening is due to the rate sensitivity of the slip systems. Finally, we mention that, at this point, we do not fit any parameters related to the rate dependency of Mg polycrystals, especially of the rate sensitivity of twinning. The results may not represent the exact behavior of Mg polycrystals. In order to develop a more comprehensive model to capture the rate sensitivity, more evidence from experiments is required, especially on Mg single crystals.

Chapter 8

Concluding Remarks

8.1 Summary

In this thesis, we have reported an efficient continuum framework to describe the effective mechanical response of hcp metals and particularly of pure Mg single- and polycrystals, whose inelastic performance is governed by the interplay of slip and twinning deformation mechanisms. Our model follows the internal variable approach and employs an extended crystal plasticity model to include twinning as additional slip systems. The interaction of slip and twinning and the associated lattice reorientations are modeled by the introduction of a specific flow rule. By employing the concept of twinning ratios, we capture the average twinning response at the lower scale level, but build an efficient model on the higher scale. Following the variational approach, we assign different hardening behaviors to basal, pyramidal, and prismatic slip as well as to the tensile twin systems by choice of different plastic stored energies. The rate sensitivity is treated differently for slip and twinning: slip is regarded as an irreversible process and dissipation potentials are assigned to each slip systems. The dissipation of twinning is assumed to be vanishingly small since twinning shows very low rate sensitivity, as discussed in Section 3.3. The elastic anisotropy of the hcp crystal structure can be included by a polyconvex strain energy density.

The model has been studied and validated by a series of numerical experiments. Nanoindentation simulations on calcite and sapphire have produced resulting twin shapes to be in agreement with experimental observations and phase field calculations (Clayton and Knap, 2011b). Simple shear/compression examples with single slip and single twin systems explicitly show slip-twinning interactions and lattice reorientation. Material parameters are determined by a direct comparison

to experimental data for single- and polycrystalline Mg, showing good quantitative and qualitative agreement and superior efficiency compared to modeling approaches based on explicit updates of the internal variables. The model was utilized for simulating the cold-rolling process, during which we predict texture and yield surface evolution. Our simulation shows good agreement with experimental observations. Finally, we apply our model to run large-scale simulations of textured Mg polycrystals using both a Taylor model and the finite element method. We perform uniaxial compression tests on extruded and cold-rolled Mg polycrystals and compare our results to experimental data from Dixit et al. (2015). Both Taylor model and finite element simulation give good qualitative and quantitative prediction of the material behavior; the two-stage S-shape stress-strain response agrees particularly well with experiments when the deformation is twinning-dominated. The Taylor model is efficient when modeling a large number of grains but tends to omit the detailed interactions at the grain boundaries. In contrast, by using finite element simulation, we model detailed microstructural evolution and deformation inside each grain, but at the expense of the higher computational cost as discussed in Chapter 7. Finally, a rate sensitivity study shows that the model captures the rate-dependent behavior because of the slip dissipation potential introduced in Chapter 3.

Owing to its variational structure, the presented model allows for various extensions. As discussed in Section 7.2.3, rate dependency is built into the model through dissipation potentials and we have predicted the stress hardening with increasing loading rate. However, because of the lack of experimental data on pure Mg single crystals, our choice was based on the dissipation of fcc metals. With the input of plausible experimental data, we can extend our model to make quantitatively more accurate and reliable predictions across various strain rates.

Of course, like every macroscopic continuum model, the presented approach is based on a number of simplified assumptions which greatly affect the balance between accuracy and efficiency. As pointed out in Section 3.1, the current model does not allow two or more twinning variants to be activated at the same time because of the complexity it would create on the lattice reorientation rule. This assumption works well in finite element simulations because each grain can activate several twinning systems, one at each different Gauss point. However, it is questionable to enforce this condition in Taylor model simulation since each material point is treated as a grain. Thus, a more comprehensive reorientation rule needs to be developed by understanding not only the slip-twin interactions but also the twin-twin interactions when multiple twinning variants are active. The

model of Zhang and Joshi (2012) does account for complicated twin-twin and twin-slip interactions, yet it does not admit a variational formulation and is therefore rather inefficient, since it requires very small load increments and does not ensure numerical stability. Furthermore, the use of the effective twinning ratio provides an efficient way to incorporate information from the lower scale; however, it lacks the capability to capture the detailed interactions between slip and twinning, e.g., twin nucleation and evolution, or effects of dislocation pile-up as discussed in Section 1.2. Thus, further model refinement possibly with the incorporation of the presented phase field model is a possible future step.

8.2 Future directions

Looking into the future, there are a number of possible directions to be explored based on the models and results presented in this thesis:

Besides the rate dependency we have discussed in Section 7.2.3, some other extensions can be readily made by feeding proper experimental data. First, our model parameters are fitted to experiments on pure Mg single crystal. However, the model we presented is developed for any general material where slip and twinning are two competing deformation mechanisms. As we show in Section 5.1, our model gives reasonable predictions on the twin shape of calcite and sapphire under nanoindentation. We could easily extend our model to Mg alloys by supplying valid experimental data on the hardening behavior of different systems of Mg alloys, so that the required material parameters can be obtained from fitting and functional representations of hardening energies and dissipation potentials may be adjusted, where necessary. Second, in our simulation, the compression twin systems are not included because of their high critical resolved shear stress and large critical shear strain as discussed in Section 3.3. The recent study by Li et al. (2009) found the activation of compression twin during static recrystallization. Thus, further understanding of the competition between compression twins and the pyramidal $\langle c+a \rangle$ slip system is necessary for proposing appropriate hardening laws for the compression twin system and thus to include the complete set of twin systems into our model.

The ultimate goal of this research is to study the dynamic behavior of Mg under extreme dynamic environments, which involves the simulation of inertial effects and wave propagation. During wave propogation, materials experience tension and compression alternatively, and thus the cyclic

behavior of twinning must be understood. Generally speaking, the reversibility of the twinning process is explained by the reversible movement of twin boundaries. In cyclic loading, twinning and untwinning appear alternately. The unusual twinning behavior of pure magnesium or Mg alloys poses challenge to conventional constitutive models. Several models have been proposed (Hama and Takuda, 2011; Kondo et al., 2014; Proust et al., 2009), and are able to predict stress-strain responses under complex strain paths. The actual implementation will involve careful treatment of the lattice reorientation with unloading thus left as an open task for future study.

Currently, the hardening laws are constant functions for each slip/twin system. Like fcc or bcc metals, Mg and Mg alloys exhibit size effects (del Valle et al., 2006; Dobroň et al., 2011). Furthermore, Manabe and Shimomura (2006) found that the ultimate yield stress of Mg alloys is strongly influenced by temperature. Thus, including the various factors such as the characteristic size of grains, or the heat generation into the hardening law will be an interesting direction. Currently, we are in collaboration with Owen Kingstedt to study the thermal effects in rolled Mg polycrystals subjected to high rate shear compression experiments, which could help us to calibrate the relationship between temperature and hardening. Second, the stored energies we impose are emperical and material parameters that have been fitted to experimental data. A more comprehensive approach would be to obtain parameters from lower-scale approaches such as dislocation dynamics (Fan et al., 2015) or the quasicontinuum method (Amelang et al., 2015; Knap and Ortiz, 2001), which is anticipated to emerge from our collaborations within the MEDE Center.

Our current work involves understanding the failure process of Mg by the modeling of void growth. We employ a Gurson-type model (Gurson, 1977) and use a volumetric deformation gradient to characterize the state of damage, which will be included in our magnesium model in the future to give a complete description of the response of Mg and its alloy. Finally, experimental evidence, e.g., Foley et al. (2011), shows grain refinement during the typical ECAE process. Thus, including the recrystallization into our continuum model is another interesting direction to pursue.

Bibliography

Agnew, S. R., Brown, D. W., Tomé, C. N., 2006. Validating a polycrystal model for the elastoplastic response of magnesium alloy AZ31 using in situ neutron diffraction. Acta Materialia 54 (18), 4841 – 4852.
URL http://www.sciencedirect.com/science/article/pii/S1359645406004502

Agnew, S. R., Duygulu, Ö., 2005. Plastic anisotropy and the role of non-basal slip in magnesium alloy AZ31B. International Journal of Plasticity 21 (6), 1161 – 1193.
URL http://www.sciencedirect.com/science/article/pii/S0749641904001408

Agnew, S. R., Tomé, C. N., Brown, D. W., Holden, T. M., Vogel, S. C., 2003. Study of slip mechanisms in a magnesium alloy by neutron diffraction and modeling. Scripta Materialia 48 (8), 1003 – 1008.
URL http://www.sciencedirect.com/science/article/pii/S1359646202005912

Agnew, S. R., Yoo, M. H., Tomé, C. N., 2001. Application of texture simulation to understanding mechanical behavior of Mg and solid solution alloys containing Li or Y. Acta Materialia 49 (20), 4277 – 4289.
URL http://www.sciencedirect.com/science/article/pii/S135964540100297X

Ahzi, S., Asaro, R. J., Parks, D. M., 1993. Application of crystal plasticity theory for mechanically processed BSCCO superconductors. Mechanics of Materials 15 (3), 201 – 222.
URL http://www.sciencedirect.com/science/article/pii/016766369390018M

Aitken, Z. H., Fan, H., El-Awady, J. A., Greer, J. R., 2015. The effect of size, orientation and alloying on the deformation of AZ31 nanopillars. Journal of the Mechanics and Physics of Solids 76, 208 – 223.
URL http://www.sciencedirect.com/science/article/pii/S0022509614002385

Al-Maharbi, M., Karaman, I., Beyerlein, I. J., Foley, D., Hartwig, K. T., Kecskes, L. J., Mathaudhu, S. N., 2011. Microstructure, crystallographic texture, and plastic anisotropy evolution in an Mg alloy during equal channel angular extrusion processing. Materials Science and Engineering: A 528 (25-26), 7616 – 7627.
URL http://www.sciencedirect.com/science/article/pii/S0921509311007106

Amelang, J. S., Venturini, G. N., Kochmann, D. M., 2015. Summation rules for a fully nonlocal energy-based quasicontinuum method. Journal of the Mechanics and Physics of Solids 82, 378 – 413.
URL http://www.sciencedirect.com/science/article/pii/S0022509615000630

Ando, S., Tonda, H., 2000. Non-basal slip in magnesium-lithium alloy single crystals. Materials Transactions, JIM(Japan) 41 (9), 1188–1191.

Arsenlis, A., Parks, D. M., 2002. Modeling the evolution of crystallographic dislocation density in crystal plasticity. Journal of the Mechanics and Physics of Solids 50 (9), 1979 – 2009.
URL http://www.sciencedirect.com/science/article/pii/S002250960100134X

Asaro, R. J., 1983. Crystal Plasticity. Journal of Applied Mechanics 50, 921–934.
URL http://dx.doi.org/10.1115/1.3167205

Asaro, R. J., Needleman, A., 1985. Overview no. 42 Texture development and strain hardening in rate dependent polycrystals. Acta Metallurgica 33 (6), 923 – 953.
URL http://www.sciencedirect.com/science/article/pii/0001616085901889

Asaro, R. J., Rice, J. R., 1977. Strain localization in ductile single crystals. Journal of the Mechanics and Physics of Solids 25 (5), 309 – 338.
URL http://www.sciencedirect.com/science/article/pii/0022509677900011

Avedesian, M. M., Baker, H., et al., 1999. ASM specialty handbook: magnesium and magnesium alloys. ASM international.

Ball, E. A., Prangnell, P. B., 1994. Tensile-compressive yield asymmetries in high strength wrought magnesium alloys. Scripta Metallurgica et Materialia 31 (2), 111 – 116.
URL http://www.sciencedirect.com/science/article/pii/0956716X94901597

Ball, J. M., 1976. Convexity conditions and existence theorems in nonlinear elasticity. Archive for Rational Mechanics and Analysis 63, 337–403, 10.1007/BF00279992.
URL http://dx.doi.org/10.1007/BF00279992

Ball, J. M., James, R. D., 1987. Fine phase mixtures as minimizers of energy. Archive for Rational Mechanics and Analysis 100 (1), 13–52.
URL http://dx.doi.org/10.1007/BF00281246

Barnett, M. R., 2007. Twinning and the ductility of magnesium alloys: Part II. "Contraction" twins. Materials Science and Engineering: A 464 (1-2), 8 – 16.
URL http://www.sciencedirect.com/science/article/pii/S0921509307004297

Becker, R., Lloyd, J. T., 2015. An efficient crystal model for HCP metals: Application to Mg (under review).

Berdichevsky, V. L., 2006. On thermodynamics of crystal plasticity. Scripta Materialia 54 (5), 711 – 716.
URL http://www.sciencedirect.com/science/article/pii/S1359646205006536

Bertin, N., Capolungo, L., Beyerlein, I. J., 2013. Hybrid dislocation dynamics based strain hardening constitutive model. International Journal of Plasticity 49 (0), 119 – 144.
URL http://www.sciencedirect.com/science/article/pii/S0749641913000739

Bhattacharya, K., 1998. Theory of martensitic microstructure and the shape-memory effect. Available from author: bhatta@caltech.edu.

Bohlen, J., Nuernberg, M. R., Senn, J. W., Letzig, D., Agnew, S. R., 2007. The texture and anisotropy of magnesium-zinc-rare earth alloy sheets. Acta Materialia 55 (6), 2101 – 2112.
URL http://www.sciencedirect.com/science/article/pii/S1359645406008214

Brown, D. W., Agnew, S. R., Bourke, M. A. M., Holden, T. M., Vogel, S. C., Tomé, C. N., 2005. Internal strain and texture evolution during deformation twinning in magnesium. Materials Science and Engineering: A 399 (1-2), 1 – 12.
URL http://www.sciencedirect.com/science/article/pii/S0921509305001541

Burke, E., Hibbard, W., 1952. Plastic deformation of magnesium single crystals. Transactions of the Metallurgical Society of AIME 194, 295–303.

Cahn, J. W., Hilliard, J. E., 1958. Free Energy of a Nonuniform System. I. Interfacial Free Energy. The Journal of Chemical Physics 28 (2), 258–267.
URL http://scitation.aip.org/content/aip/journal/jcp/28/2/10.1063/1.1744102

Carstensen, C., Hackl, K., Mielke, A., 2002. Non-convex potentials and microstructures in finite-strain plasticity. Proc. R. Soc. London, Ser. A 458 (2018), 299–317.

Chang, Y., Kochmann, D. M., 2015. A variational constitutive model for slip-twinning interactions in hcp metals: Application to single- and polycrystalline magnesium. International Journal of Plasticity 73, 39 – 61.
URL http://www.sciencedirect.com/science/article/pii/S0749641915000637

Chapuis, A., Driver, J. H., 2011. Temperature dependency of slip and twinning in plane strain compressed magnesium single crystals. Acta Materialia 59 (5), 1986 – 1994.
URL http://www.sciencedirect.com/science/article/pii/S1359645410008190

Christian, J. W., Mahajan, S., 1995. Deformation twinning. Progress in Materials Science 39 (1-2), 1 – 157.
URL http://www.sciencedirect.com/science/article/pii/0079642594000077

Chun, Y. B., Davies, C. H. J., 2011. Twinning-induced negative strain rate sensitivity in wrought Mg alloy AZ31. Materials Science and Engineering: A 528 (18), 5713 – 5722.
URL http://www.sciencedirect.com/science/article/pii/S0921509311004916

Clausen, B., Tomé, C. N., Brown, D. W., Agnew, S. R., 2008. Reorientation and stress relaxation due to twinning: Modeling and experimental characterization for Mg. Acta Materialia 56 (11), 2456 – 2468.
URL http://www.sciencedirect.com/science/article/pii/S1359645408000724

Clayton, J. D., Knap, J., 2011a. A phase field model of deformation twinning: Nonlinear theory and numerical simulations. Physica D: Nonlinear Phenomena 240 (9ˇ201310), 841 – 858.
URL http://www.sciencedirect.com/science/article/pii/S0167278910003623

Clayton, J. D., Knap, J., 2011b. Phase field modeling of twinning in indentation of transparent crystals. Modelling and Simulation in Materials Science and Engineering 19 (8), 085005.
URL http://stacks.iop.org/0965-0393/19/i=8/a=085005

Clayton, J. D., Knap, J., 2013. Phase-field analysis of fracture-induced twinning in single crystals. Acta Materialia 61 (14), 5341 – 5353.
URL http://www.sciencedirect.com/science/article/pii/S1359645413003911

Coleman, B., Noll, W., 1963. The thermodynamics of elastic materials with heat conduction and viscosity. Archive for Rational Mechanics and Analysis 13 (1), 167–178.
URL http://dx.doi.org/10.1007/BF01262690

Comi, C., Corigliano, A., Maier, G., 1991. Extremum properties of finite-step solutions in elasto-plasticity with nonlinear mixed hardening. International Journal of Solids and Structures 27 (8), 965 – 981.
URL http://www.sciencedirect.com/science/article/pii/002076839190094V

Comi, C., Maier, G., Perego, U., 1992. Generalized variable finite element modeling and extremum theorems in stepwise holonomic elastoplasticity with internal variables. Computer Methods in Applied Mechanics and Engineering 96 (2), 213 – 237.
URL http://www.sciencedirect.com/science/article/pii/0045782592901335

Conti, S., Ortiz, M., 2008. Minimum principles for the trajectories of systems governed by rate problems. Journal of the Mechanics and Physics of Solids 56 (5), 1885 – 1904.
URL http://www.sciencedirect.com/science/article/pii/S0022509607002220

Conti, S., Theil, F., 2005. Single-Slip Elastoplastic Microstructures. Archive for Rational Mechanics and Analysis 178 (1), 125–148.
URL http://dx.doi.org/10.1007/s00205-005-0371-8

del Valle, J. A., Carreno, F., Ruano, O. A., 2006. Influence of texture and grain size on work hardening and ductility in magnesium-based alloys processed by ECAP and rolling. Acta Materialia 54 (16), 4247 – 4259.
URL http://www.sciencedirect.com/science/article/pii/S1359645406003557

Dixit, N., Xie, K. Y., Hemker, K. J., Ramesh, K. T., 2015. Microstructural evolution of pure magnesium under high strain rate loading. Acta Materialia 87, 56 – 67.
URL http://www.sciencedirect.com/science/article/pii/S1359645414009471

Dobroň, P., Chmelík, F., Yi, S., Parfenenko, K., Letzig, D., Bohlen, J., 2011. Grain size effects on deformation twinning in an extruded magnesium alloy tested in compression. Scripta Materialia 65 (5), 424 – 427.
URL http://www.sciencedirect.com/science/article/pii/S1359646211003101

Fan, H., Aubry, S., Arsenlis, A., El-Awady, J. A., 2015. The role of twinning deformation on the hardening response of polycrystalline magnesium from discrete dislocation dynamics simulations. Acta Materialia 92, 126 – 139.
URL http://www.sciencedirect.com/science/article/pii/S1359645415002153

Fleck, N. A., Hutchinson, J. W., 1997. Strain Gradient Plasticity. Vol. 33 of Advances in Applied Mechanics. Elsevier, pp. 295 – 361.
URL http://www.sciencedirect.com/science/article/pii/S0065215608703880

Foley, D. C., Al-Maharbi, M., Hartwig, K. T., Karaman, I., Kecskes, L. J., Mathaudhu, S. N., 2011. Grain refinement vs. crystallographic texture: Mechanical anisotropy in a magnesium alloy. Scripta Materialia 64 (2), 193 – 196.
URL http://www.sciencedirect.com/science/article/pii/S1359646210006603

Franciosi, P., Berbenni, S., 2007. Heterogeneous crystal and poly-crystal plasticity modeling from a transformation field analysis within a regularized Schmid law. Journal of the Mechanics and Physics of Solids 55 (11), 2265 – 2299.
URL http://www.sciencedirect.com/science/article/pii/S0022509607000865

Glüge, R., Bertram, A., Böhlke, T., Specht, E., 2010. A pseudoelastic model for mechanical twinning on the microscale. ZAMM - Journal of Applied Mathematics and Mechanics / Zeitschrift fr Angewandte Mathematik und Mechanik 90 (7-8), 565–594.
URL http://dx.doi.org/10.1002/zamm.200900339

Godet, S., Jiang, L., Luo, A. A., Jonas, J. J., 2006. Use of Schmid factors to select extension twin variants in extruded magnesium alloy tubes. Scripta Materialia 55 (11), 1055 – 1058.
URL http://www.sciencedirect.com/science/article/pii/S1359646206005550

Graff, S., Brocks, W., Steglich, D., 2007. Yielding of magnesium: From single crystal to polycrystalline aggregates. International Journal of Plasticity 23 (12), 1957 – 1978.
URL http://www.sciencedirect.com/science/article/pii/S0749641907001076

Guillemer, C., Clavel, M., Cailletaud, G., 2011. Cyclic behavior of extruded magnesium: Experimental, microstructural and numerical approach. International Journal of Plasticity 27 (12), 2068 – 2084.
URL http://www.sciencedirect.com/science/article/pii/S0749641911001033

Gurson, A. L., 1977. Continuum theory of ductile rupture by void nucleation and growth: Part I. Yield criteria and flow rules for porous ductile media. Journal of Engineering Materials and Technology 99 (1), 2–15.

Gurtin, M. E., Anand, L., 2007. A gradient theory for single-crystal plasticity. Modelling and Simulation in Materials Science and Engineering 15 (1), S263.
URL http://stacks.iop.org/0965-0393/15/i=1/a=S20

Hackl, K., Fischer, F. D., 2008. On the relation between the principle of maximum dissipation and inelastic evolution given by dissipation potentials. Proceedings of the Royal Society A: Mathematical, Physical and Engineering Science 464 (2089), 117–132.

Hall, E. O., 1951. The deformation and ageing of mild steel: III discussion of results. Proceedings of the Physical Society. Section B 64 (9), 747.
URL http://stacks.iop.org/0370-1301/64/i=9/a=303

Hama, T., Takuda, H., 2011. Crystal-plasticity finite-element analysis of inelastic behavior during unloading in a magnesium alloy sheet. International Journal of Plasticity 27 (7), 1072 – 1092.
URL http://www.sciencedirect.com/science/article/pii/S0749641910001841

Hansen, B. L., Beyerlein, I. J., Bronkhorst, C. A., Cerreta, E. K., Dennis-Koller, D., 2013. A dislocation-based multi-rate single crystal plasticity model. International Journal of Plasticity 44 (0), 129 – 146.
URL http://www.sciencedirect.com/science/article/pii/S0749641912001957

Hauser, F. E., Landon, P. R., Dorn, J. E., 1956. Deformation and fracture mechanisms of polycrystalline magnesium at low temperatures. Trans. ASM 48, 986–1002.

Hazell, P. J., Appleby-Thomas, G. J., Wielewski, E., Stennett, C., Siviour, C., 2012. The influence of microstructure on the shock and spall behaviour of the magnesium alloy, Elektron 675. Acta

Materialia 60 (17), 6042 – 6050.
URL http://www.sciencedirect.com/science/article/pii/S1359645412004892

Hill, R., 1966. Generalized constitutive relations for incremental deformation of metal crystals by multislip. Journal of the Mechanics and Physics of Solids 14 (2), 95 – 102.
URL http://www.sciencedirect.com/science/article/pii/0022509666900408

Homayonifar, M., Mosler, J., 2011. On the coupling of plastic slip and deformation-induced twinning in magnesium: A variationally consistent approach based on energy minimization. International Journal of Plasticity 27 (7), 983 – 1003.
URL http://www.sciencedirect.com/science/article/pii/S0749641910001786

Homayonifar, M., Mosler, J., 2012. Efficient modeling of microstructure evolution in magnesium by energy minimization. International Journal of Plasticity 28 (1), 1 – 20.
URL http://www.sciencedirect.com/science/article/pii/S0749641911000878

Hong, S. G., Park, S. H., Lee, C. S., 2010. Role of $\{10\bar{1}2\}$ twinning characteristics in the deformation behavior of a polycrystalline magnesium alloy. Acta Materialia 58 (18), 5873 – 5885.
URL http://www.sciencedirect.com/science/article/pii/S135964541000426X

Hurtado, D. E., Ortiz, M., 2012. Surface effects and the size-dependent hardening and strengthening of nickel micropillars. Journal of the Mechanics and Physics of Solids 60 (8), 1432 – 1446.
URL http://www.sciencedirect.com/science/article/pii/S0022509612000816

James, R., 1981. Finite deformation by mechanical twinning. Archive for Rational Mechanics and Analysis 77 (2), 143–176.
URL http://dx.doi.org/10.1007/BF00250621

Kadiri, H. E., Baird, J. C., Kapil, J., Oppedal, A. L., Cherkaoui, M., Vogel, S. C., 2013. Flow asymmetry and nucleation stresses of twinning and non-basal slip in magnesium. International Journal of Plasticity 44 (0), 111 – 120.
URL http://www.sciencedirect.com/science/article/pii/S0749641912001696

Kalidindi, S. R., 2001. Modeling anisotropic strain hardening and deformation textures in low stacking fault energy fcc metals. International Journal of Plasticity 17 (6), 837 – 860.
URL http://www.sciencedirect.com/science/article/pii/S0749641900000711

Kalidindi, S. R., Bronkhorst, C. A., Anand, L., 1992. Crystallographic texture evolution in bulk deformation processing of FCC metals. Journal of the Mechanics and Physics of Solids 40 (3), 537 – 569.
URL http://www.sciencedirect.com/science/article/pii/0022509692800039

Kelley, E., Hosford, W. J., 1968a. Plane-strain compression of magnesium and magnesium alloy crystals. Trans Met Soc AIME 242 (1), 5–13.

Kelley, E., Hosford, W. J., 1968b. The deformation characteristics of textured magnesium. TRANS MET SOC AIME 242 (4).

Knap, J., Ortiz, M., 2001. An analysis of the quasicontinuum method. Journal of the Mechanics and Physics of Solids 49 (9), 1899 – 1923.
URL http://www.sciencedirect.com/science/article/pii/S0022509601000345

Kochmann, D. M., Hackl, K., 2011. The evolution of laminates in finite crystal plasticity: a variational approach. Continuum Mechanics and Thermodynamics 23 (1), 63–85.
URL http://www.springerlink.com/content/b02h6085l620u737/?MUD=MP

Kochmann, D. M., Le, K. C., 2008. Dislocation pile-ups in bicrystals within continuum dislocation theory. International Journal of Plasticity 24 (11), 2125 – 2147.
URL http://www.sciencedirect.com/science/article/pii/S0749641908000594

Kochmann, D. M., Le, K. C., 2009a. A continuum model for initiation and evolution of deformation twinning. Journal of the Mechanics and Physics of Solids 57 (6), 987–1002.
URL http://www.sciencedirect.com/science/article/pii/S0022509609000325

Kochmann, D. M., Le, K. C., 2009b. Plastic deformation of bicrystals within continuum dislocation theory. Mathematics and Mechanics of Solids 14 (6), 540–563.
URL http://mms.sagepub.com/content/14/6/540.abstract

Kondo, R., Tadano, Y., Shizawa, K., 2014. A phase-field model of twinning and detwinning coupled with dislocation-based crystal plasticity for HCP metals. Computational Materials Science 95, 672 – 683.
URL http://www.sciencedirect.com/science/article/pii/S092702561400576X

Kosevich, A. M., Boĭko, V. S., 1971. Dislocation theory of the elastic twinning of crystals. Soviet Physics Uspekhi 14 (3), 286.
URL http://stacks.iop.org/0038-5670/14/i=3/a=R05

Kurukuri, S., Worswick, M. J., Ghaffari Tari, D., Mishra, R. K., Carter, J. T., 2014. Rate sensitivity and tension-compression asymmetry in AZ31B magnesium alloy sheet. Philosophical Transactions of the Royal Society A: Mathematical, Physical and Engineering Sciences 372 (2015).
URL http://rsta.royalsocietypublishing.org/content/372/2015/20130216.abstract

Lee, C. S., Duggan, B. J., 1991. A simple theory for the development of inhomogeneous rolling textures. Metallurgical Transactions A 22 (11), 2637–2643.
URL http://dx.doi.org/10.1007/BF02851357

Lee, E. H., 1969. Elastic-plastic deformation at finite strains. Journal of Applied Mechanics 36 (1), 1–6.

Lee, M. G., Lim, H., Adams, B. L., Hirth, J. P., Wagoner, R. H., 2010. A dislocation density-based single crystal constitutive equation. International Journal of Plasticity 26 (7), 925 – 938.
URL http://www.sciencedirect.com/science/article/pii/S0749641909001582

Li, B., Ma, E., Jul 2009. Atomic Shuffling Dominated Mechanism for Deformation Twinning in Magnesium. Phys. Rev. Lett. 103, 035503.
URL http://link.aps.org/doi/10.1103/PhysRevLett.103.035503

Li, X., Yang, P., Wang, L. N., Meng, L., Cui, F., 2009. Orientational analysis of static recrystallization at compression twins in a magnesium alloy AZ31. Materials Science and Engineering: A 517 (1-2), 160 – 169.
URL http://www.sciencedirect.com/science/article/pii/S0921509309003839

Lilleodden, E., 2010. Microcompression study of Mg (0001) single crystal. Scripta Materialia 62 (8), 532 – 535.
URL http://www.sciencedirect.com/science/article/pii/S1359646209008124

Lloyd, J. T., Becker, R., 2016. Stress-based crystal analysis of yielding in rolled Mg AZ31B. Philosophical Magazine, 1–17 (In press).
URL http://dx.doi.org/10.1080/14786435.2015.1132854

Lou, X. Y., Li, M., Boger, R. K., Agnew, S. R., Wagoner, R. H., 2007. Hardening evolution of AZ31B Mg sheet. International Journal of Plasticity 23 (1), 44 – 86.
URL http://www.sciencedirect.com/science/article/pii/S0749641906000398

Lubliner, J., 1972. On the thermodynamic foundations of non-linear solid mechanics. International Journal of Non-Linear Mechanics 7 (3), 237 – 254.
URL http://www.sciencedirect.com/science/article/pii/0020746272900480

Lubliner, J., 1973. On the structure of the rate equations of materials with internal variables. Acta Mechanica 17 (1-2), 109–119.
URL http://dx.doi.org/10.1007/BF01260883

Ma, A., Roters, F., 2004. A constitutive model for fcc single crystals based on dislocation densities and its application to uniaxial compression of aluminium single crystals. Acta Materialia 52 (12), 3603 – 3612.
URL http://www.sciencedirect.com/science/article/pii/S1359645404002289

Manabe, K., Shimomura, O., 2006. Effect of temperature and drawing speed on warm deep drawing characteristics of AZ31 magnesium alloy sheet. Journal of Japan Institute of Light Metals 56 (10), 521–526.

Mielke, A., 2004. Deriving new evolution equations for microstructures via relaxation of variational incremental problems. Computer Methods in Applied Mechanics and Engineering 193 (48-51), 5095 – 5127.
URL http://www.sciencedirect.com/science/article/pii/S0045782504002683

Mosler, J., Ortiz, M., 2006. On the numerical implementation of variational arbitrary Lagrangian-Eulerian (VALE) formulations. International Journal for Numerical Methods in Engineering 67 (9), 1272–1289.
URL http://dx.doi.org/10.1002/nme.1621

Van Houtte, P., 1978. Simulation of the rolling and shear texture of brass by the Taylor theory adapted for mechanical twinning. Acta Metallurgica 26 (4), 591 – 604.
URL http://www.sciencedirect.com/science/article/pii/0001616078901116

Nye, J., 1953. Some geometrical relations in dislocated crystals. Acta Metallurgica 1 (2), 153 – 162.
URL http://www.sciencedirect.com/science/article/pii/0001616053900546

Obara, T., Yoshinga, H., Morozumi, S., 1973. $\{11\bar{2}2\}\langle\bar{1}\bar{1}23\rangle$ slip system in magnesium. Acta Metallurgica 21 (7), 845 – 853.
URL http://www.sciencedirect.com/science/article/pii/0001616073901417

Onsager, L., Feb 1931. Reciprocal Relations in Irreversible Processes. I. Phys. Rev. 37, 405–426.
URL http://link.aps.org/doi/10.1103/PhysRev.37.405

Ortiz, M., Repetto, E. A., 1999. Nonconvex energy minimization and dislocation structures in ductile single crystals. Journal of the Mechanics and Physics of Solids 47 (2), 397 – 462.
URL http://www.sciencedirect.com/science/article/pii/S0022509697000963

Ortiz, M., Repetto, E. A., Stainier, L., 2000. A theory of subgrain dislocation structures. Journal of the Mechanics and Physics of Solids 48 (10), 2077 – 2114.
URL http://www.sciencedirect.com/science/article/pii/S0022509699001040

Ortiz, M., Stainier, L., 1999. The variational formulation of viscoplastic constitutive updates. Computer Methods in Applied Mechanics and Engineering 171 (3-4), 419 – 444.
URL http://www.sciencedirect.com/science/article/pii/S0045782598002199

Petch, N., 1953. The cleavage strength of polycrystals. J. Iron Steel Inst. 174, 25–28.

Proust, G., Tomé, C. N., Jain, A., Agnew, S. R., 2009. Modeling the effect of twinning and detwinning during strain-path changes of magnesium alloy AZ31. International Journal of Plasticity 25 (5), 861 – 880.
URL http://www.sciencedirect.com/science/article/pii/S074964190800079X

Qiao, L., 2009. Variational constitutive updates for strain gradient isotropic plasticity.

Radovitzky, R., Ortiz, M., 1999. Error estimation and adaptive meshing in strongly nonlinear dynamic problems. Computer Methods in Applied Mechanics and Engineering 172 (1-4), 203 – 240.
URL http://www.sciencedirect.com/science/article/pii/S0045782598002308

Reed-Hill, R., Robertson, W., 1958. Pyramidal slip in magnesium. Trans. Met. Soc. AIME 212.

Rice, J. R., 1971. Inelastic constitutive relations for solids: An internal-variable theory and its application to metal plasticity. Journal of the Mechanics and Physics of Solids 19 (6), 433 – 455.
URL http://www.sciencedirect.com/science/article/pii/002250967190010X

Roberts, E., Partridge, P., 1966. The accommodation around {1012} < 1011 > twins in magnesium. Acta Metallurgica 14 (4), 513 – 527.
URL http://www.sciencedirect.com/science/article/pii/0001616066903191

Sandlöbes, S., Zaefferer, S., Schestakow, I., Yi, S., Gonzalez-Martinez, R., 2011. On the role of non-basal deformation mechanisms for the ductility of Mg and Mg-Y alloys. Acta Materialia 59 (2), 429 – 439.
URL http://www.sciencedirect.com/science/article/pii/S1359645410005458

Schmidt-Baldassari, M., 2003. Numerical concepts for rate-independent single crystal plasticity. Computer Methods in Applied Mechanics and Engineering 192 (11-12), 1261 – 1280.
URL http://www.sciencedirect.com/science/article/pii/S0045782502005637

Schröder, J., Neff, P., Ebbing, V., 2008. Anisotropic polyconvex energies on the basis of crystallographic motivated structural tensors. Journal of the Mechanics and Physics of Solids 56 (12), 3486 – 3506.
URL http://www.sciencedirect.com/science/article/pii/S0022509608001373

Simo, J. C., 1988a. A framework for finite strain elastoplasticity based on maximum plastic dissipation and the multiplicative decomposition: Part I. Continuum formulation. Computer Methods in Applied Mechanics and Engineering 66 (2), 199 – 219.
URL http://www.sciencedirect.com/science/article/pii/004578258890076X

Simo, J. C., 1988b. A framework for finite strain elastoplasticity based on maximum plastic dissipation and the multiplicative decomposition. Part II: Computational aspects. Computer Methods in Applied Mechanics and Engineering 68 (1), 1 – 31.
URL http://www.sciencedirect.com/science/article/pii/0045782588901041

Slutsky, L. J., Garland, C. W., Aug 1957. Elastic Constants of Magnesium from 4.2 K to 300 K. Phys. Rev. 107, 972–976.
URL http://link.aps.org/doi/10.1103/PhysRev.107.972

Stainier, L., Ortiz, M., 2010. Study and validation of a variational theory of thermo-mechanical coupling in finite visco-plasticity. International Journal of Solids and Structures 47 (5), 705 – 715.
URL http://www.sciencedirect.com/science/article/pii/S0020768309004478

Stanford, N., Sotoudeh, K., Bate, P. S., 2011. Deformation mechanisms and plastic anisotropy in magnesium alloy AZ31. Acta Materialia 59 (12), 4866 – 4874.
URL http://www.sciencedirect.com/science/article/pii/S1359645411002709

Staroselsky, A., Anand, L., 2003. A constitutive model for hcp materials deforming by slip and twinning: application to magnesium alloy AZ31B. International Journal of Plasticity 19 (10), 1843 – 1864.
URL http://www.sciencedirect.com/science/article/pii/S0749641903000391

Taylor, G. I., 1938. Plastic strain in metals. J. Inst. Met. 62, 307–324.

Taylor, G. I., Quinney, H., 1934. The latent energy remaining in a metal after cold working. Proceedings of the Royal Society of London. Series A, Containing Papers of a Mathematical and Physical Character 143 (849), 307–326.
URL http://www.jstor.org/stable/96095

Tegart, W. J. M., 1964. Independent slip systems and ductility of hexagonal polycrystals. Philosophical Magazine 9 (98), 339–341.
URL http://dx.doi.org/10.1080/14786436408229197

Thoutireddy, P., Ortiz, M., 2004. A variational r-adaption and shape-optimization method for finite-deformation elasticity. International Journal for Numerical Methods in Engineering 61 (1), 1–21.
URL http://dx.doi.org/10.1002/nme.1052

Ulacia, I., Dudamell, N. V., Gálvez, F., Yi, S., Pérez-Prado, M. T., Hurtado, I., 2010. Mechanical behavior and microstructural evolution of a Mg AZ31 sheet at dynamic strain rates. Acta Materialia 58 (8), 2988 – 2998.
URL http://www.sciencedirect.com/science/article/pii/S1359645410000431

von Mises, R., 1928. Mechanik der plastischen Formaenderung von Kristallen. Zeitschrift f. Angewandte Mechanik 8, 161–185.
URL http://www.wiley-vch.de/vch/journals/2231/pss40/241_250.pdf

Wang, H., Wu, P. D., Tomé, C. N., Huang, Y., 2010. A finite strain elastic viscoplastic self-consistent model for polycrystalline materials. Journal of the Mechanics and Physics of Solids 58 (4), 594 – 612.
URL http://www.sciencedirect.com/science/article/pii/S0022509610000050

Wonsiewicz, B. C., Backofen, W. A., 1967. Independent slip systems and ductility of hexagonal polycrystals. Transaction of Metallurgical Society of AIME 239, 1422–1433.

Yang, Q., Stainier, L., Ortiz, M., 2006. A variational formulation of the coupled thermo-mechanical boundary-value problem for general dissipative solids. Journal of the Mechanics and Physics of Solids 54 (2), 401 – 424.
URL http://www.sciencedirect.com/science/article/pii/S0022509605001511

Yoshida, K., Brenner, R., Bacroix, B., Bouvier, S., 2009. Effect of regularization of Schmid law on self-consistent estimates for rate-independent plasticity of polycrystals. European Journal of Mechanics - A/Solids 28 (5), 905 – 915.
URL http://www.sciencedirect.com/science/article/pii/S0997753809000618

Yu, Q., Qi, L., Chen, K., Mishra, R. K., Li, J., Minor, A. M., 2012. The nanostructured origin of deformation twinning. Nano Letters 12 (2), 887–892, pMID: 22239446.
URL http://dx.doi.org/10.1021/nl203937t

Zhang, J., Joshi, S. P., 2012. Phenomenological crystal plasticity modeling and detailed micromechanical investigations of pure magnesium. Journal of the Mechanics and Physics of Solids 60 (5), 945 – 972.
URL http://www.sciencedirect.com/science/article/pii/S0022509612000130